PHOTODISSOCIATION OF TRANSITION METAL CATION-LIGAND COMPLEXES

By

MARY THANDI BUTHELEZI

A DISSERTATION PRESENTED TO THE GRADUATE SCHOOL
OF THE UNIVERSITY OF FLORIDA IN PARTIAL FULFILLMENT
OF THE REQUIREMENTS FOR THE DEGREE OF
DOCTOR OF PHILOSOPHY

UNIVERSITY OF FLORIDA

1997

This dissertation is dedicated to my family.

ACKNOWLEDGMENTS

I would like to thank Phil (Prof. P.J. Brucat) for his guidance, support, encouragement and friendship. Above all, I am grateful to have had a chance to work with a talented mentor whose ambition for science and passion for research are so obvious. The research work presented here would not have been possible without the help of Phil and the members of our research group.

Thanks to Robert L. Asher, a previous graduate student in our group, for his guidance and friendship as I was learning about our experimental apparatus and the art of analyzing data. It has been a great pleasure for me to work with a very good friend, Darrin Bellert, and someone whose way of thinking is different from mine but complementary. The experimental data presented in this dissertation are a result of team work between Darrin and I; many thanks to Darrin for being the best colleague. Thanks to Tom Hayes for his friendship and collaboration with data acquisition of the final projects presented here. To all the Brucat research group members and Phil, I strongly appreciate their introducing me to drinking coffee as it is, no milk and no sugar, which has now become a ritual.

Special thanks go to my family for supporting me during all my school years especially those spent abroad. Without them I could not have advanced to this level in my academic career. Finally, I would like to thank all my friends (for making it easier for me to feel at home here in the USA) for their love, support and understanding.

TABLE OF CONTENTS

ACKNOWLEDGMENTS . . . iii

LIST OF TABLES . . . viii

LIST OF FIGURES . . . x

ABSTRACT . . . xiii

CHAPTERS

1 INTRODUCTION . . . 1

2 EXPERIMENT . . . 7

- Experimental Procedures for Photodissociation Spectroscopy . . . 8
- Details of Some Crucial Aspects . . . 13
  - Gas Mixture . . . 13
  - Pumped Dye Lasers and Spectral Calibration . . . 19
  - Photodissociation Techniques . . . 19
  - Dissociation Limits . . . 22

3 THE C-X TRANSITION IN $CaKr^+$ AND $CaAr^+$ . . . 27

- $CaKr^+$ . . . 28
- $CaAr^+$ . . . 36

4 VIBRONIC ANALYSIS OF COBALT CATION-RARE GAS COMPLEXES . . . 41

- Results . . . 42
  - Vibrational Analysis . . . 43
  - Dissociation Limits . . . 52
- Discussion . . . 65

5 RESONANT PHOTODISSOCIATION OF GROUP V MAr^+ COMPLEXES . . . 72

- Data Analysis of Group V (Metal Cation)-(Argon) Complexes . . . 73
  - VAr^+ . . . 77
  - $NbAr^+$ . . . 83

$TaAr^+$ 87
Determination of Dissociation Limits 91
Discussion 92
Conclusions 102

6 POLARIZABILITY OF ARGON 104

A Measure of the Effective Electric-Dipole Polarizability of Argon 104
Discussion 110
Summary 114

7 PROBING THE IRON-LIGAND STRETCHING AND BENDING MODES IN $FeCO^+$ AND $FeCO_2^+$ COMPLEXES 116

Evidence of Spin-Allowed and Spin-Forbidden Transitions 116
Part A: Spin-Allowed Transition in $FeCO^+$ 118
Dissociation Energies 126
Trends in $FeCO^+$, $FeCO^-$ and FeCO Binding Energies 131
Part B: Spin-Forbidden Transition in $FeCO_2^+$ 136
Comparison of $FeCO_2^+$ to $FeCO^+$ Photodissociation Spectra 136
Binding Energies 137
Trends in M^+-CO_2 Binding Energies 137
Electrostatic Bonding of CO_2 and CO to a Transition Metal Cation 141

8 TWO-COLOR EXPERIMENTS 145

Two-Color Experiment Technique 147
Part A: Homonuclear Diatomic Ion 148
Discussion 156
Part B: Heteronuclear Diatomic Ion 160
The Binding Energy of $(CrFe)^+$ 162
Evidence of Two Pathways in the Photofragmentation of $CrFe^+$ 165
Overview 170

9 CONCLUSIONS 171

APPENDICES

A GENERATION OF IONS OR MOLECULES IN THE PLASMA AND DETERMINATION OF THE CONCENTRATION OF CARRIER GAS MIXTURE 178

Generation of Ions or Molecules 178
Determination of the Concentration of Carrier Gas Mixture . . 180

B DETERMINATION OF LEROY-BERNSTEIN CONSTANT, $-K^{4/3}$, FOR DERIVING THE POLARIZABILITY OF A RARE GAS ATOM IN THE PRESENCE OF A POSITIVE CHARGE 181

LIST OF REFERENCES 184

BIOGRAPHICAL SKETCH 193

LIST OF TABLES

Table page

3-1. Line Position of Assigned C-X Transitions of $CaKr^+$ and $CaAr^+$ [cm^{-1}] . . 31

3-2. Molecular Constants [in cm^{-1}] of the Low Lying States of $CaKr^+$ and $CaAr^+$ 33

3-3. Ground State Binding Energy (D_0'') of Group II MAr^+ Complexes [cm^{-1}]. 39

4-1. Line Positions of Assigned Vibronic Transitions [cm^{-1}]. 45

4-2. Spectroscopic Constants of $^{59}Co^{40}Ar^+$ Complex [cm^{-1}]. 56

4-3. Spectroscopic Constants of $^{59}Co^{84}Kr^+$ Complex [cm^{-1}]. 57

4-4. Spectroscopic Constants of $^{59}Co^{129}Xe^+$ Complex [cm^{-1}]. 58

4-5. Ground State Binding Energy, Do", of $M(Rg)^+$ Ions [eV]. 71

5-1. Line Positions of Group V Cation - Argon Complexes [cm^{-1}]. 78

5-2. Line Positions of $TaAr^+$ Complex [cm^{-1}] 80

5-3. Spectroscopic Constants of Group V Cation - Argon Molecular Ions [cm^{-1}]. 82

5-4. Ground States of M^+•Ar Complexes [cm^{-1}]. 98

5-5. Charge-(Induced-Dipole) Contribution to the Ground State Binding Energy of MAr^+. 101

6-1. Properties of the Observed Excited States of MAr^+ Systems. 109

7-1. Frequencies of Assigned Transitions in $FeCO^+$ and $FeCO_2^+$ Molecular Ions [cm^{-1}] 120

7-2. Molecular constants of $FeCO^+$ and $FeCO_2^+$ [cm^{-1}] 123

7-3. Spectroscopic Properties of Iron-Carbonyl Systems [cm^{-1}] 132

7-4. Spectroscopic Constants of M^+-CO_2 Systems [cm^{-1}].. 140

7-5. Ground State Binding Energies, D_0" (kcal/mol) 143

8-1. Frequencies of Assigned Transitions in $^{58}Ni_2^+$ and Observed Isotope Shifts [cm^{-1}]. 152

8-2. Molecular Constants for $^{58}Ni_2^+$ [cm^{-1}]. 155

8-3. Experimental and Theoretical Ground State Binding Energies, D_0" in eV, of Transition Metal Dimer Cations. 169

9-1. Spectroscopic Parameters of Studied Diatomic Ions [cm^{-1}].. 173

9-2. Spectroscopic Parameters of Studied Polyatomic Ions [cm^{-1}].. 176

LIST OF FIGURES

Figure page

1-1. Electrostatic Forces (Long-Range Attraction) of Studied M^+-L Complexes 4

2-1. Illustration of the Experimental Apparatus 9

2-2. Molecular Beam Source. 10

2-3. Time-of-Flight Mass Spectrum of $Fe(L)^+$ Complexes: Reaction with Acetone. 15

2-4. Time-of-Flight Mass Spectrum of $Fe(L)^+$ Complexes: Reaction with CCl_4 16

2-5. Laser Dye Curves for Visible Dyes 17

2-6. Observed Atomic Transitions in Neon 20

2-7. Observed and Literature Atomic Transitions in Ne. 21

2-8. Representation of One-Photon/Color Dissociation Mechanism. 23

2-9. Representation of Two-Photon/Color Dissociation Mechanism. 24

2-10. Vibronic Intervals Illustrated for a Diatomic Molecular Ion 25

3-1. Resonant Photodissociation Spectrum of $^{40}Ca^{84}Kr^+$. 30

3-2. The $CaAr^+$ C-X (0,0) Band. 32

3-3. Energy Level Correlation Diagram 35

3-4. Resonant Photodissociation Spectrum of $CaAr^+$ 37

4-1. Photodissociation Excitation Spectrum of $CoAr^+$ 53

4-2. The Photodissociation Excitation Spectrum of $^{59}Co^{129}Xe^+$ 54

4-3. Observed and Calculated Isotope Shifts of $CoXe^+$. 55

4-4. $CoAr^+$ Fit to Band Origin 60

4-5. $CoKr^+$ Fit to Band Origin 61

4-6. $CoXe^+$ Fit to Band Origin 62

4-7. $CoAr^+$ Dissociation Limits 63

4-8. The Low-Lying Atomic States of Co^+ [43]. 64

4-9. The Long Extrapolation of a LeRoy-Bernstein Plot. 66

4-10. Correlation Diagram: k as a Function of D_0' 67

5-1. Resonant Photodissociation Spectrum of $^{51}V^{40}Ar^+$ 74

5-2. Resonant Photodissociation Spectrum of $^{93}Nb^{40}Ar^+$ 75

5-3. Resonant Photodissociation Spectrum of $^{181}Ta^{40}Ar^+$ 76

5-4. Observed and Calculated Isotope Shift of VKr^+ 81

5-5. VAr^+ Fit to Band Origin 84

5-6. $V^{84}Kr^+$ Excited States 85

5-7. Excited States of $NbAr^+$ 86

5-8. The $TaAr^+$ A-X Band System 89

5-9. $TaAr^+$ Fit to Band Origin. 90

5-10. LeRoy-Bernstein Plots of Group V (Metal Cation)-Argon Complexes . 93

5-11. Low-Lying Atomic States of $^{93}Nb^+$ Ion 94

5-12. Low-Lying Atomic States of $^{181}Ta^+$ Ion. 97

6-1. LeRoy-Bernstein Limiting Slopes for MAr^+ Complexes 111

7-1. The Resonant Photodissociation Spectrum of $^{56}FeCO^+$ 119

7-2. The Band Origin (0,0) of $^{56}FeCO^+$ 124

7-3. The Assigned Transitions of the A ← X Progression in $^{56}FeCO^+$. . . . 125

7-4. Observed and Calculated Isotope Shift of $FeCO^+$. 128

7-5. The Low-Lying Atomic States of Fe^+ [9] 129

7-6. Simplified Molecular Orbitals in $FeCO^+$. 130

7-7. Schematic Representation of the Bonding Orbitals in $FeCO^+$. 133

7-8. $^{56}FeCO_2^+$ Photodissociation Spectrum 138

8-1. Two-Color Resonant Photodissociation Spectrum of $^{58}Ni_2^+$ 149

8-2. Excited State, [13.07]9/2, Vibrational Quantum Number Assignment. . 151

8-3. Assigned Excited States in $^{58}Ni_2^+$ 157

8-4. Photodissociation Spectrum of $^{52}Cr^{56}Fe^+$ 161

8-5. Evidence of One-Photon Dissociation in $CrFe^+$ 163

8-6. Evidence of Two-Color Photodissociation in $CrFe^+$. 164

8-7. Two Pathways in the Photodissociation of $CrFe^+$. 166

8-8. Products Produced in the Photodissociation of $CrFe^+$ 168

Abstract of Dissertation Presented to the Graduate School
of the University of Florida in Partial Fulfillment of the
Requirements for the Degree of Doctor of Philosophy

PHOTODISSOCIATION OF TRANSITION METAL CATION - LIGAND COMPLEXES

By

Mary Thandi Buthelezi

August, 1997

Chairperson: Philip J. Brucat
Major Department: Chemistry

High-resolution photodissociation spectroscopy has been used to characterize singly charged metal-ligand binary ions in the visible region. Molecular ions of interest [e.g. (M^+-L) complexes, where M^+ is either Ca^+, Co^+ , V^+ , Nb^+ , Ta^+ or Fe^+ with Ar, Kr, Xe, CO and CO_2 'ligands'] and metal diatomic ions [Ni_2^+ and $CrFe^+$], generated in a laser-driven-plasma supersonic expansion ion source, are mass-selected prior to photo-interrogation with tunable laser light. Vibronic analysis of the spectra for various molecular ions provide their spectroscopic constants; vibrational frequencies and anharmonicities of the excited states are obtained.

For diatomic metal cation - (rare-gas) complexes, band systems with long progressions (that lead to convergence) are analyzed via LeRoy-Bernstein (LB) protocol to provide accurate dissociation limits for the probed excited states. From this analysis both ground and excited states well depths are then determined. Each molecular ion has a unique LB slope which depends on both the polarizability of the rare gas and the reduced mass. Thus, from several examples of M^+(Ar) systems, the effective electric-dipole polarizability volume of argon (derived from LB slopes) in a field of a point charge yields a value (1.48 ± 0.1 Å^3) slightly less than the accepted literature 'bulk' value (1.64 Å^3).

Trends in the binding energies of transition metal cation - ligand systems and calcium cation - (rare gas) complexes are discussed. Comparisons between experimental observations and theoretical predictions indicate that calculations estimate parallel trends to experiment but consistently underestimate the true binding energies by ≈20 %.

CHAPTER 1
INTRODUCTION

In order to understand chemical reactions, characterization of the forces holding atoms together has to be made. Extensive reference data on covalently bound molecules can be found in literature, such as the CRC Handbook of Chemistry and Physics [1]. On the contrary, fewer examples of inductively-bound molecular ions are represented [2]. Details of the binding mechanism, molecule structure, energetics and dynamics involved in an ion-neutral system are not yet fully characterized either. As a result, both experimentalists [3-5] and theorists [6,7] (have and) are still conducting research in this field. The analysis of the data acquired for this dissertation adds new spectroscopic parameters for several molecular ions. In addition, comparisons of experimental observations and theoretical predictions are made in order to determine the accuracy of the postulated models.

The chemistry of transition metal containing complexes is extremely important in the fields of inorganic and surface chemistry. Applications of the obtained experimental data are numerous. Briefly, the ability of transition metal complexes to act as catalysts for many types of chemical reactions in solution [8] has caught the interest of many researchers. The abundance of low-lying electronic states [9] is one of the vital features of transition metal cations that is central to their ability to catalyze chemistry, since it enables the metal center to be a versatile reaction site to which many different types of ligands can bond and subsequently react. However, the density of such states makes it difficult to generate transition metal (TM) complexes in any one specific electronic state. This challenge has been overcome through the development of laser spectroscopy in supersonic molecular beams [10].

High-resolution laser photodissociation spectroscopy can provide accurate information on the structure and binding of unstable molecular ions or small cluster ions that can only be generated in small quantities ($\approx 10^8$ ions per laser pulse, see Appendix A). The gas phase molecular ions are isolated prior to photo-interrogation in a custom built time-of-flight mass spectrometer (TOF-MS) in order to eliminate contamination (from other absorbing species) and are by their nature "free" of solvent or matrix effects.

In this study, the design of the Brucat research group experimental apparatus [chapter 2] has made it possible to generate cold nascent cluster ions ($T_{rot} \leq 10$ K) and their properties determined from the obtained resonant photodissociation spectra. This technique has proven to be a powerful means for studying systems of transition metal cation complexed with various ligands. However, the lifetime of molecular ions plays a vital role in whether a spectrum will be obtained or not. That is, the prepared molecular ion must absorb the visible photon of laser light and dissociate in the time scale of the experiment (1 ps $< \tau <$ 10 μs). For very short lived excited states the spectrum appears as a featureless threshold (for example: NiN_2O^+ [11]) above which only broad photodissociation resonances are observed and below which no resonant one-photon dissociation is detected. If however, the lifetime of the excited states is much longer than the experimental time window, then no spectrum will be observed (example: ML_n^+; n> 100). The probed excited states of molecular ions with appropriate lifetimes will exhibit vibronic transitions (if the molecular ion has enough time to vibrate) and ro-vibronic transitions (if the molecular ion has enough time to rotate) prior to dissociating. The spectra of these ions result from direct or predissociation mechanism.

Resonant two-color dissociation (R2CD) technique [chapter 2] has been successfully applied to systems that have adiabatic binding energies (D_0'') that are larger than the one-photon energy (coming from the first laser pulse) and for determining the lifetime of the excited states (examples: Ni_2^+ and $CrFe^+$ [chapter 8]).

Investigated projects in this dissertation involve characterization of both diatomic and polyatomic molecular ions. Chapters 3 to 7 focus primarily on systems that exhibit inductive forces [12] , such as, charge-(induced-dipole), charge-quadrupole and charge-(dipole) shown in Figure 1-1. However, three examples $FeCO^+$, Ni_2^+ and $CrFe^+$ are also covalently bound complexes. The following topics are addressed:

INDUCTIVE OR ELECTROSTATIC FORCES

Type of Interaction		Energy of Interaction	Example
Charge-induced dipole	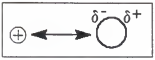	$-\frac{q^2\alpha}{2r^4}$	M^+(Rare-gas)
Charge-quadrupole	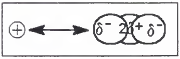	$\frac{q\Theta}{4r^3}(3\cos^2\theta - 1)$	$M^+(CO_2)$
Charge-dipole	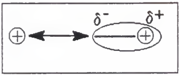	$-\frac{q\mu}{r^2}\cos\theta$	$(M-CO)^+$

Figure 1-1. Electrostatic Forces (Long-Range Attraction) of Studied M^+-L Complexes.

All studied metal cation-rare gas diatomics are fundamentally bound by a charge-(induced-dipole) interaction and the equation that describes this energy is given in the top panel of this figure. Polyatomic examples include, $Fe^+{\bullet}CO_2$ which is bound primarily by a charge-quadrupole interaction and the formula that predicts this energy is given in the middle panel. Fe^+-CO, which is a covalently bound molecular ion, has additional electrostatic forces such as charge-dipole (described in the bottom panel) and charge-quadrupole forces. A covalent bond has no simple expression.

a) Chapters 3, 4 and 5 present a study of $M^+\bullet(Rg)$ diatomic ions. Trends in the binding energies as a function of both metal ion and the ligand are discussed.

b) Calculation of the polarizability of Ar is presented in Chapter 6. Since several transition metal cation-Argon complexes have been a subject of the Brucat research group for the past decade, there exist enough data from which the effective electric-dipole polarizability of Argon in a field of a positive point charge can be derived. Therefore, this information has been extracted and results are presented.

c) Chapter 7 presents excited states progressions of spin-allowed and spin-forbidden transitions probed in $FeCO^+$ and $FeCO_2^+$, respectively.

d) Chapter 8 focuses on the two-color photodissociation of transition metal diatomic ions, Ni_2^+ and $CrFe^+$.

Ion-neutral systems serve as models for solvation processes. A common example is the dissolution of NaCl(s) in water which is presented in essentially all general chemistry text books. The binding energy of a sodium cation to a water molecule can be described as a charge-dipole interaction (dipole of H_2O = 1.847 D [2]), however, studying simpler systems such as $M(Rg)^+$ which are primarily bound by charge-(induced dipole) forces serves as the first step to characterizing such electrostatic forces. By studying metal cations ligated with a rare gas atom the system is simplified to a level that can easily be tractable by theoretical investigations. Once these complexes are fully characterized, then those with higher orders of multipoles can also be examined.

Previous members of the Brucat research group have studied various transition metal cation-water systems [3-5] and theory has predicted spectroscopic properties of some of these molecular ions [6,7]. However, sample data in literature both from experiment and theory of $M^+\cdot(Rg)$ complexes far outnumber those of M^+-(H_2O) systems.

The next logical step up from studying metal cation-rare gas diatomic ions would be to investigate properties of polyatomic systems. This is the topic of chapter 7. The primary electrostatic forces described are both charge-quadrupole (example: $Fe^+\cdot CO_2$) and charge-dipole, as illustrated in Figure 1-1. However, a more complex system, $FeCO^+$, that exhibits both these electrostatic forces in addition to a covalent bond character (which is also found in metal cation-metal complexes [chapter 8]) has also been spectroscopically probed. Metal dimer cations are expected to be the most bound of the studied examples here.

Almost all of the data presented in this dissertation deal with vibronic analysis of the obtained spectra and spectroscopic parameters, such as vibrational frequencies, anharmonicities and binding energies of the probed states are provided. In addition, a measure of the effective electric-dipole polarizability of argon in the presence of a positive point charge is presented. Evidence of two photodissociation pathways for $CrFe^+$ molecular ion is revealed in the obtained spectra.

CHAPTER 2
EXPERIMENT

The vibrational and rotational analysis of the spectra of molecules provide some information about their geometry. Traditional spectroscopic techniques, such as Infrared (IR) and Raman absorption spectroscopy useful for normal stable molecules, are hard pressed to deal with novel molecules such as charged species. Therefore, for unstable complexes that can be generated only in small quantities, techniques with fast-time response and higher sensitivity are essential. Consequently, in the past twenty years the development of laser spectroscopy in supersonic molecular beams pioneered by Smalley et al. [10] and Levy [13] has grown and diversified. The use of supersonic expansion allows the preparation of isolated, internally cold gas phase molecules thus retaining the advantage of matrix isolation spectroscopy without the disadvantage of matrix effects. The spectral simplification that results when the internal degrees of molecular freedom are cooled facilitates the analysis of spectra that would otherwise be complicated.

Various spectroscopic techniques are being used in conjunction with supersonic expansions to study weakly bound (van der Waals or electrostatic) complexes. Some examples of the utilized techniques include photodissociation, stimulated emission pumping, laser induced fluorescence and photoelectron spectroscopy. For the work presented in this dissertation photodissociation spectroscopy was used, as described here.

Experimental Procedures for Photodissociation Spectroscopy

A detailed outline of the experimental equipment (manufacturers, dimensions and modifications) including procedures appeared previously [5,6]. Thus, only a summary of the general overview of experimental procedures involved in obtaining one-photon dissociation and two-color or two-photon dissociation spectra is provided. However, any new developments or improvements will be elaborated upon.

Figure 2-1 displays an illustration of the experimental apparatus. The focused light of the second harmonic generated from a Nd^{3+}:YAG laser (7 ns duration with 10-25 mJ/cm^2) vaporizes the surface of a rotating target rod (mainly composed of the metal of interest) to generate atoms and subsequently ionizes them to make both positive and negative ions. The vaporization laser is timed to fire at the center of the highest density portion of a pulsed Helium gas seeded with $\leq 1\%$ of ligating gas or reactant species. The generated ions and neutrals are expanded through a small orifice (2 mm diameter) and cooled into the vibrationless level of the ground electronic state via supersonic expansion as shown in Figure 2-2.

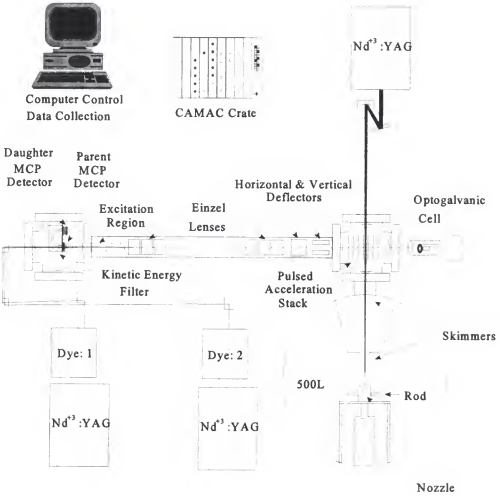

Figure 2-1. Illustration of the Experimental Apparatus.

This figure [from Ref. 6] shows the setup of the experiment. The molecular ions are generated in a pulsed laser-driven plasma supersonic expansion source. The vaporization laser (top right) is timed to fire in the middle of a pulsed gas (seeded with ≈1 % ligating species in Helium carrier gas). The resulting molecular beam is expanded and cooled through a supersonic nozzle then collimated by the skimmers. Approximately 1 m downstream of the supersonic orifice, the positive ensemble is accelerated 90° out of the beam with a kinetic energy ca. 1.45 keV into a custom time-of-flight mass spectrometer. The ions are deflected and guided by both deflectors and einzel lenses into the entrance of kinetic energy filter (hemispherical electrostatic sector). Photodissociation spectra are obtained by monitoring the photocurrent of the fragment ion (using the micro channel plate detector) that results from an isolated parent ion as a function of the laser energy. The laser light simultaneously strikes the neon optogalvanic cell from which a neon spectrum is obtained for spectral calibration.

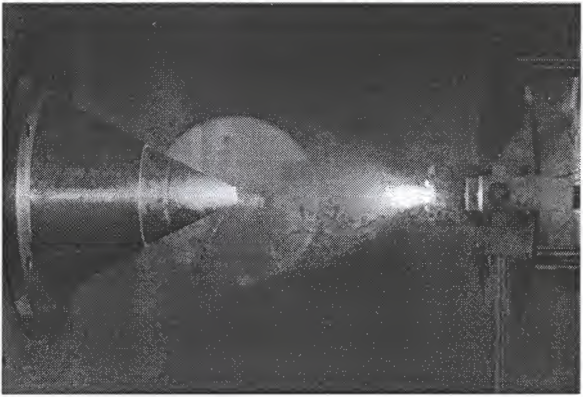

Figure 2-2. Molecular Beam Source.

The figure displays the laser-driven plasma expanding (right to left) out of the supersonic nozzle. The skimmer on the left (cone) collimates the gas flow of clusters into a molecular beam.

The operating pressure in the main chamber where atomic and molecular ions are generated is 10^{-5} Torr. The inlet gas flow (consisting of high pressure pulse of helium seeded with ≈1 % ligating gas or reactant, normally between 20 to 150 PSI) through the nozzle orifice counterpropagates along the vaporization laser beam axis and a plasma is generated. This plasma expands adiabatically and two skimmers aid in collimating the gas mixture flow into a molecular beam. The beam thus formed travels through two differential-pumping regions defined by the skimmers with operating pressures of 10^{-6} and 10^{-7} Torr respectively. The 10^{-7} Torr region is liquid nitrogen trapped, oil-free chamber and serves as an acceleration region of a custom time-of-flight mass spectrometer (TOF-MS).

The positive ensemble is accelerated 90° out of the molecular beam with a kinetic energy ca. 1.45 keV into a custom TOF-MS. As the ions travel down a 2.45 m flight tube mass separation occurs, and the molecular ion ensemble is guided by deflectors and einzel lenses (labeled in Figure 2-1) into the entrance aperture of a 180° electrostatic sector which serves as an ion kinetic energy filter. The time-of-arrival at the detector (micro channel plates, MCP) determines the mass to charge ratio (m/z) at the time of acceleration. TOF-MS are obtained by setting the electrostatic analyzer to transmit ions of the full beam kinetic energy ca. 1.45 keV.

Isolation of a molecular ion of interest is then possible based on its time of arrival at the detector. The one-photon dissociation mechanism utilizes the energy output from a Nd^{3+}:YAG pumped dye-laser (labeled Dye:1 in Figure 2-1) which is used to photoexcite ground state vibrationless level molecular ions into a specific excited state energy level. Electrostatic energy distribution of the ions following photoexcitation allows for the determination of the fragmentation yield of any given parent ion. That is, fragment ions produced via photodissociation are detected at the time-of-arrival associated with the parent mass but at laboratory kinetic energies approximately equal to the parent beam energy (955 V) times the ratio of fragment to parent ion masses. The optical spectra of the mass selected isotopomers are obtained simultaneously (but separately) in order to record accurate isotope shift. The one-color dissociation technique has been successfully applied to all studied systems presented in this dissertation with the exception of metal dimer cation complexes for which two-photon or two color dissociation experiments were conducted.

For the two-color or two-photon dissociation technique, photoexcitation is accomplished with the visible light of two Nd^{3+}:YAG pumped dye-lasers. The first laser pulse of lower power ≈5 mJ/cm^2 (excitation) serves to prepare an excited vibronic level of the molecule. The dissociation of the photoexcited ion is accomplished by a second laser pulse of higher energy and fixed frequency. Calibration is accomplished by simultaneous acquisition of Neon optogalvanic transitions with the ion photodissociation spectrum. In order to transform the calibrated transition frequencies to the rest frame, a Doppler frequency correction is performed. To facilitate data acquisition, critical timing parameters and voltages are performed by CAMAC crate/microcomputer combination.

Details of Some Crucial Aspects.

Gas Mixture

The gas mixture is either premixed in a cylinder (with volume ≈ 50 L) which is delivered by a regulator or may be mixed dynamically using dual regulators and a reservoir of a volatile substance (e.g., acetone or carbon tetrachloride with helium flowing over it). Preparation of a 1% tank of Ar in He would require diluting 10 PSI of pure Ar in pure He to a total of 1000 PSI mixed gas and at least 48 hours of “equilibration” for the concentration to be uniform within the tank. The gas mixture is then ready to be used for the experiment. The final concentration of the prepared gas mixture can be directly obtained from the time of arrival of the molecular ions at the “A” chamber (demonstrated in appendix A).

Success with four reactions using the dynamic method has yielded spectra in some molecular ions. Equations of three new reactants seeded in He are given, below

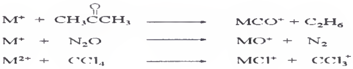

$$M^+ + CH_3\overset{O}{\overset{\|}{C}}CH_3 \longrightarrow MCO^+ + C_2H_6$$

$$M^+ + N_2O \longrightarrow MO^+ + N_2$$

$$M^{2+} + CCl_4 \longrightarrow MCl^+ + CCl_3^+$$

The first reactant ligand studied in the Brucat research group was water, details and spectra of $M(H_2O)^+$ complexes are presented elsewhere [5,6]. Sample time-of-flight mass spectra are provided in Figures 2-3 and 2-4. Figure 2-3 results from a nearly pure Fe rod (and reaction with acetone, (CH_3COCH_3). Figure 2-4 results from reaction of the Fe rod and carbon tetrachloride , CCl_4. Note that in Fig. 2-3 acetone reacts with Fe^+ ion to produce $FeCO^+$ complex for which a spectrum has been obtained and is discussed in Chapter 7. An alternative to preparing this molecular ion, $FeCO^+$, was to pre-mix a ≈1% CO tank in pure He and both methods resulted in identical photodissociation spectrum. In the same mass spectrum, a second CO ligand attached to the iron cation was also observed and $Fe(CO)_2^+$ complex occurs at the m/z as Fe_2^+ dimer ion.

The described experimental apparatus allows for unit mass resolution thus there is no distinction between the mass peak at 112 (m/z) corresponding to both Fe_2^+ and $Fe(CO)_2^+$. As a result, the optical spectra of these molecular ions were not investigated under these conditions. However, it is possible to synthesize uncontaminated Fe_2^+ ion by using pure He as a carrier gas with no ligating gas seeded into it. Interestingly, acetone binds preferentially and makes the largest cluster ion $Fe(CH_3COCH_3)^+$ however, there were no resonant transitions in the region accessible by the green light (532 nm) pumped dye laser (11 200 to 18 000 cm^{-1}), see Figure 2-5 for dye curves.

Since the metal is the chromophore in each of the investigated systems, the species of interest (in the TOF-MS) are complexes that contain a metal that absorbs in the visible. The second reaction of transition metal cation with N_2O

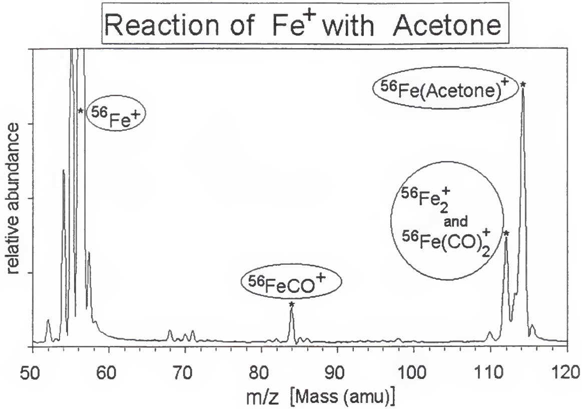

Figure 2-3. Time-of-Flight Mass Spectrum of Fe(L)$^+$ Complexes: Reactions with Acetone.

This figure shows ions resulting from the vaporization of a rod with ≈70 % Fe content. The Fe cations complex with the reactant (≤1% acetone seeded into He carrier gas) and the main products of this reaction are labeled. Note that the mass at m/z = 112 corresponds to either (or both) dimer $^{56}Fe_2^+$ or $^{56}Fe(CO)_2^+$.

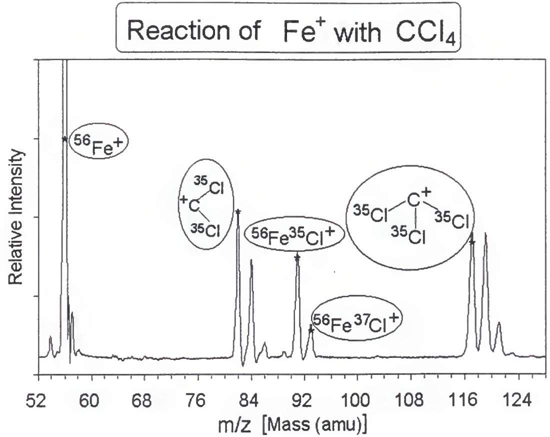

Figure 2-4. Time-of-Flight Mass Spectrum of Fe(L)$^+$ Complexes: Reactions with CCl$_4$.

This figure shows ions resulting from vaporization of a rod of ≈80 % Fe rod content. The Fe cations complex with the reactant (≤1% CCl$_4$ seeded into He carrier gas) and the main products of this reaction are labeled.

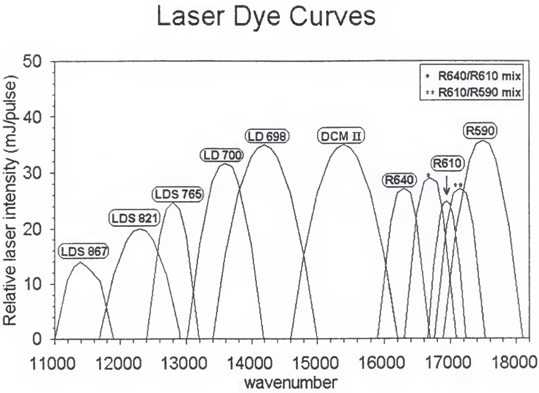

Figure 2-5. Laser Dye Curves for Visible Dyes.

The figure shows simplified dye out-put power curves of nine pure dyes, labeled, plus two mixed samples, marked with asterisks, as a function of energy (wavenumber). The optical regions accessible by each dye are true representations, however, the simulated curves were generated by fitting a parabola to known maximum dye out-put and end points values thus the indicated laser intensity is only an approximation.

yields either MO^+ products or $M(N_2O)^+$. (Note that for this reaction a pre-mixed 1% N_2O tank in He was used as a carrier gas.) Early transition metal cations form very strong M-O bonds therefore generation of MO^+ is preferred as was the case with V^+ and Fe^+ ions. The Brucat research group has successfully made FeO^+ molecular ion (using N_2O as a reactant) and probed its ro-vibronic levels, however, the vibrational spectrum is congested and thus difficult to interpret. Rotational resolution of some of the bands was obtained, and data are currently being analyzed. For late transition metal cations complexation of M^+ with N_2O as a ligand occurs with no evidence of MO^+ in the mass spectrum. For example, reaction of a 1 % N_2O (balance He) gas mixture with Ni^+ ions formed $Ni(N_2O)^+$ clusters but no NiO^+ molecular ions. The adiabatic binding energy threshold for the ground state of $Ni(N_2O)^+$ was measured [11].

Finally, the reaction of Fe^+ with carbon tetrachloride also produced a molecular ion of interest $FeCl^+$ but unfortunately, like $Fe(acetone)^+$ there was no evidence of photodissociation action spectrum. Indication of CCl_4 gas molecules that have reacted to form CCl_2^+ or $(Cl_2C_2Cl_2)^{2+}$ molecular ions is given by a peak at mass/charge ratio of 82 and the iron dimer cation (m/z of 112) is not formed here. In both Figures 2-3 and 2-4 the atomic Fe^+ peak was the most intense and it appears off scale since the y-axis was highlighted to "zoom in" on the smaller cluster ions. Natural occurring isotopes (above 1% in abundance) of all the atomic ions are present in all the TOF-MS and contamination in the iron rod with other metals such as Mn with a mass peak at 55 m/z are also revealed.

Pumped Dye Lasers and Spectral Calibration

Figure 2-5 shows the accessible region (11 200 to 18 000 cm^{-1}) of the dyes used to obtain the spectra presented in the next chapters. Since the photofragmentation spectra are obtained by irradiation of the molecular ion of interest by a tunable Nd^{3+}:YAG pumped dye laser it is important to know what regions each dye will access with adequate laser power (minimum dye output of 5 mJ/cm^2 per pulse). Note that these curves are artificial in relative laser intensity since only the maximum and perhaps three to four additional data points were fit to a standard parabola. However, the working ranges of each dye are expected to be reliable representations. The experimental dye output values were measured with a power meter for the (Lumonics) Nd^{3+}:YAG pumped dye laser marked 1 in Figure 2-1. This dye laser was used to probe all conducted experiments whereas the second laser (Dye 2 in Figure 2-1) was used only for two-color experiments [Chapter 8].

Figure 2-6 shows the observed neon transitions in the accessible optical region and Figure 2-7 shows a “close-up” that compares literature values (tick marks above the spectrum) to experimental transitions in Ne (spectrum). Clearly, all literature neon transitions are reproduced in the experiment and serve for spectral calibration of the unknown photodissociation spectra.

Photodissociation Techniques

Two types of experimental techniques were tackled. First, the most direct methodology which was used for all molecular ions with the exception of metal dimer

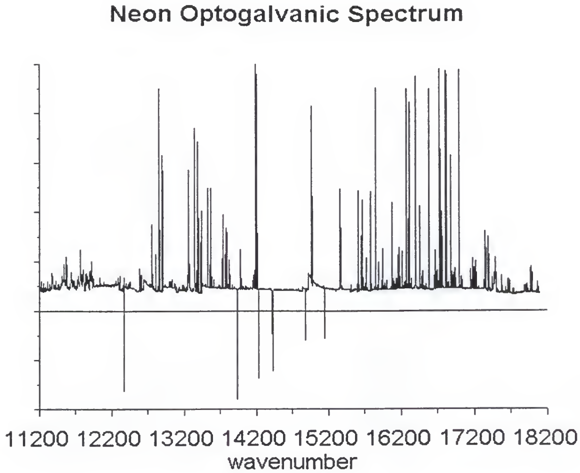

Figure 2-6. Observed Atomic Transitions in Neon.

The figure shows neon optogalvanic transitions observed in the region of 11 200 to 18 200 cm^{-1}. The intensity and sign of these transitions are variable and they depend on the probability which is a function of the laser light power and voltage applied to the hollow cathode. However, the line positions remain unchanged, as shown in Figure 2-7, comparison of experiment and literature neon transitions.

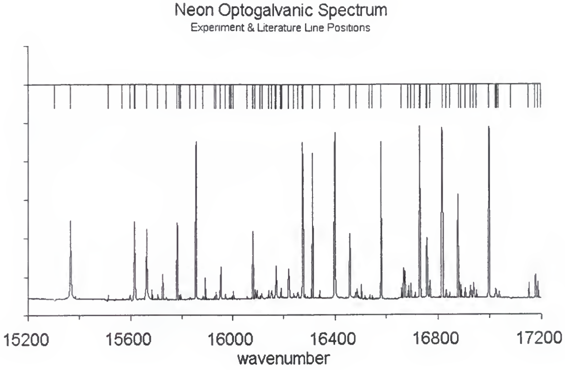

Figure 2-7. Observed and Literature Atomic Transitions in Ne.

The figure shows “a closeup” of a neon optogalvanic spectrum in the region 15 200 to 17 200 cm^{-1}. Comparisons between literature (tick marks above the spectrum) and experiment (spectrum) line positions indicates that all known neon transitions are probed in the Brucat group experimental apparatus.

cations was the one photon-dissociation (or one-color dissociation) illustrated in Figure 2-8. If photons from the excitation laser populates a specific vibrational energy level in an excited state which is to higher energy than the adiabatic limit of the ground state, then, rapid predissociation event may occur. The photocurrent of a fragment ion (usually M^+) resulting from the dissociation of an isolated parent molecular ion is recorded as a function of laser frequency as indicated in all presented photodissociation spectra.

The mechanism of a two-color photodissociation is very similar to that described above with the exception that two-photons or two-color dissociation lead to a spectrum. Figure 2-9 displays transitions involved in a two-color dissociation experiment. In this instance the timing between the two lasers is crucial with the resonant laser marked ($h\nu_1$) preparing the excited state molecular ions and the second laser ($h\nu_2$) held fixed at a non-resonant frequency. The resonant laser first populates a specific excited state energy level and the non-resonant laser (dissociation laser) aids in promoting the molecular ions above the adiabatic dissociation limit as illustrated in the Figure. Then, coupling of this prepared level to unbound levels lead to predissociation as described above.

Dissociation Limits

When two potential energy surfaces involved in an electron transition have different r_e values (shown in Figure 2-10), then, Franck-Condon factors favor long vibrational progressions in the excited state, for photofragmentation excitation spectrum. The measured upper vibrational energy levels can be analyzed via

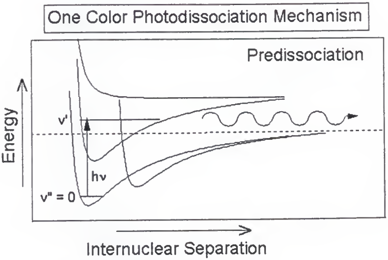

Figure 2-8. Representation of One-Photon/Color Dissociation Mechanism.

When an isolated molecular ion absorbs a photon and populates a specific excited state level of similar internuclear separation to the ground state (resonance) but above the adiabatic dissociation limit (indicated with the dashed line) coupling of this level to unbound levels at this energy results in a rapid predissociation. The photofragment of the resulting metal cation daughter is monitored as a function of laser frequency.

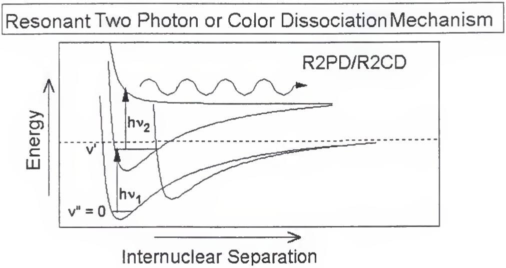

Figure 2-9. Representation of Two-Photon/Color Dissociation Mechanism.

When an isolated molecular ion absorbs a photon ($h\nu_1$) and populates a specific excited state level of similar internuclear separation to the ground state (resonance) but below the adiabatic dissociation limit (indicated with the dashed line) no dissociation can occur unless a second photon or color at a fixed non-resonant energy ($h\nu_2$) aids in effectively coupling of this level to unbound levels at an energy above the ground state dissociation threshold. The photofragment of the resulting metal cation daughter is then monitored as a function of laser frequency.

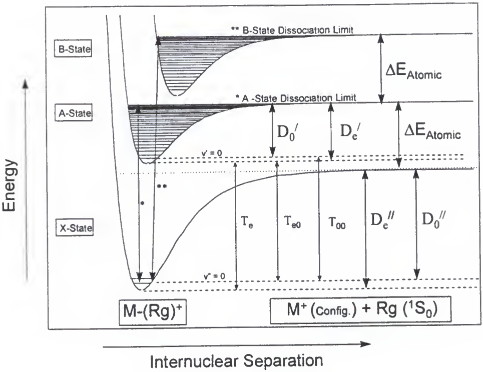

Figure 2-10. Vibronic Intervals Illustrated for a Diatomic Molecular Ion.

The figure displays hypothetical potential energy curves as a function of internuclear separation of a M-(Rg)$^+$ complex. The presented ground state binding energies (D_0''), in this dissertation, are determined from the difference between the measured dissociation limit (marked with asterisks) and the assigned atomic difference (ΔE_{Atomic}) corresponding to the atomic asymptotes of the relevant states. Excited state binding energy values, D_0', are then determined from subtracting the electronic term origin T_{00} (derived from fitting observed vibrational energy levels to a standard function given by Equation 3-1) from the known dissociation limit of that particular state.

LeRoy-Bernstein (LB) [14] method to determine the excited state dissociation limit, D*(LB), marked with asterisks in Figure 2-10. The ground state binding energy D_0'' can be calculated by using the simple relationship: [$D_0'' = D^*(LB) - \Delta E_{Atomic}$] provided the atomic transition energy is known [9]. Assuming a Morse type potential energy surface, the observed vibrational energy levels can be fit to the predicted energy levels of a Morse function. Spectroscopic constants such as the electronic term origin, T_{e0}, vibrational frequencies and anharmonicities can be determined from this type of data analysis.

CHAPTER 3
THE C-X TRANSITION IN $CaKr^+$ AND $CaAr^+$

In our goal to describe the chemical bonding in all possible types of molecules, involving any combination of constituent elements, it is important to survey benchmarks of particular types of interactions which will play the role of signposts in the quest for new and uncharacterized systems. Molecules that serve as these benchmarks should be completely and accurately characterized, both experimentally and theoretically, and be as 'pure' an example of a particular chemical interaction as possible.

One type of limiting behavior in chemical bonding is the electrostatic bond. In general chemistry, the first kind of solid discussed is the ionic salt (e.g., NaCl) which is stable not because of covalent sharing of the electrons of the constituent atoms, but by the simple electrostatic interaction of the atomic ions which result from electron donation of electrons from the metal to the halogen.

Electrostatic complexes of ions with neutrals are conceptually simpler still. Before the complex is formed, an electron is removed from the metal forming a cation, and this ion interacts with the polarized neutral 'ligand' to form a complex. In the limit of pure electrostatics, no electron donation or sharing takes place. Metal ion - rare gas diatomic complexes are the smallest and simplest example of such behavior. If the metal ion is that of an alkali element, such as $NaAr^+$, then the complex is composed of two spherically symmetric centers, and the description of this molecule is quite analogous to that of the NaCl solid. If, however, the neutral metal atom has more valence electrons than it loses upon ionization, the resulting ion has 'extra' electrons outside a closed shell, and is 'lumpy'. The character of the complex will depend largely on the interaction of the ions' valence electrons with the closed shell of the rare-gas, and will have properties that vary for different electronic configurations of the metal ion.

In the following study a metal-ion rare gas complex that has just one 'extra' electron on the metal center, an (alkali-earth ion) - (rare-gas) complex is examined. In the ground state, this metal valence electron is in an s-orbital, and the metal is spherical and 'alkali like'. After photoexcitation, this electron may be promoted to a p-orbital, or, as in this study, promoted to a d-orbital. The excited state of the complex in this latter configuration exhibits the behaviour of a transition metal ion complex.

$CaKr^+$

Figure 3-1 shows a portion of the resonant photodissociation spectrum of ${}^{40}Ca^{84}Kr^+ + h\nu \rightarrow {}^{40}Ca^+ + {}^{84}Kr$ which contains the only electronic transition of this molecular ion observed to date. Another isotopic variant of this molecule, ${}^{40}Ca^{86}Kr^+$, is also observed at natural abundance simultaneously during the scan, but is not displayed in this figure. As is usual in spectra of this type, the horizontal axis of this figure is the frequency of the dissociation laser and the vertical axis is the relative photodissociation yield, i.e. the Ca^+ photocurrent. No Kr^+ is observed as a photoproduct. The spectrum in Figure 3-1 results from a one-photon absorption of the ion followed by predissociation; the upper state of this transition is well above the adiabatic dissociation limit of the molecule. The features in the spectrum represent vibronic transitions in the electronic system labelled **C-X**, as it is expected to be the third reddest of all possible electronic transitions originating from the ground electronic state. The transitions are labelled in the figure by their upper and lower vibrational quantum numbers in the accepted form: (v',v").

The relative intensities and spacings of the transitions readily lead to the proposed assignment and the resulting spectroscopic constants for the upper and lower states in the transition. The very small isotope shifts observed between $^{40}Ca^{84}Kr^+$ and $^{40}Ca^{86}Kr^+$ bands are consistent with this assignment. Table 3-1 lists the line position of observed and calculated transitions for $^{40}Ca^{84}Kr^+$ and $^{40}Ca^{40}Ar^+$ complexes. The observed band origins are used in the determination of the electronic and vibrational constants in the standard formula,

$$\nu(v',0) = T_{eo} + \omega_e'\left(v'+\frac{1}{2}\right) - \omega_e x_e'\left(v'+\frac{1}{2}\right)^2 \tag{3-1}$$

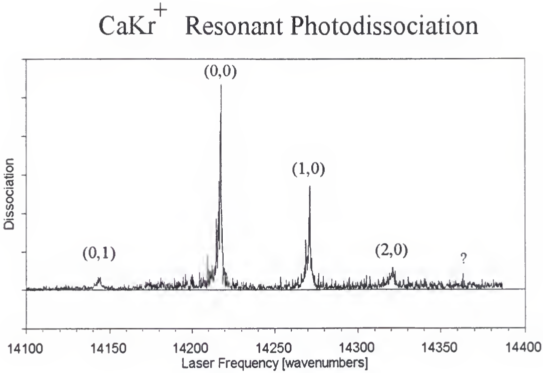

Figure 3-1. Resonant Photodissociation Spectrum of $^{40}Ca^{84}Kr^+$

A portion of the resonant photodissociation spectrum of $CaKr^+$ in the region of the **C-X** transition. The horizontal axis is dissociation laser frequency, in cm^{-1}, and the vertical axis is the Ca^+ photocurrent resulting from the dissociation of mass selected $^{40}Ca^{84}Kr^+$. The vibrational quantum number assignments of the transition are marked in the form: (v',v"). The question mark (?) is placed where the (3,0) transition is tentatively assigned. It should be noted that this spectrum is the composite of a low laser power (right) and a high laser power (left) scan. The 'splice' occurs at ca. 14170 cm^{-1}, and was made to make the hot band more noticeable while not saturating the cold bands. The hot band intensity is exaggerated by about a factor of 5 by this method.

Table 3-1. Line Positions of Assigned C-X Transitions for CaKr^+ and CaAr^+ [cm^{-1}].

$^{40}\mathrm{Ca}^{84}\mathrm{Kr}^+$

V', V"	Observed	Calculated[a]	Obs-Calc
0,1	14143.6	-	
0,0	14217.6	14217.2	0.4
1,0	14271.0	14271.8	-0.8
2,0	14321.6	14321.1	0.4
3,0	14363.0	14365.0	-2

$^{40}\mathrm{Ca}^{40}\mathrm{Ar}^+$

V', V"	Observed	Calculated[a]	Obs-Calc
0,0	14093.0	14093.0	0.0
1,0	14132.7	14132.7	0.0
2,0	14170.6	14170.5	0.1
3,0	14206.3	14206.4	-0.1
4,0	14240.2	14240.3	-0.1
5,0	14272.5	14272.4	0.1
6,0	14302.6	14302.5	0.1
7,0	14330.6	14330.7	-0.1

[a] Fit of observed transitions to Eq. 3-1.

The derived constants for the $^{40}\mathrm{Ca}^{84}\mathrm{Kr}^+$ and $^{40}\mathrm{Ca}^{40}\mathrm{Ar}^+$ ions may be found in Table 3-2. The presence of an upper state vibrational progression as well as the difference in vibrational spacing ($\omega'' > \omega'$) suggests that the equilibrium bond length of the ground state is shorter than that of the excited state.

Figure 3-2 displays a closeup of the origin band of the C-X system. Unfortunately, the combination of limited signal to noise and small rotational

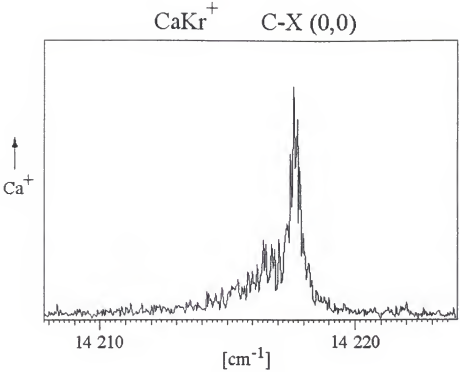

Figure 3-2. The CaAr$^+$ C-X (0,0) Band.

A 'closeup' of the origin band of the **C-X** transition in CaKr$^+$. No rotational structure is evident but the band is clearly red-degraded.

Table 3-2. Molecular Constants [in cm^{-1}] of the Low Lying States of CaKr$^+$ and CoAr$^+$.

CaKr$^+$	T_e	T_{00}	ω_e	$\omega_e x_e$	D_e
X $^2\Sigma^+$ (Ca$^+$ ^{2}S)	-	-	74	-	840±100
C $^2\Sigma^+$ (Ca$^+$ ^{2}D)	14220	14217	60	2.8	330±100
CaAr$^+$	T_e	T_{00}	ω_e	$\omega_e x_e$	D_e
X $^2\Sigma^+$ (Ca$^+$ ^{2}S)	-	-	-	-	890±100
C $^2\Sigma^+$ (Ca$^+$ ^{2}D)	-	14072	42	0.96	525±100

constants of the bands leaves no rotational structure evident. The red-degraded nature of the band is, however, distinctly apparent. This also supports the conclusion that the upper state has a longer equilibrium bond length than the ground state.

The electronic transition observed in Figures 3-1 and 3-2 must be the consequence of a change in electronic state of the Ca$^+$ ion since no Kr excited states (nor charge transfer transitions) are energetically accessible. In fact, the only possible assignment of this transition is a d–s transition at the Ca$^+$ center, which is , of course, parity forbidden in the isolated ion. The two spin-orbit components of the ^{2}D state of the Ca$^+$ ion lie 13650 { $^2D_{3/2}$ } and 13711 { $^2D_{5/2}$ } cm^{-1} above the ground ^{2}S state [9]. Since the electronic origin of the **C-X** transition is some 500 cm^{-1} to the blue of the energy difference in the diabatic dissociation limits, the ground state of the transition must be more strongly bound than the excited state by this amount, consistent with the above discussion. Of the three symmetries of electronic states arising from the upper state dissociation limit ($^2\Sigma^+$, $^2\Pi$, and $^2\Delta$), shown in Figure 3-3, only the $^2\Sigma^+$ state is expected to be more weakly bound than the $^2\Sigma^+$ ground state, and thus the **C** state is assigned this symmetry. The $^2\Pi$, and $^2\Delta$ states, although not observed directly in this study, are expected to lie to lower energy than the **C** $^2\Sigma^+$ state, and are reserved the **A** and **B** designations (see Figure 3-3). As the **C** $^2\Sigma^+$state is diabatically correlated to the $Ca^+(\,^2D_{5/2})$ + Kr (^1S) limit, the difference in binding energies of the **C** and **X** states may be determined from the data in Table 3-2, i.e. $D_e'' - D_e' = T_e - 13711 = 509\ cm^{-1}$.

The diabatic binding energy of the **C** state itself may be crudely estimated in two ways. If the excited state potential is approximately a Morse function, D_e may be estimated as $D_e \cong \omega_e^2/4\omega_e x_e = 320\ cm^{-1}$. For all the electrostatically bound ions that have been studied to date, this approximation has yielded a lower limit to the diabatic dissociation energy [15-19]. When higher vibrational levels are observed a LeRoy-Bernstein analysis [14] of the vibrational first differences for a limiting $1/r^4$ potential has been shown to work very well [18] . For the lowest vibrational levels in the potential, the Leroy-Bernstein plot shows negative curvature for all Metal -Rg^+ ions, and thus this analysis should provide an upper limit to the diabatic dissociation when only these lowest levels are observed. The Leroy-Bernstein analysis of the **C** state gives $D_e \cong 337\ cm^{-1}$, in somewhat surprising agreement with the Morse potential formula.

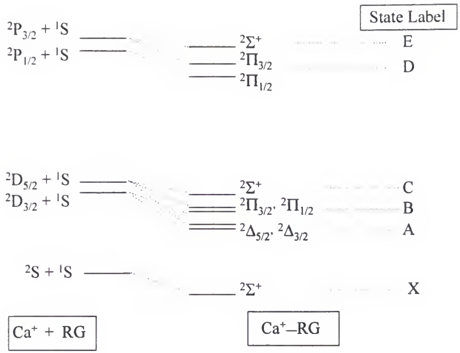

Figure 3-3. Energy Level Correlation Diagram.

The energy level diagram indicating the correlation between atomic calcium cation states and the resulting Ca^+-(rare gas) diatomic molecular ion states [15].

Conservatively, then, the excited state dissociation energy is placed at 330±100 cm^{-1}. Using this value, ground state binding energy of the $CaKr^+$ ion is 840±100 cm^{-1}.

CaAr$^+$

Figure 3-4 shows the **C-X** transition observed in the resonant photodissociation spectrum of $CaAr^+$. This spectrum is inferior to that observed in the krypton analog of this molecule because: (1) The spectrum is 'riding' on a background of the dissociation spectrum of Ca_2^+ (which has the same nominal mass/charge) (2) There are no naturally occurring isotopes of the molecule with sufficient abundance to confirm vibrational assignments by isotopic shifts in the spectrum and (3) no hot bands can be assigned.

Nonetheless, the spectrum in Figure 3-4 is remarkable in likeness to the spectrum displayed in Figure 3-1, and is therefore analyzed in the same way. The position of the origin band as well as the red-degraded band shapes means the upper state is more weakly bound than the ground state. Following the reasoning above, the **C** state is more weakly bound than the ground state by 362 cm^{-1} in this ion. Morse analysis of the vibrational structure gives an excited state binding energy of 450 cm^{-1}, whereas LeRoy Bernstein analysis yields 600 cm^{-1}, so the excited state diabatic binding is taken as 525±100 cm^{-1}. This gives

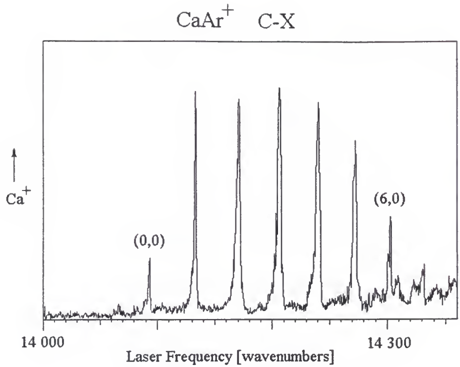

Figure 3-4. Resonant Photodissociation Spectrum of $CaAr^+$.

A portion of the resonant photodissociation spectrum of $CaAr^+$ showing the **C-X** system. The transitions involving v'=1-4 at the center of the figure are saturated and these features should not be taken as representative of the true transition probabilities. The rubble strewn throughout the baseline most likely originates from the (two-photon?) photodissociation of Ca_2^+, which is a contaminant in the ion beam and is not separable by our present mass resolution.

the ground state binding of 890±100 cm^{-1}. A summary of all constants derived for this ion can be found in Table 3-2. In this table the expected accuracies of electronic term energies are ±5 cm^{-1}, vibrational frequencies ±2 cm^{-1}, and anharmonicities ±0.1 cm^{-1}.

Molecular ions consisting of alkali-earth metal ions and rare-gas atoms have been studied before. The rare-gas (Rg = Ar, Kr, Xe) complexes of the Mg$^+$ ion have been extensively studied [15,16,20,21] via resonant photodissociation spectroscopy. Panov et al. [22] have studied the BaAr$^+$ molecule by laser fluorescence excitation at high resolution, as well as dispersed fluorescence. These studies found electronic transitions in the ions isoelectronic with CaRg$^+$, but corresponding to the np←ns transition in the metal ion not the (n-1)d←ns found here. Note that only the Π states correlating to the np limit were vibrationally and rotationally resolved in either study.

The ground state of CaKr$^+$ is much more weakly bound than its magnesium analog, MgKr$^+$ (840 vs. 1831 cm^{-1}) and has a correspondingly lower vibrational frequency (74 vs. 112 cm^{-1}). The binding energy of CaAr$^+$ determined in this study (890 cm^{-1}) lies intermediate between the binding energy of the lighter MgAr$^+$ ion (1189 cm^{-1}) and the heavier BaAr$^+$ molecule (680 cm^{-1}). The vibrational frequency in the ground state of MgAr$^+$ (96 cm^{-1}) is greater than that of BaAr$^+$ (61.7 cm^{-1}) and the CaAr$^+$ ground state vibrational frequency (66 cm^{-1}) is intermediate as expected. Data shows that dissociation energies decrease and bond lengths increase as the alkaline earth metals get heavier (larger), shown in

Table 3-3. That is, the bond energies decrease for the series: $BeAr^+$ [17] > $MgAr^+$ [20] > $CaAr^+$ [this work and 15] > $SrAr^+$ [23] > $BaAr^+$ [24].

Table 3-3. Ground State Binding Energy (D_o'') of Group II MAr^+ Complexes [cm^{-1}].

System [ref #]	**Config. (M^+)**	**D_o Expt.**
$BeAr^+$ [17]	$2s^1$	4112
$MgAr^+$ [20]	$3s^1$	1281
$CaAr^+$ [this work] [15]	$4s^1$	890±100 [732]
$SrAr^+$ [23]	$5s^1$	827
$BaAr^+$ [24]	$6s^1$	680

The indication that the binding energy of $CaKr^+$ is almost the same as that of $CaAr^+$ (Table 3-2) runs counter to previous experience with alkali, alkali-earth, and transition metal rare gas ion complexes. Moreover, a comparison of the **C** $^2\Sigma^+$ excited states in $CaAr^+$ and $CaKr^+$ shows a greater vibrational frequency in the krypton species and a greater diabatic binding energy in the argon species; Both of these observations seem odd. However, the recent photodissociation study by Duncan *et al* [21] of the parity allowed p←s transition on Ca^+ (chromophore) in the $Ca(Rg)^+$ diatomics where the Rg = Ar, Kr or Xe indicates the expected trend in the ground state binding energies: 700 ± 100 cm^{-1}, 1400 ± 150 cm^{-1} and 2300 ± 150 cm^{-1} for $CaAr^+$, $CaKr^+$ and $CaXe^+$ respectively. Note that both Duncan's group research and this study yield an identical vibrational frequency of 74 cm^{-1} for the ground state of $CaKr^+$ molecular ion. The discrepancies in the reported binding energies is due to the fact that only few lines were observed in the parity forbidden transition of (n-1)d ← ns versus about ten lines for each of the excited states, $^2\Pi_{1/2}$ and $^2\Pi_{3/2}$ for a very allowed transition p←s on calcium cation. Thus a ground state binding energy of 1400 ± 150 cm^{-1} for $CaKr^+$ is accepted.

At present, on-going research in Brucat group is concentrating on searching for the **A** and **B** ($^2\Delta$ and $^2\Pi$) states arising from the Ca^+ 3d limit, as well as the **E** $^2\Sigma^+$ state derived from the Ca^+ 4p limit. Hopefully, these results will provide an incentive to theoreticians to calculate the spectroscopic properties of $Ca(Rg)^+$ molecular ions.

CHAPTER 4
VIBRONIC ANALYSIS OF COBALT CATION-RARE GAS COMPLEXES

The study of isolated ion-neutral complexes in the gas phase has been of great interest for various scientists [25-40]. These simple systems serve as models for understanding the complex ion-solvent interactions that are found in many biological systems. The nature of the electrostatic binding between a neutral ligand and an ion is not fully characterized, however, the governing attractive force is the charge-(induced dipole).

Progress has been made both experimentally [25-31] and theoretically [32-40] in the last decade on the study of binary metal-(rare-gas) ions. Comparing the binding energy trends of **M^+**(Rg) complexes with M^+(**Ar**) while keeping one partner 'in bold' constant: a direct correlation in the binding energy of metal-(rare gas) ion with increasing size of the rare gas has been established. However, a decrease in binding energy has been verified [20-22] as a function of the metal cation's size for group two metals (s^1 configuration and closed d-shell) also verified in chapter 3. These trends have yet still to be established for transition metal containing molecular ions.

In this chapter a high-resolution photodissociation study of $Co(Rg)^+$ diatomic ions is presented where the rare gas is either Ar, Kr or Xe. The probed transitions are centered on Co^+ as a chromophore and the obtained spectra of the $Co(Rg)^+$ binary ions are a result of either a $d^8 \leftarrow d^8$ or $d^7s \leftarrow d^8$ atomic resonance. The vibronic analysis of the data provides spectroscopic information such as the stretching frequencies, anharmonicities and binding energies. Global comparisons among various metal cation-rare gas systems studied are discussed.

Results

Figure 4-1 shows the resonant photodissociation excitation spectrum of $^{59}Co^{40}Ar^+$ in the range of 12300 to 17400 cm^{-1} and Figure 4-2 shows a portion of the photodissociation excitation spectrum of $^{59}Co^{129}Xe^+$ in the range of 12200 to 17200 cm^{-1}. Simultaneously acquired spectra of the isotopically varied molecular ion, for $CoXe^+$, aid in the assignment of the vibrational quantum number. Six excited states have been assigned and are labeled **a, b, A, B, C** and **D**, in Figure 4-2, for the $CoXe^+$ complex.

The resonant photofragmentation spectrum of $CoAr^+$ shows five analogous band systems(Figure 4-1). For easier comparison, the previously assigned electronic transitions of $CoAr^+$ and $CoKr^+$ have been re-labeled **A-X**, **B-X** and **C-X** [25] as **b-X**, **C-X** and **D-X**, respectively and for $CoAr^+$ states **A", A'** and **B'** [28] as **a, A** and **B** respectively. Note that the **B** state for $CoAr^+$ ion is currently not analyzed due to the presence of obvious perturbations in the spectrum that cause line splittings. The complete analysis of the **B** state awaits either data from the isotopic variant $^{59}Co^{36}Ar^+$ ion or the related molecule $CoKr^+$ (since Kr has many naturally occuring isotopes) for confirmation of the vibrational index. Only four analogous band systems have been observed to date for the $CoKr^+$ system, that is **b, C, D** and **a** [29].

Vibrational Analysis

Table 4-1 lists the assigned line positions of the $^{59}Co(RG)^+$ homologs. The calculated lines are determined from the standard formula,

$$E(v') = T_{eo} + \omega_e'(v'+\frac{1}{2}) - \omega_e X_e'(v'+\frac{1}{2})^2 + \omega_e Y_e'(v'+\frac{1}{2})^3 \tag{4-1}$$

where T_{eo} is the electronic term energy relative to the zero point level of the ground state, ω_e' is the stretching frequency, $\omega_e x_e$' and $\omega_e y_e$' are the first and second anharmonicities, respectively. The spectroscopically determined molecular constants are given in Tables 4-2, 4-3 and 4-4 for $CoAr^+$, $CoKr^+$ and $CoXe^+$ complexes, respectively.

Note that for our spectra the electronic transitions originate from v" = 0 due to the adiabatic expansion the molecular ions suffer prior to photo-interrogation. Hot bands are seldom observed as indicated in Table 4-1. The assignment of the excited state vibrational index is achieved by fitting values of v' to the observed isotope shift using the following equation [41],

$$h\Delta v_{isotopic}(v',v'')=(1-\rho)[\omega_e'(v'+\frac{1}{2})-\omega_e''(v'+\frac{1}{2}))$$
$$-(1-\rho^2)[\omega_e x_e'(v'+\frac{1}{2})^2-\omega_e x_e''(v''+\frac{1}{2})^2] \tag{4-2}$$

where $h\Delta v_{isotopic}$ is the shift for a particular vibrational band as a function of vibrational energy level, ρ is the ratio of the reduced masses, $m = (\mu/\mu_{isotope})^{1/2}$. The ground state molecular constants are either estimated $\omega_e X_e$" = 2.0 cm^{-1} for $CoXe^+$) or determined from observed hot bands (ω_e" = 200 cm^{-1}). Theoretical values can also be used, however, none are available for the $CoXe^+$ system.

Figure 4-3 shows the assignment of the vibrational quantum number for two excited states, A and D to within ±1 vibrational index. Experimental isotope shifts between corresponding bands in the $^{59}Co^{129}Xe^+$ and $^{59}Co^{136}Xe^+$ are plotted as a function of the absolute vibrational index. For the **A** state the measured shifts (in triangles) are in good agreement with the assignment of the first band observed as (4-0) and (1-0) for the **D** state (in squares). The dotted curves in Figure 4-3 indicate the predicted isotope shift for the assignment of the vibrational quantum numbers. The solid curves are the predicitions for the numbering shifted by one vibrational index lower or higher in reference to the absolute assignment.

Figures 4-4, 4-5 and 4-6 show term value plots of the transition frequency as a function of the vibrational quantum number for each of the $Co(Rg)^+$

Table 4-1. Line Position of Assigned Vibronic Transitions [cm^{-1}]

Hot Band a-X	**^{59}Co^{40}Ar$^+$**	**Residual**	**^{59}Co^{84}Kr$^+$**	**Residual**	**^{59}Co^{129}Xe$^+$**	**Residual**
0-1			12318.5?		12317.6	
1-1			12517.6		12553.9	
a-X	**^{59}Co^{40}Ar$^+$**	**Residual**	**^{59}Co^{84}Kr$^+$**	**Residual**	**^{59}Co^{129}Xe$^+$**	**Residual**
0-0	12551.8		12553.6		12575.0	
1-0					12733.1	
A-X	**^{59}Co^{40}Ar$^+$**	**Residual**	**^{59}Co^{84}Kr$^+$**	**Residual**	**^{59}Co^{129}Xe$^+$**	**Residual**
0-0	12505.0	0.91				
1-0	12600.3	0.23				
2-0	12691.2	-0.59				
3-0	12778.4	-1.02				
4-0	12862.9	-0.06			13504.1	-1.07
5-0	12942.5	-0.08			13621.5	1.25
6-0	13018.2	-0.11			13733.9	0.42
7-0	13090.0	-0.30			13845.0	-0.02
8-0	13158.3	-0.25			13954.4	-0.39
9-0	13223.3	0.21			14062.7	-0.03
10-0	13284.5	0.37			14169.0	0.04
11-0	13342.2	0.56			14273.2	-0.19
12-0	13396.1	0.42			14376.1	-0.02
13-0	13446.9	0.42			14477.0	-0.16
14-0	13494.5	0.50			14576.4	0.04
15-0	13538.8	0.47			14673.2	-0.62
16-0	13579.7	0.21			14769.8	0.27
17-0	13616.4	-1.28			14863.9	0.44
18-0	13652.8	-0.13			14956.3	0.58
19-0	13685.0	-0.33			15046.1	-0.17
20-0	13713.9	-1.07			15134.6	-0.36

Table 4-1--continued.

A-X	^{59}Co^{40}Ar$^+$	Residual	^{59}Co^{84}Kr$^+$	Residual	^{59}Co^{129}Xe$^+$	Residual
21-0	13740.7	-1.13				
22-0	13768.1	2.05				
23-0	13787.4	-0.37				
24-0	13806.9	-0.08				
25-0	13824.3	0.53				
26-0	13839.6	1.34				
27-0	13853.1	2.54				
28-0	13865.5	4.88				
29-0	13875.8	7.15				
30-0	13884.5	9.92				
31-0	13892.2	13.48				
32-0	13897.4	16.54				
33-0	13902.3	20.96				
34-0	13907.0	26.97				
35-0	13911.4	34.30				
36-0	13913.5	40.81				
37-0	13914.5	47.73				
38-0	13915.7	56.18				

b-X	^{59}Co^{40}Ar$^+$	Residual	^{59}Co^{84}Kr$^+$	Residual	^{59}Co^{129}Xe$^+$	Residual
0-0					13705.5	-0.76
1-0					13868.6	0.94
2-0			13699.0	0.12	14023.9	0.97
3-0			13837.5	-0.08	14172.4	-0.58
4-0			13972.5	-0.94	14318.4	-0.53
5-0			14099.7	-6.54	14459.8	-2.05
6-0			14220.7	-15.31	14605.4	2.77
7-0			14357.5	-1.20	14741.3	-1.14
8-0			14489.2	-5.34	14883.0	0.89

Table 4-1--continued.

B-X	$^{59}Co^{40}Ar^+$	Residual	$^{59}Co^{84}Kr^+$	Residual	$^{59}Co^{129}Xe^+$	Residual
9-0			14604.9	-2.48	15022.3	-0.50
10-0			14625.0	2.97		
11-0	14578.7	0.30	14728.1	-0.66		
12-0	14678.0	0.60				
13-0	14768.7	-2.20	15165.1	-0.46		
14-0	14859.7	0.85	15265.8	-2.22		
15-0	14941.7	0.29	15365.4	-2.03		
16-0			15452.5	-11.14		
17-0	15092.0	0.83	15452.5	11.14		
18-0	15158.5	-0.08	15549.8	-7.04		
19-0	15220.4	-0.64	15637.4	-9.39		
20-0			-	-		
21-0			15814.1	-3.41		
22-0			-	-		
23-0			-	-		
24-0			16043.3	2.87		
25-0	15502.5	0.05				
26-0	15535.7	0.86				
27-0	15565.5	1.93				
28-0	15592.3	3.68				
29-0	15616.2	6.05				
30-0	15637.3	8.98				
31-0	15655.9	12.68				
32-0	15672.2	17.19				
33-0	15686.7	22.84				
34-0	15699.1	29.26				
35-0	15709.9	36.85				

Table 4-1--continued.

B-X	^{59}Co^{40}Ar^{+}	Residual	^{59}Co^{84}Kr^{+}	Residual	^{59}Co^{129}Xe^{+}	Residual
4-0					14228.7	0.18
5-0					14344.6	-0.32
6-0					14459.6	0.04
7-0					14572.7	-0.04
8-0					14684.2	0.05
9-0					14794.1	0.12
10-0					14902.3	0.12
11-0					15008.5	-0.18
12-0					15113.8	0.23
13-0					15216.9	0.12
14-0					15318.4	0.12
15-0					15417.3	-0.84
16-0					15516.4	0.06
17-0					15613.0	0.20
18-0					15707.3	-0.29
19-0					15801.3	0.74
20-0					15891.8	-0.07
21-0					15981.3	-0.23

C-X	^{59}Co^{40}Ar^{+}	Residual	^{59}Co^{84}Kr^{+}	Residual	^{59}Co^{129}Xe^{+}	Residual
2-0			14162.6	1.02		
3-0			14271.6	0.61		
4-0			14378.0	0.25		
5-0			14481.6	-0.25		
6-0	14077.5	0.06	14583.4	0.05		
7-0	14168.7	0.13	14679.2	-3.01	14997.0	-0.09
8-0	14255.7	-0.14	14778.9	0.42	15111.6	-0.85
9-0	14339.4	-0.06	14872.2	0.08	15226.2	-0.08
10-0	14419.2	-0.17	14963.7	0.46	15339.1	0.79

Table 4-1--continued.

C-X	$^{59}Co^{40}Ar^+$	Residual	$^{59}Co^{84}Kr^+$	Residual	$^{59}Co^{129}Xe^+$	Residual
11-0	14495.7	-0.04	15049.5	-2.34	15450.9	2.27
12-0	14568.4	0.02	15137.1	-0.73	15559.3	2.01
13-0	14637.7	0.16	15221.1	-0.21	15662.8	-1.45
14-0	14703.3	0.13	15302.8	0.43	15765.1	-4.37
15-0	14765.2	-0.14	15382.1	1.25	15870.7	-2.31
16-0	14824.0	-0.12	15459.8	2.93	15974.7	-0.24
17-0	14880.2	0.72	15529.4	-1.04	16076.3	1.24
18-0	14931.3	-0.24	15601.3	-0.31	16176.9	3.43
19-0	14980.0	-0.28	15670.5	0.20	16276.0	5.79
20-0	15025.6	-0.11	15739.5	2.91	16365.3	0.15
21-0	15067.7	-0.26	15799.8	-0.62	16450.3	-8.13
22-0	15107.4	0.32	15860.6	-1.32	16544.7	-5.28
23-0	15143.4	0.29	15921.0	-0.04	16649.9	10.03
24-0	15177.0	1.09	15980.2	2.36	16725.0	-2.93
25-0	15207.9	2.16	16032.0	-0.27		
26-0	15236.1	3.45	16083.2	-1.12		
27-0	15261.5	5.01	16134.0	-0.17		
28-0	15285.0	7.50	16182.3	0.62		
29-0	15305.3	9.77	16225.7	-1.22		
30-0	15323.2	12.41	16267.5	-2.44		
31-0	15340.5	17.23	16309.9	-0.71		
32-0	15354.8	21.87	16348.9	-0.25		
33-0	15367.7	27.75	16384.3	-1.14		
34-0	15378.7	34.45	16419.8	0.34		
35-0	15388.2	42.19	16452.7	1.31		
36-0	15396.3	51.16				
37-0	15403.2	61.43				
38-0	15409.0	73.20				

Table 4-1--continued.

C-X	$^{59}\text{Co}^{40}\text{Ar}^+$	Residual	$^{59}\text{Co}^{84}\text{Kr}^+$	Residual	$^{59}\text{Co}^{129}\text{Xe}^+$	Residual
39-0	15413.9	86.43				
40-0	15417.8	101.04				
41-0	15421.0	117.46				
42-0	15425.1	137.01				

D-X	$^{59}\text{Co}^{40}\text{Ar}^+$	Residual	$^{59}\text{Co}^{84}\text{Kr}^+$	Residual	$^{59}\text{Co}^{129}\text{Xe}^+$	Residual
0-0	14545.8	-1.16				
1-0	14715.7	-0.14			15191.3	0.74
2-0	14880.2	1.84			15345.5	-1.15
3-0	15034.8	0.25			15500.9	0.31
4-0	15185.0	0.32	15351.9	0.31	15651.7	-0.48
5-0	15328.7	0.11	15492.9	0.24	15802.1	0.58
6-0	15465.9	-0.53	15630.0	-0.39	15948.6	-0.02
7-0	15598.1	-0.38	15764.5	-0.20	16093.1	-0.32
8-0	15724.3	-0.32	15895.4	-0.18	16236.1	0.28
9-0	15844.7	-0.28	16022.5	-0.70	16376.5	0.50
10-0	15959.7	-0.06	16147.1	-0.22	16513.9	-0.02
11-0	16069.0	-0.01	16267.5	-0.70	16649.1	-0.35
12-0	16172.5	-0.21	16384.3	-1.40	16782.8	0.14
13-0	16271.0	-0.13	16499.7	-0.15	16913.3	-0.32
14-0	16364.4	0.23	16611.3	0.51	17042.1	-0.12
15-0	16452.3	0.23	16718.0	-0.44	17168.6	0.12
16-0	16535.0	0.13	16822.5	-0.33	17292.5	0.11
17-0	16612.8	0.18	16924.0	0.04		
18-0	16685.6	0.12	17021.7	-0.18		
19-0	16753.6	0.11	17117.0	0.36		
20-0	16816.9	0.05	17208.7	0.53		
21-0	16875.3	-0.17	17296.5	-0.05		
22-0	16929.4	-0.17	17381.8	-0.03		

Table 4-1--continued.

D-X	$^{59}Co^{40}Ar^+$	Residual	$^{59}Co^{84}Kr^+$	Residual	$^{59}Co^{129}Xe^+$	Residual
23-0	16978.7	-0.56	17463.6	-0.30		
24-0	17024.6	0.07	17542.5	-0.41		
25-0	17065.7	0.17	17618.8	0.04		
26-0	17103.8	1.53	17691.4	-0.11		
27-0	17138.0	3.00	17761.4	0.12		
28-0	17168.7	5.00	17828.0	0.06		
29-0	17196.2	7.72	17891.8	0.20		
30-0	17220.7	11.19	17952.2	-0.09		
31-0	17242.3	15.59				
32-0	17261.6	21.30				
33-0	17278.4	28.03				
34-0	17293.3	36.27				
35-0	17306.3	46.07				
36-0	17317.4	57.22				
37-0	17327.1	70.14				
38-0	17335.3	84.62				
39-0	17342.2	100.83				
40-0	17348.0	118.78				
41-0	17351.9	137.77				
42-0	17356.9	160.47				
43-0	17359.1	183.12				
44-0	17362.6	209.52				
45-0	17363.6	235.88				
46-0	17366.2	266.21				

molecular ions (Rg = Ar, Kr and Xe). Analogous excited states have been labeled with the same letter for cobalt cation-rare gas complexes. Moreover, within each molecular ion (for example $CoXe^+$) the states assigned to a d^7s configuration (**A**, **B** and **C**) of the cobalt cation have parallel vibrational structures and so does the d^8 configurations (**b** and **D**). Note the obvious perturbations between the **b** state and **C** state in $CoAr^+$ and $CoKr^+$ where an accidental degeneracy occurs (the two states cross) and an indication of the same perturbation in the $CoXe^+$ term value plot. There is also a perturbation between the **b** and **B** states of $CoXe^+$.

Dissociation Limits

While the fit to band origins fails at the top of the Morse potential, that is: higher v', see Figures 4-4, 4-5 and 4-6. LeRoy-Bernstein (LB)analysis [14, 42] provides an accurate prediction which leads to the determination of the dissociation limits for the excited states. The LB treatment takes into account the long-range forces of the atoms; and the derivative of the vibrational energy with respect to vibrational index can be approximated as,

$$(\Delta G)(v') = \frac{E(v'+1)-E(v'-1)}{2} \qquad (4\text{-}3)$$

and equates to the dissociation limit by,

$$\Delta G(v')^{\frac{4}{3}} = [D-E(v')]K^{\frac{4}{3}} \qquad (4\text{-}4)$$

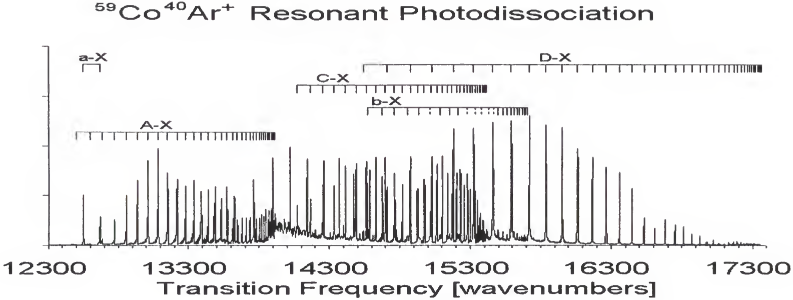

Figure 4-1. Photodissociation Excitation Spectrum of $CoAr^+$.

The resonant photodissociation spectrum of $CoAr^+$. The vertical axis is relative Co^+ photocurrent resulting from the photodissociation of mass selected $CoAr^+$ molecular ion and the horizontal axis is the dye laser frequency. Five excited states are labeled with the tick marks above the spectrum. The dotted lines in the b-X band system represent either missing or perturbed transitions that were not included in the data analysis (see text).

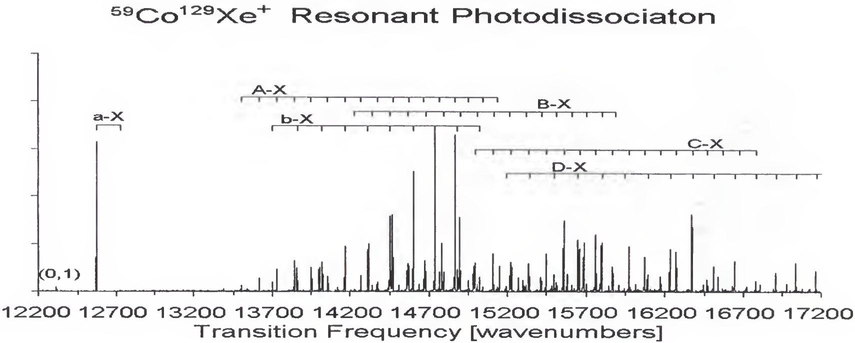

Figure 4-2. The Photodissociation Excitation Spectrum of $^{59}Co^{129}Xe^+$.

A portion of the $^{59}Co^{129}Xe^+$ resonant photodissociation spectrum. The horizontal axis is the dye laser frequency and the vertical axis is relative Co^+ photocurrent coming from the photofragmentation of mass selected $^{59}Co^{129}Xe^+$ ion. Six excited states have been assigned and are labeled with the tick marks above the spectrum. The lower case letters are used to denote spin-forbidden transitions whereas the upper case letters indicate spin-allowed transitions.

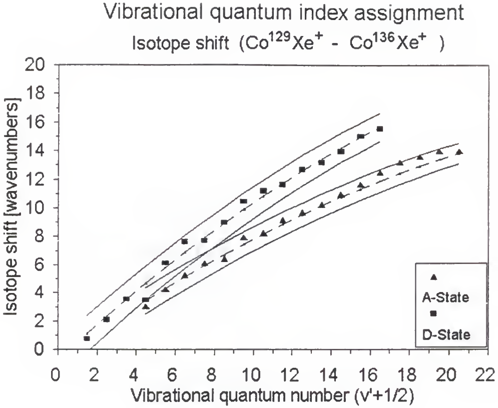

Figure 4-3. Observed and Calculated Isotope Shifts of CoXe$^+$.

The figure shows the vibrational index assignment of the A and D states where the lines are calculated using equation 4-2 and the symbols are observed isotope shifts. The first observed transition for the A-X band system in triangles is (4,0) and for the D-X system it is (1,0) represented in squares. The dashed curve in the middle is in accord with this vibrational quantum number assignment whereas the solid curves were calculated assuming the index was different by ±1 quantum.

Table 4-2. Spectroscopic Constants of $^{59}Co^{40}Ar^{+}$ Complex [cm^{-1}].

Constant	X-State	a-State	b-State	A-state	C-State	D-State
T_{00}	-	12552	13193	12505	13451	14549
w_e	-	~120.5	155.2	100.2	118.6	175.4
w_ex_e	-	-	2.41	2.15	2.04	3.26
w_ey_e	-	-	-	0.01	0.007	0.02
k ($N.m^{-1}$)	-	~20.4	33.8	14.1	19.8	43.2
D_o	4111	3210	2569	1420	1983	2825
$D_o^{'}$ (LB)	4111	-	15759	13922	15432	17369
$-K^{4/3}$ (LB)	-	-	-0.4429	-0.4148	-0.4155	-0.4433
Co^{+} Energy (config.)	0 $^3F_4$ (d^8)	11651.48 $^1D_2$ (d^8)	11651.48 $^1D_2$ (d^8)	9812.96 $^3F_4$ (d^7s)	11321.96 $^3F_2$ (d^7s)	13260.77 $^3P_2$ (d^8)
Ω	3	2	-	4	2	-
Term Symbol	$^3\Delta_3$	$^1\Delta_2$	-	$^3\Phi_4$	$^3\Pi_2$	-
r_e (Å)	2.385*	2.458*	-	2.784	2.669	-
B_v	B_0 0.1245	B_0 0.1172	-	B_e 0.0914	B_e 0.0993	-
α_e	-	-	-	-0.00211	-0.00206	-

Note: All excited state D_0 were determined from Eq. [$D_0' = (D_0'' + \Delta E_{atomic}) - T_{00}$]

* r_o

Table 4-3. Spectroscopic Constants of $^{59}Co^{84}Kr^+$ Complex [cm^{-1}].

Constant	X-State	a-State	b-State	A-state	C-State	D-State
T_{00}	-	12553	13413	-	13935	14753
w_e	-	-	147.6	-	117.5	158.5
$w_e x_e$	-	-	1.47	-	1.35	1.76
$w_e y_e$	-	-	(-0.002)	-	0.002	0.002
k ($N.m^{-1}$)	-	-	44.5	-	28.2	51.3
D_o	5405	4503	3644	-	2792	3913
$D_o^{'}$ (LB)	5405	-	17010	-	16730	18658
Co^+ Energy (config.)	0 $^3F_4$ (d^8)	11651.48 $^1D_2$ (d^8)	11651.48 $^1D_2$ (d^8)	9812.96 $^3F_4$ (d^7s)	11321.96 $^3F_2$ (d^7s)	13260.77 $^3P_2$ (d^8)
Ω	3	2	-	4	2	-
Term Symbol	$^3\Delta_3$	$^1\Delta_2$	-	$^3\Phi_4$	$^3\Pi_2$	-
r_o (Å)	2.447	2.452	-	-	-	-
B_v	B_0 0.0813	B_0 0.0810	-	-	-	-

Note: All excited state D_0 were determined from Eq. [$D_0' = (D_0'' + \Delta E_{atomic}) - T_{00}$]

Table 4-4. Spectroscopic Constants of $^{59}Co^{129}Xe^{+}$ Complex [cm^{-1}].

	X-State	a-State	b-State	A-state	B-state	C-State	D-State
T_{00}	-	12575	13711	13028	13748	14142	15033
w_e	~257	~237	158.2	123.9	124.3	128.9	160.7
$w_e x_e$	-	-	1.29	0.888	0.786	0.837	1.13
$w_e y_e$	-	-	-	0.0003	(-0.0013)	(-0.00034)	(-0.0009)
k (N.m^{-1})	157	134	59.5	36.1	36.8	39.6	61.6
D_o	7700	6776	5640	4485	-	4880	5929
D_o^{*} (LB)	7700	-	-	17629	18404	-	20890
$-K^{4/3}$ (Calc)	-	-	-	-0.1935	-0.1958	-	-0.1923
Co^{+} Energy (config.)	0 $^3F_4$ (d^8)	11651.48 $^1D_2$ (d^8)	11651.48 $^1D_2$ (d^8)	9812.96 $^3F_4$ (d^7s)	-	11321.96 $^3F_2$ (d^7s)	13260.77 $^3P_2$ (d^8)
Ω	3	2	2	4	-	2	-
Term Symbol	$^3\Delta_3$	$^1\Delta_2$	?($^1\Delta_2$)	$^3\Phi_4$	-	$^3\Pi_2$	-
r_o (Å)	2.880	2.883	-	-	-	-	-
B_v	B_0 0.0502	B_0 0.0501	-	-	-	-	-

Note: All excited state D_0 were determined from Eq. [$D_0' = (D_0'' + \Delta E_{atomic}) - T_{00}$] and all LB dissociation limits were determined via long-extrapolation and setting the slope to the theoretical value.

Equation 4-4 is in a suggested form for electrostatically bound complexes, for which the primary forces are charge-(induced dipole). Note that the L-B analysis is, however, independent of the precise vibrational numbering. A plot of $\Delta G(v')^{4/3}$ versus transition frequency, E(v'), should be linear at high vibrational numbers of the excited state (as shown in Figure 4-7, for $CoAr^+$ complex) and can be extrapolated to zero on the vertical axis in order to give the dissociation limit. The $CoAr^+$ dissociation limits shown in Figure 4-7 are referenced to the zero point energy of the ground electronic state of the ion and must be separated by the energy difference between corresponding states in the isolated Co^+ atomic ion Figure 4-8 [43]. (Argon is not energetically accessible in this energy range). The assignments of the excited states are then made based on the agreement and are listed in Tables 4-2, 4-3 and 4-4. Therefore LeRoy-Bernstein analysis of the vibrational structure of the upper state in an electronic transition yields the diabatic dissociation limit of that state which in turn can be assigned to an atomic resonance from which the transition on the chromophore (Co^+) arises.

The analogous states in the $Co(Rg)^+$ homologs have been assigned to the same limits as $CoAr^+$ molecular ion. The LB protocol has been applied to all available vibrational information in the $CoAr^+$ (as discussed above) however, for both $CoKr^+$ and $CoXe^+$ only lower energy levels of the potential were probed thus a long-extrapolation to the dissociation limit of the probed state became necessary. Figure 4-9 shows such a modification of a LB plot for the observed

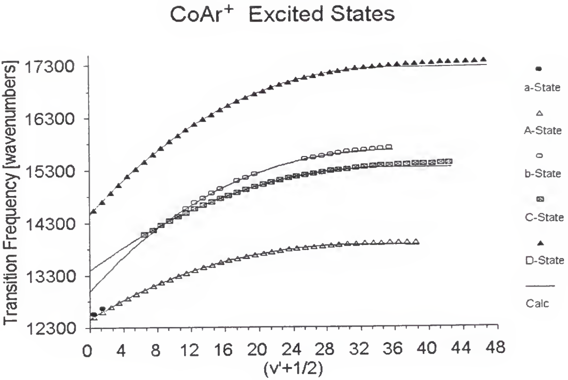

Figure 4-4. CoAr$^+$ Fit to Band Origin.

The assigned excited states are represented with symbols and labeled (on the right). The solid curves are the least-squares fit to Eq.1 of the observed vibrational band origins. Note that the a-state has no curve through the data since only two transitions were observed for this band system, thus, not enough experimental points to do the same data analysis as the other excited states. The b and D states have similar vibrational structure since they both arise from a d^8 cobalt cation configuration, whereas, the A and C states are also similar arising from a d^7s atomic ion configuration. The vibrational structure of a-state is uncertain.

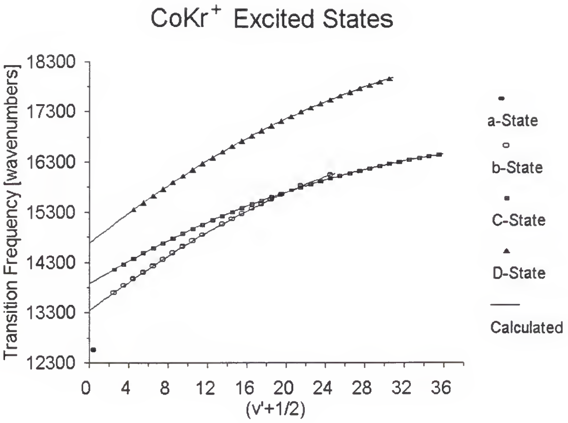

Figure 4-5. CoKr$^+$ Fit to Band Origin

In the figure assigned excited states are represented with symbols and labeled (on the right). The solid curves are the least-squares fit to Eq.4-1 of the observed band origins and the residuals (observed minus calculated) are tabulated in Table 4-1. Note that the a-state has no curve through the data since only one transition was observed for this band system, thus, not enough experimental points to do the same data analysis as the other excited states. The vibrational structure of CoKr$^+$ resembles that of the probed analogous states in CoAr$^+$ complex. In both molecular ions obvious perturbation in the b and C states is indicated by an accidental degeneracy in the vibrational energy level (potentials cross).

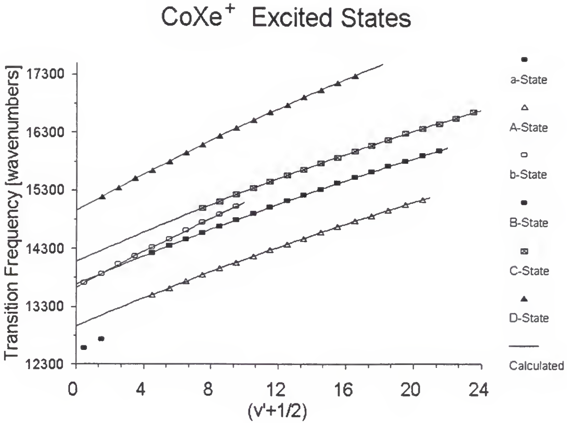

Figure 4-6. CoXe$^+$ Fit to Band Origin.

The assigned excited states are represented with symbols and labeled (on the right). The solid curves are the least-squares fit to Eq.1 of the observed vibrational band origins. Note that the a-state has no curve through the data since only two transitions were observed for this band system. Note once again b and D states have similar vibrational structure (d^8 cobalt cation configuration), while, the A, B and C states are also similar arising from a d^7s atomic ion configuration. The vibrational structure of a-state is uncertain, but it is believed to arise from a d^8 configuration of cobalt ion based on rotational information (see text).

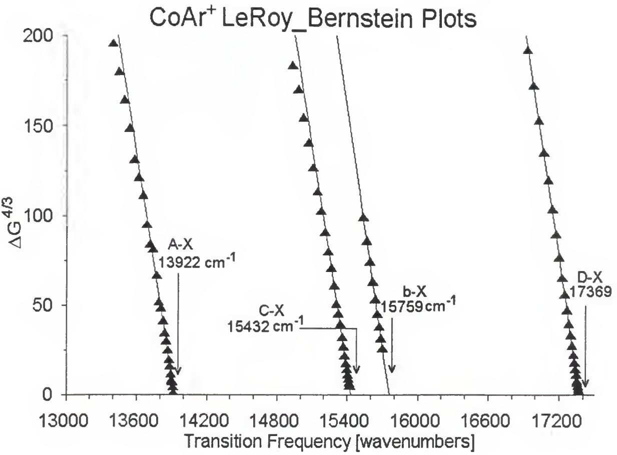

Figure 4-7. CoAr$^+$ Dissociation Limits.

LeRoy-Bernstein analysis with the progressions labeled. A linear plot of $\Delta G(v')^{4/3}$ as a function of transition frequency is obtained when a $1/r^4$, charge-(induced-dipole)limiting form of the potential is assumed. Dissociation limits at which each of the excited states vibrational energy levels converge are indicated.

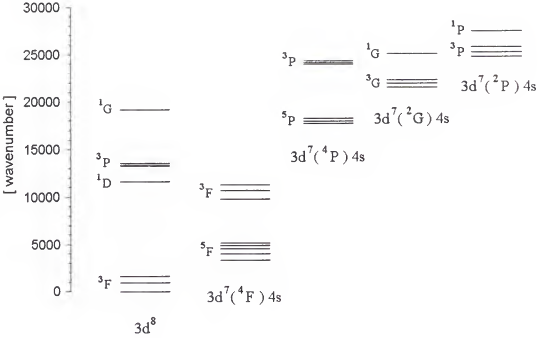

Figure 4-8. The Low-Lying Atomic States of Co$^+$ [43].

transitions in the $CoXe^+$ A-X system. This method overestimates the diabatic limit of the A-state thus the limit at 17 629 cm^{-1} is an upper limit while the fit to a hypothetical Morse potential yields a lower limit at 17 412 cm^{-1} (Birge-Sponer limit). The actual limit is determined as, 17 520 cm^{-1}, an average of these two values.

Figure 4-10 shows a correlation diagram between the force constant (k) and the binding energy (D_o') and it is related to Badger's rule [44]. The a- and X-states have been eliminated in this analysis because of the relative larger uncertainty in the measured vibrational frequency. It is compelling to note that all the $Co(Rg)^+$ homologs have parallel behavior.

Discussion

Tables 4-2, 4-3 and 4-4 show the experimental binding energies of various states of the Co^+ ion with the rare gases Ar, Kr and Xe from the analysis of the spectra of the $Co^+{\cdot}Rg$ electrostatic complexes. Note that the states which arise from the $3d^8$ atomic ion configuration are more strongly bound than those arising from the $3d^74s$ configuration consistent with simple electrostatic arguments. Tables 4-2, 4-3 and 4-5 also show the symmetry assignments of some of the states observed in these molecules where this can be made unambiguously. The ground state of all of these species is expected to be $^3\Delta_3$ from molecular orbital arguments as well as *ab initio* theory [36] and this is

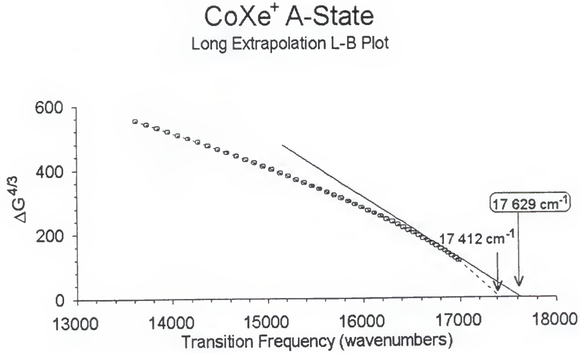

Figure 4-9. The Long Extrapolation of a LeRoy-Bernstein Plot.

Two dissociation limits of the A-state [lower (Birge-Sponer fit) and upper (LeRoy-Bernstein fit) limit] are shown. Symbols indicate experimental data, the solid line represent the LB predicted line (with a theoretical slope of -0.193) and the dotted curve represents results of a hypothetical Morse potential function with constants of Table 4-4c.

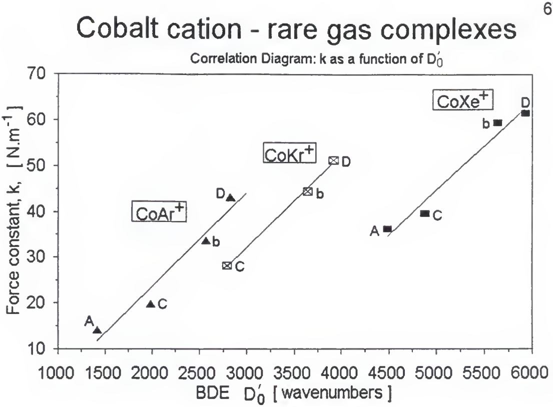

Figure 4-10. Correlation Diagram: k as a Function of D_0'.

A plot of excited states force constants as a function of their binding energy (D_0'). Analogous states have been labeled with the same alphabet and the linear dependence of the molecular ion's stretching frequency on its binding energy is indicated. All three $Co(Rg)^+$ homologs have the same slope.

consistent with the observed rotational structure of the **a**-**X** transition [29]. The **a** state is assigned as $^1\Delta_2$ arising from the ^{1}D Co$^+$ limit although $^3\Pi_2$ symmetry arising from the ^{3}P Co$^+$ limit is, at first glance, also a possibility. This latter assignment is rejected because it would place the upper state binding energy significantly greater than that of the ground state, inconsistent with the smaller vibrational frequency and greater bond length of the **a** state with respect to the **X** state. The $^3\Pi_2$ assignment is also rejected on the basis of the overall intensity of the **a**-**X** electronic transition which is consistent with a Hunds case (a) spin-forbidden transition. The **A** state is assigned as $^3\Phi_4$ as this is the only Ω"=4 state arising from the $^3F_4$ Co$^+$ limit to which the state is known to converge.

Note that although the ground (**X** $^3\Delta_3$) state and the low-lying excited (**a** $^1\Delta_2$) state both arise from a 3d^8 Co$^+$ atomic ion configuration, the bond strengths of the two states differ by -17% in CoKr$^+$, with the ground state being the more strongly bound. This, too, is consistent with simple molecular orbital arguments which predict slightly greater repulsion in the $^1\Delta_2$ than the $^3\Delta_3$ states due to the contribution of ππ hole states in the former configuration. In CoKr$^+$, however, the bond lengths of the two states differ by only 0.2%.

The ground state predicted by *ab initio* theory [36] for CoAr$^+$ is $^3\Delta_3$ with a binding energy of D_0 = 0.402 eV (3240 cm^{-1}) when corrected for zero point and spin-orbit effects. Experiment [28] has confirmed this assignment of the ground electronic state for CoAr$^+$ but with a somewhat greater binding energy of 4111 cm^{-1}. As the binding of Co·Rg$^+$ molecules is primarily electrostatic, the ground state is formed from the electronic configuration of the open-shell metal ion that minimizes bond-axis electron density and thus minimizes repulsion with the polarizable rare gas atom. Of the low-lying configurations of the Co^+ ion, the d^8 (ground state) is expected to be more strongly bound to Ar than the excited d^7s configuration based on its smaller effective ionic radius. The observed spectra of $CoKr^+$ and $CoXe^+$ confirm that they too have a $^3\Delta_3$ ground state.

The optical spectrum of $CoAr^+$, $CoKr^+$, and $CoXe^+$ in the region around 12 550 cm^{-1} are remarkably similar and, in fact, all show the same **a-X** electronic system. Remember that this system is a transition between two terms of the Co^+ ion that arise from the same electronic configuration but in the case of the ground state the 2 d-holes are triplet coupled and in the excited state they form a singlet. It is then interesting to compare the properties of the **a** and **X** states. The change in bond strength upon **a-X** excitation is greatest for $CoAr^+$ (nearly -22%), intermediate for $CoKr^+$ (-17%) and least for $CoXe^+$ (-12%) with the ground state being stronger bound. The difference in equilibrium bond length between the **a** and **X** states is greater in $CoAr^+$ (+3.1%) [28] than in $CoKr^+$ (+0.2%) [29] with the singlet state having the greater r_0. None of the bond lengths of the states in $CoXe^+$ are accurately known at this time.

By comparing the relative bond lengths of Ar and Kr complexes for the same state of the Co^+ ion, relative effective sizes of the rare gases in an ionic environment can be probed. The ground state bond length of $CoAr^+$ ($r_0 = 2.385 \pm 0.005$ Å) is only slightly shorter than that of $CoKr^+$ ($r_0 = 2.447 \pm 0.005$ Å).

This implies the effective radius of Krypton is only 0.062 Å greater than Argon in that state, yet the difference in their vdW radii is on the order of 0.2 Å [30], over three times greater than this dimension. Comparison of the effective rare-gas radii in the excited (**a** $^1\Delta_2$) state implies that the Krypton is smaller than the Argon by .006 Å! This may be an indication of covalency in this excited state.

As expected Table 4-5 indicates that the binding energy of cobalt cation-rare gas complexes increases as a function of the rare gas size for both ground and excited states. Xenon being the most polarizable gas thus more highly bound. Comparisons of analogous states (**b**, **C** and **D**, Figure 4-10) for the $Co(Rg)^+$ homologs show a direct proportionality with force constant and binding energy.

Table 4-5 summarizes the ground state binding energies obtained from both experiment and theory of the binary $M(Rg)^+$ complexes studied. Experimental methods test the theoretical predictions of the important properties of chemical interactions of these and other transition-metal ion clusters. The accuracy of experiment is still far better than the best theory, when it is available at all. It is hoped that complete experimental detail regarding a class of charge-(induced-dipole) bound open d-shell systems such as those described above will provide a useful benchmark for empirical and *ab initio* theory. Currently, computed binding energies are consistently 20 % less than the experimental measurements.

Table 4-5. Ground State Binding Energy, D_o'', of $M(Rg)^+$ Ions [eV].

Metal cation in $M(RG)^+$	**M^+ configuration**	**MAr^+**		**MKr^+**		**MXe^+**	
		Expt.	**Calc.**	**Expt.**	**Calc.**	**Expt.**	**Calc.**
Zr^+	$4d^3$	0.335[a]					
V^+	$3d^4$	0.369[b]	0.312[c]	0.474[b]		0.650[b]	
Nb^+	$4d^4$	0.385[d]		0.571[r]		0.721[r]	
Cr^+	$3d^5$	0.290[e]	0.232[c]				
Fe^+	$3d^6 4s$		0.245[g]		0.415[g]	0.390[f]	0.615[g]
Co^+	$3d^8$	0.508[h]	0.406[c]	0.669[h]		0.955*	
Ni^+	$3d^9$	0.567[i]	0.450[j]				
Cu^+	$3d^{10}$		0.379[j]		0.571[j]		0.624[k]
Ag^+	$4d^{10}$						0.374[k]
Hg^+	$6s$	0.228[l]		0.393[l]		0.748[l]	
Li^+	$1s^2$		0.238[j]		0.309[j]		0.352[k]
Na^+	$2s^2 2p^6$		0.120[j]				0.203[k]
K^+	$3s^2 3p^6$		0.061[j]				0.108[k]
Cs^+	$5s^2 5p^6$	0.240[m]		0.260[m]		0.350[m]	
Mg^+	$3s$	0.159[n]	0.129[o]	0.238[n]	0.231[o]	0.519[n]	
Ca^+	$4s$	0.087[p]		0.173[p]		0.285[p]	
Ba^+	$6s$	0.080[q]					

*this work (a) Ref. 45 (b) Ref. 26 (c) Ref. 32 (d) Ref. 46 (e) Ref. 47 (f) Ref. 48 (g) Ref. 40 (h) Ref. 31 (i) Ref. 18 (j) Ref. 35 (k) Ref. 49 (l) Ref. 50 (m) Ref. 51 (n) Ref.20 (o) Ref 37 (p) Ref. 21 (q) Ref. 22 (r) Ref. 52

CHAPTER 5

RESONANT PHOTODISSOCIATION OF GROUP V $M^+\bullet(Ar)$ COMPLEXES

Metal cation-rare gas complexes, because of their small size and relative simplicity, make them reasonable benchmarks for theoretical investigation which provides some of the motivation for their spectroscopic characterization. The research performed in the Brucat group [26,53] and that of both Duncan and Bauschlicher's groups [21, 22, 36, 37] have consistently indicated that the binding energy of $M^+\bullet(RG)$ complexes increases as a function of the polarizability of the rare gas [see Chapter 4]. On the contrary, trends in the binding energy as a function of the electron configuration of a metal cation are not yet clearly defined given the vast number of metals. In this study experimental spectroscopic parameters for group V cation-Argon molecules are added to the growing list which includes that of already completed group II cation-Argon complexes [23].

By keeping the size of the ligand constant it is feasible to study the changes associated with the different electron configurations of the metal cation. Just as illustrated in the previous chapters, holding the size of the metal cation constant (Ca^+ or Co^+) and varying the ligand (Ar, Kr and Xe) indicated an obvious trend in the molecular ion's binding energy as a function of the rare gas. Xenon atom with the largest polarizability in the given series, has the biggest binding energy (M^{+}•Xe). Some theoretical predictions and experimental observations have harmoniously indicated that a complex containing a transition metal cation with no s-occupation in its ground state was more likely to have a higher binding energy than that with s-occupation. This concept is easily understood, since, for electrostatically bound complexes reducing the number of electrons along the internuclear axis leads to less repulsion, which in turn facilitates getting the ligand to move closer to the point charge (+1) of the metal. For group I and II metal cations complexed with argon an obvious decreasing trend in the adiabatic binding energy as a function of the atomic mass of the metal has been observed and the binding energy values are given in references [36,23] respectively. However, predicting the absolute trend based solely on the occupation of the metal cation for transition metals (with open d-shell occupancy) is not so obvious, as will be illustrated in this chapter. Thus, increasing the number of studied systems would only shed more light to this puzzle.

Data Analysis of Group V (Metal Cation)-(Argon) Complexes

Figures 5-1, 5-2 and 5-3 show resonant photodissociation spectra of the studied M^{+}•Ar complexes. VAr^{+} (Fig. 5-1) and $NbAr^{+}$ (Fig. 5-2) molecular ions have similar features due to vibronic transitions that are centered on the same

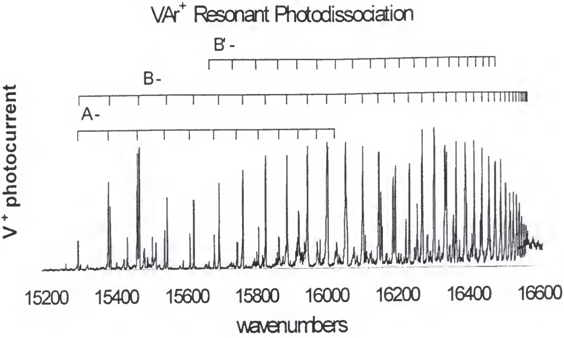

Figure 5-1. Resonant Photodissociation Spectrum of $^{51}V^{40}Ar^+$.

The figure shows three progressions A-X, B-X and B'-X (in VAr$^+$) in the region of 15 200 cm^{-1} to 16 600 cm^{-1}. The vertical axis is the relative V$^+$ photocurrent resulting from the fragmentation of mass selected VAr$^+$ and the horizontal axis is the dissociation laser frequency.

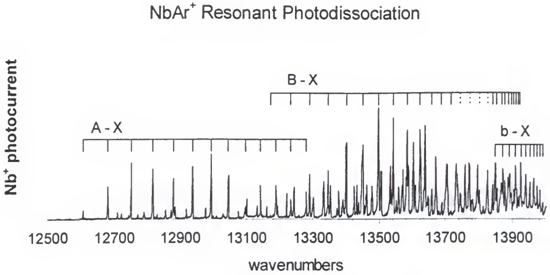

Figure 5-2. Resonant Photodissociation Spectrum of ^{93}Nb^{40}Ar$^+$.

The figure shows three progressions A-X, B-X and b-X (in NbAr$^+$) in the region of 12 500 cm^{-1} to 14 000 cm^{-1}. Tick marks above the spectrum indicate line position of assigned transitions; dotted lines denote missing or grossly perturbed lines. The vertical axis is the relative Nb$^+$ photocurrent resulting from the fragmentation of mass selected NbAr$^+$ and the horizontal axis is the dissociation laser frequency.

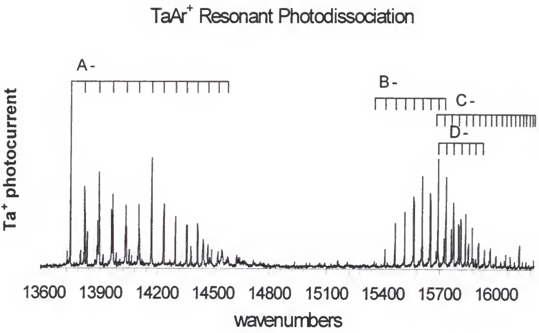

Figure 5-3. Resonant Photodissociation Spectrum of $^{181}Ta^{40}Ar^+$.

The figure shows four progressions A-X, B-X, C-X and C-X (in TaAr$^+$) in the region of 13 600 cm^{-1} to 16 200 cm^{-1}. Tick marks above the spectrum indicate line position of assigned transitions. The vertical axis is the relative Ta$^+$ photocurrent resulting from the fragmentation of mass selected TaAr$^+$ and the horizontal axis is the dissociation laser frequency.

transition, i.e. $nd^3(n+1)s\ (^5P_2)\ B\leftarrow nd^4\ (^5D)\ X$, arising from the transition metal cation chromophore. Preliminary rotational analysis of the photofragmentation excitation spectrum for both VAr^+ and $NbAr^+$ [54] support the assignment of the ground electronic state (X) as $^5\Sigma_0$ which is also in agreement with theory [32]. The photodissociation spectrum of $TaAr^+$ molecular ion (Fig. 5-3) was not rotationally resolvable because of its heavy mass and experimental limitations. However, $TaAr^+$ has a unique spectrum compared to both VAr^+ and $NbAr^+$ due to transitions that originate from a different ground state electron configuration (d^3s) of the chromophore, Ta^+ [9, 55].

VAr^+

The resonant photodissociation spectrum of VAr^+ has been recorded in the visible region from 15100 cm^{-1} to 16 700 cm^{-1}. Figure 5-1 shows the photofragmentation excitation spectrum of VAr^+ with the **A-X**, **B-X** and **B'-X** band systems labeled. Table 5-1 and 5-2 lists the line positions of the assigned vibronic transitions and residuals to the least-squares fit to the standard function (Eq. 3-1) from which the constants T_{eo}, ω_e and $\omega_e x_e$ were derived (Table 5-3). The lack of substantial % of natural occurring isotopes for both vanadium (^{50}V = 0.25 % balance ^{51}V [1]) and argon (^{36}Ar = 0.38 % , ^{38}Ar = 0.63 % balance ^{40}Ar [1]) has constituted to the arbitrary excited state vibrational quantum numbering of VAr^+ complex. Without confirmation of the vibrational index the obtained spectroscopic constants from a fit to Eq. (3-1) are possibly inaccurate. However, a similar spectrum to Fig. 5-1 has been observed in the region 15 700

Table 5-1. Line Positions of group V cation -Argon Complexes [cm^{-1}].

	VAr$^+$		**NbAr$^+$**		**TaAr$^+$**	
v'	**A-X**	**obs-calc**	**A-X**	**obs-calc**	**A-X**	**obs-calc**
0					13741.0	0.52
1					13816.9	-0.79
2	15293.7	-1.82	12606.9	-1.86	13892.9	0.31
3	15380.1	0.19	12680.5	-0.14	13965.6	0.10
4	15462.1	1.33	12751.7	2.31	14037.2	1.03
5	15539.3	1.42	12816.6	1.49	14103.1	-1.67
6	15612.3	0.97	12878.4	0.76	14170.7	-0.40
7	15681.1	-0.02	12936.4	-0.73	14235.3	-0.10
8	15746.5	-0.75	12992.5	-0.88	14297.9	0.44
9	15808.9	-0.88	13044.5	-2.17	14357.9	0.49
10	15867.7	-0.85	13097.2	0.47	14415.8	0.60
11	15922.7	-1.07	13142.9	-0.85	14470.7	-0.06
12	15975.3	-0.01	13189.3	1.61	14524.1	-0.14
13	16024.6	1.47	13234.3	5.86	14575.3	-0.34
14			13280.0	13.90		
v'	**B'-X**	**obs-calc**	**a-X**	**obs-calc**	**C-X**	**obs-calc**
2			11911.2	-0.25		
3			11991.2	0.00	15681.7	-0.16
4			12070.9	1.52	15723.5	0.07
5			12144.4	-1.45	15763.6	0.15
6	15667.9	-1.51	12220.6	-0.14	15801.7	-0.13
7	15735.4	-1.13	12293.3	-0.65	15838.8	0.25
8	15801.9	1.10	12367.3	1.74	15873.8	0.12
9	15864.9	2.71	12434.9	-0.76	15907.0	-0.24
10	15920.9	0.08			15939.1	-0.09
11	15976.9	0.42			15969.3	-0.17
12	16029.8	0.48			15998.3	0.14
13	16078.4	-0.92			16025.5	0.18
14	16127.4	0.97			16050.6	-0.18
15	16169.0	-1.71			16074.6	-0.05
16	16210.6	-1.47			16097.0	0.09
17	16250.9	0.30	b-X	obs-calc	16118.	1.06
18	16286.1	-0.23	13849.2	-	16138.1	1.55
19	16319.0	-0.17	13871.5	-	16155.7	1.76
20	16349.2	0.11	13891.0	-	16172.2	2.49
21	16377.2	0.96	13909.3	-	16187.1	3.17

Table 5-1--continued.

v'	B'-X	obs-calc	a-X	obs-calc	C-X	obs-calc
22	16402.7	2.21	13925.4	-	16199.6	3.11
23	16425.4	3.58	13939.8	-		
24	16445.9	5.48	13952.6	-		
25	16464.6	8.52	13963.9	-		
26	16480.5	11.62	13973.8	-		
27			13982.4	-		
28			13990.3	-		

v'	B-X	obs-calc	B-X	obs-calc	B-X	obs-calc
1	15299.0	-3.88				
2	15384.9	-2.11			15354.5	-0.26
3	15467.2	-0.84			15411.3	0.10
4	15547.3	1.38			15465.2	0.31
5	15623.1	2.42			15516.1	0.24
6	15695.3	2.97	13172.4	0.78	15564.0	-0.03
7	15763.9	3.04	13234.2	0.75	15608.9	-0.46
8	15829.1	2.82	13291.3	-1.08	15651.9	-0.10
9	15890.9	2.32	13346.8	-1.59	15691.9	0.09
10	15948.5	0.72	13401.6	0.18	15729.0	0.12
11	16004.0	0.08	13451.6	0.08		
12	16055.7	-1.18	13498.4	-0.28		
13	16104.2	-2.51	13543.2	0.20		
14	16149.3	-4.16	13584.9	0.58		
15	16195.9	-1.11	13625.9	1.33		
16	16235.7	-1.84	13659.0	0.76		
17	16272.8	-2.14	13704.8*	-1.72		
18	16306.9	-2.32	13732.4*	-4.30		
19	16341.0	0.64	13758.9*	-2.61		
20	16368.9	0.54	13780.1*	0.87		
21	16398.5	5.20	13801.1	9.58		
22	16420.1	5.00	13825.7	16.13		
23	16442.3	8.50	13841.0	16.46		
24	16461.8	12.45	13853.9	17.37		
25	16479.2	17.44	13867.6	21.95		
26	16495.2	24.06	13878.1	26.24		
27	16508.6	31.23	13889.0	33.89		
28	16520.3	39.91	13896.9	41.53		
29	16530.7	50.33	13904.8	52.02		
30	16539.7	62.40	13911.4	64.16		
31	16547.1	76.10	13917.2	78.46		

Table 5-1--continued.

v'	B'-X	obs-calc	a-X	obs-calc	C-X	obs-calc
32	16553.4	91.68	13921.7	94.35		
33	16558.6	109.41				
34	16562.8	129.18				
35	16566.3	151.42				
36	16569.0	175.93				
37	16571.2	203.12				

*Perturbed

Table 5-2. Line Positions of TaAr$^+$ Complex [cm^{-1}].

v'	D-X	obs-calc	E-X	obs-calc
0	15693.5	0.10	17471.4	0.01
1	15734.5	-0.13	17606.9	0.34
2	15775.1	0.10	17728.8	-1.07
3	15814.1	-0.25	17842.3	1.09
4	15852.7	0.00	17940.3	-0.37
5	15890.6	0.43		
6	15926.4	-0.24		

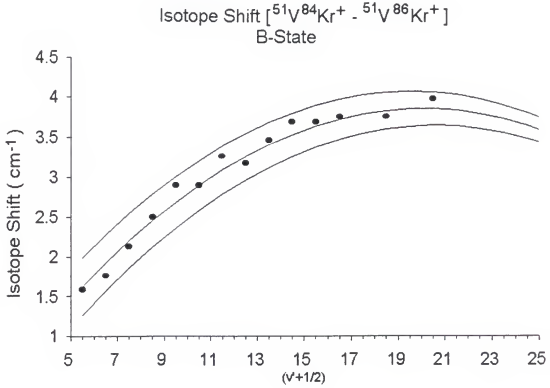

Figure 5-4. Observed and Calculated Isotope Shift of VKr^+.

The figure shows the conformation of the assignment of the B-state vibrational index. Symbols represent experimental observations and the three curves are calculated using equation 4-2. Data and predictions are in agreement that the first observed transition corresponds to (5,0) for (v', v"), middle curve. The higher and lower curves are calculations assuming the index was different by ±1 quantum.

Table 5-3. Spectroscopic Constants for Group V Cation-Argon Molecular Ions [cm^{-1}]

VAr^+	**State**	**T_{eo}**	**ω_e**	**$\omega_e x_e$**	**k**	**$(BS)D_e$**	**$(LB)D_e$**	**$(LB)D_o$***	**$(-K^{4/3})LB$**
	X	-	-	-	-	-	-	2974[a]	-
	A	15068	95.4	1.83	12.0	1243	-	-	-
	B	15171	90.4	1.56	10.8	1310	1406	16577	-0.427
	B'	15163	87.1	1.43	10.0	1326	-	-	-

$NbAr^+$	**State**	**T_{eo}**	**ω_e**	**$\omega_e x_e$**	**k**	**$(BS)D_e$**	**$(LB)D_e$**	**$(LB)D_o$***	**$(-K^{4/3})LB$**
	X	-	-	-	-	-	-	3106[a]	-
	A	12415	81.2	1.55	10.9	1063	-	-	-
	B	12698	82.3	1.46	11.2	1160	1243	13941	-0.374
	a	11705	84.6	0.809	11.8	2212	-	-	-
	b	-	-	-	-	-	-	14026	-0.374

$TaAr^+$	**State**	**T_{eo}**	**ω_e**	**$\omega_e x_e$**	**k**	**$(BS)D_e$**	**$(LB)D_e$**	**$(LB)D_o$***	**$(-K^{4/3})LB$**
	X	-	-	-	-	-	-	≈2000[b]	-
	A	13701	79.3	1.08	12.1	1456	-	-	-
	B	15201	64.8	1.38	8.10	761	-	-	-
	C	15523	48.1	0.806	4.46	718	770	16293	-0.320
	D	15672	42.2	0.48	3.44	928	-	-	-
	E	17399	147	5.96	41.7	906	-	-	-

[a] Suggested value with error ± 10 cm^{-1}

[b] Reasonable estimate with error ± 500 cm^{-1}

k (force constant) in $\mathrm{N.m}^{-1}$

$K^{4/3}$ in $(\mathrm{cm}^{-1})^{1/3}$

cm^{-1} to 17 350 cm^{-1} for VKr^+ [53]. The absolute vibrational numbering of the observed transitions was made possible from measuring the spectral shift among the $V^{82}Kr^+$, $V^{84}Kr^+$ and $V^{86}Kr^+$ isotopomers (shown in Figure 5-4). Thus the effective vibrational index listed in Table 5-1 for VAr^+ was chosen to be close to the absolute value by comparing the VAr^+ to VKr^+ spectrum.

All assigned transitions originate from v" = 0, that is, there are no observed "hot bands". The residuals (observed minus calculated line positions) to the fit show that Eqn. (3-1) is accurate near the bottom of the potential but fails near the top of the well as expected for a system (i.e. $M{\bullet}Ar^+$) for which a Morse oscillator is applied. Figure 5-5 shows that a Morse oscillator (curve) provides an accurate description of the VAr^+ complex (and Figure 5-6 for $V^{84}Kr^+$) for lower v' but under estimates the molecular ion's dissociation energy, D_o^* (Birge-Sponer extrapolation). Symbols represent experimental data points. Striking similarities in the vibrational structure of VAr^+ and VKr^+ excited states are evident. A more reliable procedure for determining the dissociation limit of a state is the LeRoy-Bernstein fit [14, 42] of higher vibrational energy levels and is applied for all the discussed molecular ions (see Determination of Dissociation Limits).

$NbAr^+$

Similar data analysis to VAr^+ were performed. Similarities in the VAr^+ and $NbAr^+$ spectra are due to vibronic transitions that originate from the same transition $nd^3\,(n+1)s\ (^5P_2)$ B←$nd^4\ (^5D)$ X centered on the metal cation

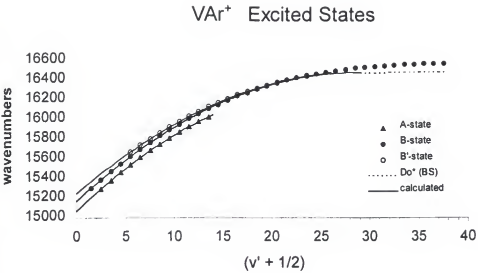

Figure 5-5. VAr^+ Fit to Band Origin.

In the figure three excited states (A, B and B') are labeled with corresponding symbols indicated on the lower right. The curves are calculated using Eq. 3-1; an excellent agreement for lower v' with calculated values is obvious, however, this model fails at higher v' where long-range forces become important. The dashed line, D_0*(BS), indicates a lower dissociation limit predicted by the Birge-Sponer approximation. The true dissociation limit of the excited states is determined by LeRoy-Bernstein analysis.

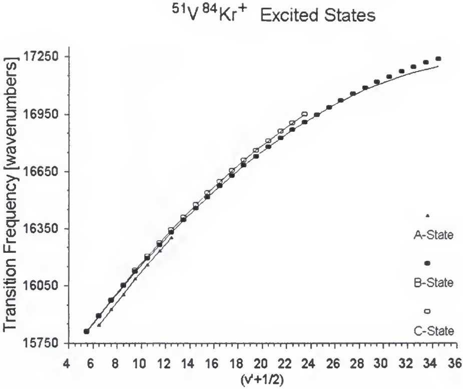

Figure 5-6. $V^{84}Kr^+$ Excited States.

In the figure three excited states (A, B and C) are labeled with corresponding symbols indicated on the lower right. The vertical axis is transition frequency and the horizontal axis is the assigned vibrational quantum number of the excited states. Curves are calculated using Eq. 3-1 and show an accurate prediction at the bottom well an obvious deviation at the top of the potential (higher v') is indicated.

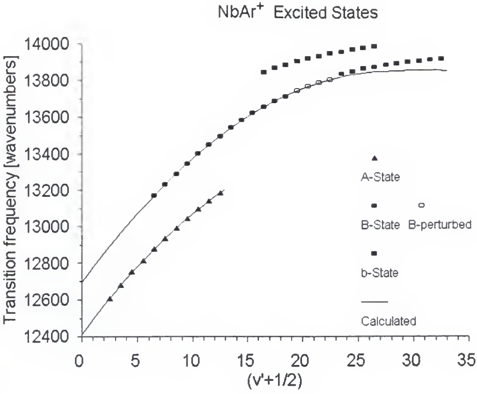

Figure 5-7. Excited States of NbAr$^+$.

This figure shows the assigned states in the region 12400 cm^{-1} to 14000 cm^{-1} of NbAr$^+$. The a-X transitions occur 1000 cm^{-1} to the red of this energy range. The vertical axis is the transition frequency and horizontal axis is arbitrary vibrational quantum index of the excited states. Symbols indicate experimental data points and curves are calculated using the standard formula Eq. 3-1. Perturbations are present (open symbol) in the B-state due to the accidental degeneracy of some of the bands belonging to the b-state convergence band system.

chromophore (V^+ or Nb^+). A portion of the photofragmentation excitation spectrum of $NbAr^+$ (12 500 cm^{-1} to 14 000 cm^{-1}) is shown in Fig. 5-2 and assigned band systems **A-X**, **B-X** and **b-X** are indicated. For the **B-X** progression the dotted lines indicate line positions (marked with asterisks in Table 5-1) that are perturbed thus not included in the regression used to obtain the molecular constants that are listed in Table 5-3. Figure 5-7 shows the vibrational structure of these excited states, however, the vibrational index is arbitrary given that both natural occuring abundances of ^{93}Nb and ^{40}Ar are over 99 % leaving less than 1 % for the other isotopes (which is too small to detect in the Brucat research experimental apparatus). Overall, four vibrational progressions have been identified: their line positions and molecular constants are tabulated in Tables 5-1 and 5-2 , respectively. The labeling of states follow standard procedure where the upper case letters are used to indicate spin allowed transitions and lower case for spin forbidden. Note that for the **b-X** progression some of the spectroscopic constants are not listed due to the fact that all probed transitions for this system were close to the convergence where a fit to equation (3-1) would be inaccurate, thus, only a LeRoy-Bernstein analysis was performed.

$TaAr^+$

The resonant photodissociation spectrum of $TaAr^+$ has been recorded in the near infrared and visible region from 12 150 cm^{-1} to 18 100 cm^{-1}. As expected the $TaAr^+$ spectrum is unique compared to both VAr^+ and $NbAr^+$

spectra as a result of a different electron configuration (d^3s) in the ground state of Ta^+. Figure 5-3 shows a portion of the photofragmentation excitation spectrum in the region 13 500 cm^{-1} to 16 200 cm^{-1} where the **A-X**, **B-X**, **C-X** and **D-X** band systems occur. A 'close-up' of the A-X progression is shown in Figure 5-8, indicating an obvious red degradation of the bands. This observation suggests that , in $TaAr^+$ system, the A-state is less bound than the ground state. Overall, five vibronic band systems were observed for $TaAr^+$ complex in the region 13 500 to 18 500 cm^{-1} (shown in Figure 5-9). Tables 5-1, 5-2 and 5-3 list line positions and spectroscopic constants of the assigned states.

Once again, the lack of natural occurring isotopes for both tantalum and argon has made the absolute vibrational numbering of these systems uncertain. However, band origins ($v' = 0 \leftarrow v'' = 0$) have been identified as the most intense features in the **A-X** , **D-X** and **E-X** progressions thus the excited state vibrational levels are labeled starting from $v' = 0$ (see Figures 5-3 and 5-8). The A, D and E states must have similar r_e values to the ground state which resulted in strongest optimal overlap with the 0-0 transition (v'-v''), thus the most intense vibronic transition observed, based on Franck-Condon principle. The vibrational quantum index for **B** and **C** excited states is arbitrary. Spectroscopic constants for the excited state labeled **E** are the least accurate as only five vibrational energy levels were observed.

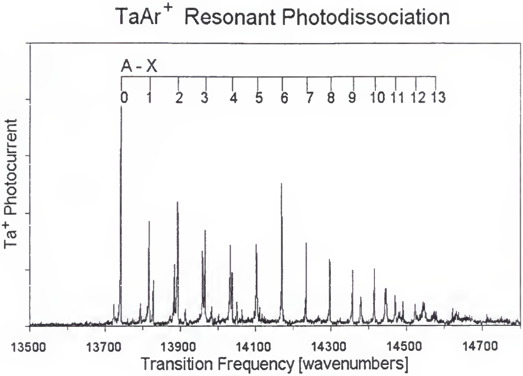

Figure 5-8. The TaAr$^+$ A-X Band System.

This figure shows a "close-up" of Figure 5-3 in the region 13 500 to 14 900 cm^{-1}. The A-X bands are clearly red degraded indicating a longer bond length in the excited state relative to the ground state. Tick marks above the spectrum mark the line positions and the corresponding vibration quantum numbers for the A state are indicated.

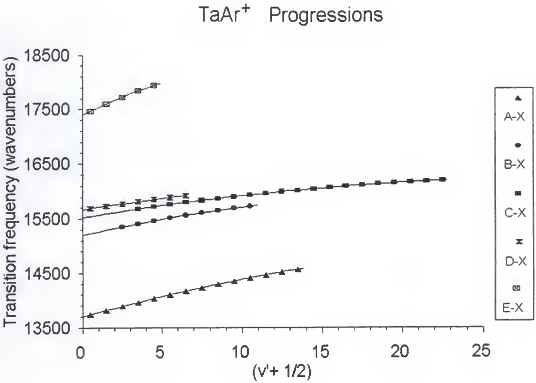

Figure 5-9. TaAr$^+$ Fit to Band Origin.

This figure shows assigned excited states for TaAr$^+$ in the region of 13 500cm^{-1} to 18 500 cm^{-1}. As consistently the vertical axis is the transition frequency (wavenumbers) and the horizontal axis is arbitrary vibrational index of the states. Excellent agreement between experiment (symbols) and prediction (curves) of transitions (Eq. 3-1) is evident.

Note that the labeling of the excited states for $TaAr^+$ molecular ion merely reflects the ordering of the electronic origin (as currently assigned), that is, some of the excited states may be spin forbidden thus would have to be indicated with lower case letters. Detailed analysis of $TaAr^+$ complex is still in progress in our laboratory. Simultaneous acquisition of high-resolution photodissociation spectra of the isotopic variant of $Ta^{40}Ar^+$ (that is, $Ta^{36}Ar^+$) would aid in confirming the vibrational numbering of the excited state vibronic levels and in assigning the diabatic dissociation limits.

Determination of Dissociation Limits

At large internuclear separations, the nature of attractive forces between the separating atoms determine the vibronic structure of the highest bound levels in the potential. LeRoy and Bernstein (LB) have provided a protocol for the analysis of this vibrational structure and accurate extrapolation to the disscoiation limit of the molecule. Figure 5-10 shows such a LeRoy Bernstein plot for the VAr^+ , $NbAr^+$ and $TaAr^+$ molecular ions. The symbols are vibrational first differences obtained from the observed bands in the spectrum and the line is calculated using the expression given by Eq. (4-3). A plot of the derivative of the vibrational energy, $\Delta G(v)^{4/3}$, with respect to the transition frequency, E(v), yields a line with a slope of $-K^{4/3}$ and the dissociation energy at the x-intercept.

Assignment of dissociation limits for VAr^+ and $NbAr^+$ has been presented elsewhere [53, 27] respectively. Briefly, for the $NbAr^+$ complex, the difference between the **B** state limit at 13941 cm^{-1} and the **b** state at 14026 cm^{-1} must correspond to that of the separated Nb^+ atom (Figure 5-11) given that argon has no low-lying electronic states in this energy range. Thus, the atomic states at the **B** and the **b** state limits have been assigned to Nb^+ $^5P_2$ + Ar ^1S (at 10835.85 cm^{-1} [9]) and Nb^+ $^3G_5$ + Ar ^1S (at 10918.52 cm^{-1} [9]), respectively. The ground state dissociation energy for $NbAr^+$ complex is then simply determined by subtracting the matching atomic promotion energy from the diabatic dissociation limit of the assigned state. From this analysis the $NbAr^+$ molecular ion's ground state binding energy is determined to be 3106 $\pm$ 10 cm^{-1}. Assuming that the **B** state in VAr^+ dissociates diabatically to V^+ $^5P_2$ + Ar ^1S, given similar spectral features in both VAr^+ and $NbAr^+$ spectra (Figures 5-1 and 5-2), then the difference between the diabatic dissociation limit at 16 577 cm^{-1} and the assigned atomic promotion energy (V^+ $^5P_2$ + ^1S Ar at 13 594.73 cm^{-1} [9]) yields the ground state binding energy of 2974 cm^{-1} for the VAr^+ complex.

The binding energy of $TaAr^+$ complex is estimated to be 2000 $\pm$ 500 cm^{-1}, further details for this assignment are provided below.

Discussion

The binding energy trends observed in VAr^+ versus $NbAr^+$ parallel those recently found in VXe^+ versus $NbXe^+$ complexes [52]. The advantage of the xenon ligand is that there are several natural occuring isotopes (^{129}Xe, ^{131}Xe, ^{132}Xe , ^{134}Xe and ^{136}Xe) which were used to confirm the absolute vibrational

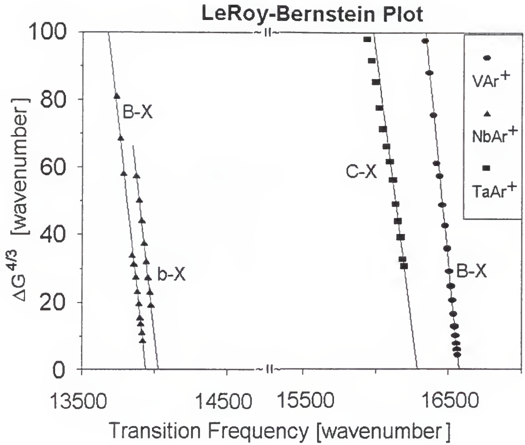

Figure 5-10. LeRoy-Bernstein Plots of Group V (Metal Cation)-Argon Complexes.

This figure shows the extrapolation of vibrational first differences to the diabatic dissociation limit of the labeled states of VAr^+, $NbAr^+$ and $TaAr^+$. This dissociation limit corresponds to the production of excited state fragments. The vertical axis is the vibrational first difference (Eq. 4-3) to the 4/3 power (in cm^{-1}) and the horizontal axis is the observed transition frequency.

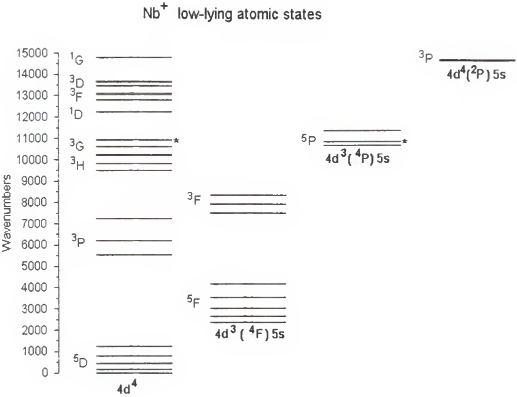

Figure 5-11. Low-Lying Atomic States of ^{93}Nb$^+$ Ion.

This figure shows the positions of low-lying atomic states of Nb$^+$ [9] with the asterics indicating the probed transitions for the **b-X** and **B-X** band systems.

numbering of the excited states in the group V cation-Xenon complexes. The ground state binding energy of Nb^+•(Rg), where Rg is either Ar or Xe, is greater than that of V^+•(Rg) systems, however, the excited states show a reverse trend. Given that the **B** state's diabatic dissociation limit (in both VAr^+ and $NbAr^+$) has been assigned into a M^+ $^5P_2$ + Ar $^1S_0$ limit with d^3s configuration, where M^+ is the metal cation, an argument can be made that the observed trend is due to the radial size of the occupied 4s versus 5s orbital which would contribute to the reduction of the binding energy for $NbAr^+$ molecular ion. The decreasing trend in binding energy as the radial size of the metal cation increases (ns^1 configuration) is also observed for group II cation-Argon complexes [23].

The opposite trend observed in the ground state binding energy is consistent in the argon and xenon ligated complexes. The difference in the ground state binding energy of VAr^+ versus $NbAr^+$ is ≈ 130 cm^{-1} while that between VXe^+ and $NbXe^+$ is ≈ 500 cm^{-1} with the Nb^+•(Rg) complex being more bound. This trend suggests that for open d-orbital with no occupation of the s-orbital the contraction of the d-orbitals which is a function of the number of electrons ($3d^4$ and $4d^4$ for V^+ and Nb^+, respectively) plays a vital role. The exact mechanism or contribution of the orbital contraction to the binding energy of these interesting systems awaits theoretical investigations. However, experimental observations indicate that the simple approach of expecting the binding energy of molecular ions to decrease on moving down a group in the periodic table fails for systems containing no s-occupied orbitals but only electrons in the unfilled d-orbitals, as discussed above. Of course, this conclusion is only based on one example which could as well be an exception. Thus, further investigations on other second row and third row transition metal containing systems are currently being pursued in the Brucat group for an extension of high-resolution photodissociation data in order to verify or predict any existing trends.

The ground state binding energy of $TaAr^+$ molecular ion has been determined based on the following arguments, the dissociation limit of the labeled **C** state predicated by a LeRoy-Bernstein analysis of the observed transitions occurs at 16293 cm^{-1}, shown in Fig. 5-10 and Table 5-3. Literature indicates that the lowest energy level of Ta^+ has a $5d^36s$ electron configuration [9, 59], shown in Figure 5-9 and that there are several atomic lines in the region of 13 000 to 15 000 cm^{-1}. This has made it difficult to assign the C-state to its corresponding atomic limit. If two dissociation limits were observed in the experiment then the information would aid in picking the correct assignment. Due to insufficient information, only an approximation of the adiabatic binding energy of $TaAr^+$ ion can be made.

Table 5-4 lists the known binding energies of M^+•Ar systems with the corresponding electron configuration on the metal cation. Comparisons of the known binding energies are used to estimate or 'guess' the adiabatic binding energy of $TaAr^+$ complex. Unfortunately, only Zr^+ has an s-occupied orbital

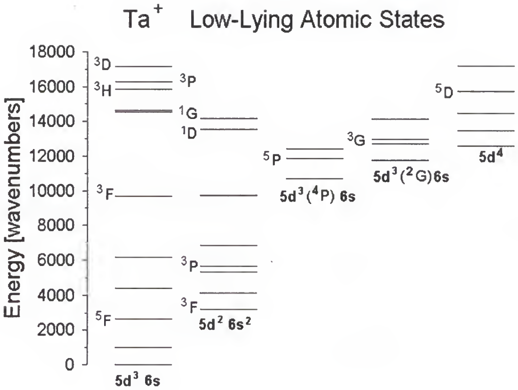

Figure 5-12. Low-Lying Atomic States of ^{181}Ta$^+$ Ion.

This figure shows the positions of low-lying atomic states of ^{181}Ta$^+$ [9, 55].

Table 5-4. Ground States of $M^+ \bullet Ar$ Complexes [cm^{-1}]

System	Config. (M^+)	D_o Expt.	D_o Theory	obs-calc	%error
$LiAr^+$	$1s^2$	-	1919[a]	-	-
$NaAr^+$	$2p^6$	-	967[a]	-	-
KAr^+	$3p^6$	-	492[a]	-	-
$BeAr^+$	$2s^1$	4112[b]	-	-	-
$MgAr^+$	$3s^1$	1270[c]	1041[d]	229	18.0
$CaAr^+$	$4s^1$	736[e]	-	-	-
$SrAr^+$	$5s^1$	827[f]			
$BaAr^+$	$6s^1$	680[g]			
$ZrAr^+$	$4d^25s^1$	2706[h]	-	-	-
VAr^+	$3d^4$	2974[i]	2520[j]	458	15.2
$NbAr^+$	$4d^4$	3106[k]	-	-	-
$CrAr^+$	$3d^5$	2339[l]	1872[j]	467	20.0
$CoAr^+$	$3d^8$	4111[m]	3275[j]	836	20.3
$NiAr^+$	$3d^9$	4572[n]	3872[o]	700	15.3
$TaAr^+$	$5d^3 6s^1$	≈2000[p]	-	-	-
$HgAr^+$	$6s^1$	1839[q]	-	-	-

[a]ref.35, [b]ref.56, [c]ref.19, [d]ref.37, [e]ref.21, [f]ref.23, [g]ref.22, [h]ref.44, [i]ref.53, [j]ref.32, [k]ref.27, [l]ref.57, [m]ref.18 , [n]ref.28, [o]ref.36, [p]this work and [q]ref.49

($4d^25s$) and the binding energy of $ZrAr^+$ complex is 2706 cm^{-1} [44] and $TaAr^+$ (Ta^+, $5d^36s$) is the first spectroscopically studied third row containing transition metal system. Given the observed trends in Table 5-4; an occupied 6s orbital would be expected to have a smaller binding energy than a 5s orbital because of its larger radial size. However, there are competing factors, the $3d^4$ configuration of $V^+ \bullet (Rg)$ proved to be less bound than the $4d^4$ configuration of $Nb^+ \bullet (Rg)$ systems, thus a $5d^3$ configuration would be expected to have a higher binding energy than a $4d^2$ configuration (provided this trend is consistent). In addition, as a general trend, increasing the number of electrons in the d-orbital tend to increase the d-subshell contraction due to increasing the atomic number which consequently leads to a smaller ion thus larger binding energy as indicated for $\mathrm{Var}^+ < \mathrm{CoAr}^+ < \mathrm{NiAr}^+$ series, Table 5-4. This trend shows an anomaly at $3d^5$ for the Cr^+ atom, but in order for the molecular ion to preserve high spin the chromium cation must present a $3d\sigma$ molecular orbital to the argon ligand, in contrast to $3d^4$ V^+. An electron along the bonding axis causes repulsion between the two atoms which in turn results in a reduction in binding energy counter to the overall increase in bond energy with d-orbital contraction.

Given the above speculations it would not be unreasonable to anticipate a binding energy in the region of 1500 cm^{-1} to 2500 cm^{-1} for $TaAr^+$ molecular ion. In keeping with this hand waving argument (provided above) the estimated binding energy of $TaAr^+$ ion is 2000 ± 500 cm^{-1}.

For M^+Ar complexes whose bond length has been determined or calculated, it is possible to evaluate the energetics of the inductive binding in the $M^+{\cdot}Ar$ ion complex through the application of the charge-induced dipole force equation, $q^2\alpha/2r^4$, and a choice of the charge (q) on the metal and the 'ligand' polarizability (α). The charge is assumed to be that of a full electron (positive) charge situated on the metal center. Two possible choices exist for the value of the dipole polarizability of argon, the exact bulk value 1.66 Å^3 [58] and a slightly lower value, 1.48 Å^3, found to be indicative of the effective dipole polarizability in the inhomogeneous field of a point charge in an ion complex (Chapter 6).

Table 5-5 lists the charge-(induced-dipole) energy (**q-μ^{IND}**) at the best-estimate bond length of several M$^+$·Ar complexes for each of the two choices of polarizability. Table 5-4 shows that the charge-(induced-dipole) attraction, (**q-μ^{IND}**), accounts for about **only 60%** of the total binding energy of the **transition-metal** ion complexes whereas this force accounts for **all** of the binding (100%) in **alkaline-metal** ion complexes. Note that if the bulk value of the dipole polarizability is used, the (**q-μ^{IND}**) value calculated is actually larger than the true bond energy (with the exception of BeAr$^+$ where both polarizabilities overestimate the binding energy). Based on this observation we suggest that the authors consider using an α = 1.48 Å^3 in predicting the LeRoy-Bernstein slope for group II cation-Argon complexes.

What is the difference between the group II cation-Argon complexes and all the other ions? The M$^+$ ion in its ground state is alkali-like in electron configuration, ns^1, so it has significant repulsion to inductive binding and thus the longest bond length with Ba$^+$•Ar having the smallest binding energy of all the studied complexes, Table 5-5. Nonetheless, Zr$^+$•Ar too has a metal 5s-electron occupancy in its ground state. Yet the binding energy of ZrAr$^+$ is over three times as large as that of Sr$^+$•Ar which also has a 5s-electron. Additional binding forces in the transition metal ion complexes associated with the open d-shell valence appears plausible. However, the charge donation from ligand to metal

Table 5-5. Charge-(induced-dipole) Contribution to the Ground State Binding Energy of $M^+ \cdot Ar$

Molecular Ion	**VAr^+**	**$NbAr^+$**	**$CoAr^+$**	**$NiAr^+$**	**$ZrAr^+$**	**$BeAr^+$**	**$MgAr^+$**	**$BaAr^+$**
[ref #]	**[53]**	**[27]**	**[28]**	**[18]**	**[45]**	**[56]**	**[59]**	**[22]**
D_o'' (cm^{-1}) expt.	2975	3106	4111	4572	2706	4112	1259	680
r_o'' (Å) expt.	2.645[c]	2.635	2.385	2.374[c]	2.718	2.085	2.88	3.36
D_o'' (cm^{-1})[a] calc.	1969	1999	2978	3034	1766	5099	1401	756.1
D_o'' (cm^{-1})[b] calc.	1767	1794	2673	2705	1585	4546	1249	674.1
% (α= 1.66 $Å^3$)[a]	66.2	64.3	72.4	66.4	65.3	124.0	111.2	111.2
% (α= 1.48 $Å^3$)[b]	59.4	57.7	65.0	59.2	58.6	110.5	99.2	99.1

Note: All group II cation-Argon complexes D_e and r_e values were used.
[a][calculated using α= 1.66 $Å^3$ ref. 58]
[b][calculated using α= 1.48 $Å^3$ this work]
[c][ref. 32] ion observed in $AuXe^+$ [60]

is not believed to be taking place in $ZrAr^+$ because of the large difference in the ionization potentials of Zr and Ar. There are currently no literature values for the prediction of the bond length of $TaAr^+$ and since our photodissociation spectrum was not rotationally resolved, this molecular ion has been omitted in the charge-induced dipole contribution calculations. More examples of transition-metal systems expected to have metal ion s-orbital occupancy in their ground states, such as $ScAr^+$ and $FeAr^+$ are currently under investigation in the Brucat laboratory and might provide additional insight into this question.

Table 5-5 summarizes the ground state bond strengths of several metal ion-Argon complexes, listed by electronic configuration of the metal ion. The trends in the binding of the various metal ions with the same ligand clearly demonstrate simple electrostatic binding. The larger the metal ion, the smaller the electrostatic and inductive binding, and thus the weaker the binding energy. Theory shows a systematic ≈20 % underestimation of all calculated $M^+\bullet Ar$ binding energies for both transition metal and non-transition metal cations complexed with argon. The observed trend of calculated ground state binding energies parallels that of experiments. However, both experimental and theoretical studies are still incomplete. Hopefully, the present work will create an incentive for calculation of second and third row containing metal cation-Argon complexes. Matching experimental data would also facilitate clarifying trends in binding energies as a function of metal ion size.

Conclusions

The bond strength of (group v) MAr^+ complexes, VAr^+ ,$NbAr^+$ and $TaAr^+$ has been determined spectroscopically as 2974 ± 10 cm^{-1} , 3106 ± 10 cm^{-1} and ≈2000 ± 500 cm^{-1}, respectively. The leading term in the electrostatic (inductive) interaction between an atomic ion and argon, the ($\mathbf{q}$-$\boldsymbol{\mu}^{IND}$) potential is found to contribute only ca. 60% of this bond energy for transition metal cations complexed with argon and ca. 100 % for group II cation-Argon systems. Given that the polarizability of argon derived here ($\alpha = 1.48$ Å^3) predicts almost 100 % of the ground state binding energy (which is overestimated by the literature $\alpha =$ 1.66 Å^3 value) for group II cation-Argon complexes a suggestion is made that the authors [22, 57, 59] use the Brucat group determined polarizability of argon for calculating the theoretical LB slope for their complexes. It is reasonable to postulate that the polarizability value (1.48 Å^3) derived from a diatomic molecular ion would better predict the binding energy of these systems compared to an exact bulk value (1.66 Å^3).

CHAPTER 6
POLARIZABILITY OF ARGON

A Measure of the Effective Electric-Dipole Polarizability of Argon

Normally, the determination of the polarizability of an atom or molecule is made from a bulk measurement of the relative electric permittivity (dielectric constant) in the radio frequency or from the index of refraction at optical frequencies. The theory behind this determination may be found in any undergraduate physical chemistry textbook [61]. In the absence of a permanent dipole, or at the high temperature limit, the reorientational contribution to the dielectric shielding of the applied electric field may be ignored and the polarizability (more precisely, the polarizability volume) of a molecule may be determined from Clausius-Mossotti equation [61] as,

$$\frac{(\epsilon/\epsilon_0) - 1}{(\epsilon/\epsilon_0) + 2} = (4\pi\rho/3)\,\alpha \qquad (6\text{-}1)$$

where (ϵ/ϵ_0) is the dielectric constant, ρ is the number density of molecules in the sample, and α is the polarizability volume of the molecule. At optical frequencies the index of refraction, n, is more easily measured than the impedance of the sample. In this case, the dielectric constant may be obtained from the relation $(\epsilon/\epsilon_0) = n^2$ and the polarizability obtained from eqn (6-1), above.

While the above treatment is not without hidden and undiscussed approximations, let us focus on the fact that a molecular property, α, is derived from a bulk phase measurement. In the bulk the molecules are in an environment created by their neighbors. The bulk electric permittivity of the sample is merely apportioned equally among the number of molecules in the sample, without regard to how the condensed phase affects individual molecular polarizability. This has the consequence of ignoring any possible many-body effects in the distortion of the molecules in the externally applied electric field.

This approximation is pragmatic in that dielectric measurements on bulk samples are easy, in contrast to the measurement of the properties of isolated molecules. The distortion of an individual atom of argon in the electric field of a nearby atomic ion is described in this chapter. The interaction of these two atoms will be studied without interference from collisions and even the application of an external electric field. The distortion of the argon is the origin of a long-ranged binding force in an ion rare-gas diatomic, and the vibrational structure of this complex determines the effective value of the polarizability in this unique environment. It is clear that the technique described here is not capable of routinely placing a measure on the polarizability of an arbitrary molecule, but is capable of determining the effective polarizability of argon to an accuracy worthy of discussion and comparison.

Sharp resonant photodissociation spectra have been observed in the Brucat group laboratory for six (transition metal cation)-(argon) binary complexes: VAr^+ [31], $NiAr^+$ [18], $CoAr^+$ [28], $NbAr^+$ [27] $ZrAr^+$ [45, 62] and $TaAr^+$ [chapter 5]. In all cases, more than one excited state of the ion has been observed. The properties of these states may vary drastically, even in a single molecule, because of differences in the electronic configuration of the metal ion which leads to that state. However, the behavior of the vibrational energy level spacing of these states near their diabatic dissociation limit , D, shows a regular structure and is the focus of our attention. For a molecular potential of the form

$$U(r) = \text{Repulsion} - \frac{C_n}{r^n} \qquad (6\text{-}2)$$

the vibrational energy level structure of the highest bound vibrational states have the property [14, 42]

$$\Delta G(v) = \frac{E(v+1) - E(v-1)}{2} = -K\,[E(v) - D]^{\left(\frac{n+2}{2n}\right)} \qquad (6\text{-}3)$$

where E(v) is the energy of the vibrational level in a given electronic state labeled by quantum number v and D is the energy of the dissociation limit of that electronic state. ΔG(v) is 'approximately' the derivative of the total energy with respect to vibrational quantum number. [E(v) - D] is the diabatic binding energy of the vibrational level labeled by v.

The constant, K, has been shown [14, 42] to be

$$K = \frac{h C_n^{-1/n}\, n\, \Gamma\left(\frac{n+1}{n}\right)}{(2\pi\mu)^{1/2}\, \Gamma\left(\frac{n+2}{2n}\right)} \qquad (6\text{-}4)$$

In this study, the long-range force binding the atoms in MAr^+ ions is expected to be charge induced-dipole (n=4) and thus

$$C_4 = \frac{q^2\alpha}{2} \qquad (6\text{-}5)$$

where q is the charge of the metal ion and α is the dipole polarizability of the argon. Application of Eqn (6-3) to MAr^+ ions suggests that for such charge-induced dipole bound species a plot of $\Delta G^{4/3}$ versus transition frequency, [E(v) - D], should be linear for the highest frequency transitions in any electronic band system, as illustrated in previous chapters 4 and 5. This analysis has been used by the Brucat group [18, 31, 63] to accurately extrapolate bound state vibrational level energies to the dissociation limit. In deference to the formulators of eqn (6-3) this plot is referred to as a LeRoy-Bernstein plot. (Note that a L-B plot of potentials with a long-ranged force characteristic of a power law with $n \neq 4$ will have a different power of ΔG on the vertical axis, but would also be called a LeRoy-Bernstein plot.) This analysis is basically an improvement of the Birge-

Sponer plot (ΔG^1 versus [E(v) - D]) which works only for molecular potentials well described by a Morse oscillator. It should be noted, however, that a traditional Birge-Sponer analysis has been successfully applied to $MgRg^+$ ions [20] which are clearly not Morse oscillators near dissociation.

LeRoy-Bernstein plots for 3 quartet electronic states of the $NiAr^+$ molecule and two excited states of $ZrAr^+$ complex have been presented elsewhere reference [18, 62] for both molecular ions respectively. Chapters 4 and 5 show L-B plots for $CoAr^+$, $CoXe^+$ and group V MAr^+ molecular ions. Although the experimental data deviates from the form of Eqn (6-3) far from dissociation, gratifying linearity is observed near E(v) = D. This confirms the origin of the long-range force between the dissociating atoms as charge induced-dipole. The limiting slope of the data near the dissociation may be obtained from eqn (3-3) for n=4 as a function of the Argon polarizability, the reduced mass of the diatomic, and fundamental constants

$$-K^{4/3} \approx \frac{-3.898}{\mu^{2/3}\,\alpha^{1/3}} \qquad (6-6)$$

where the numerical constants have been evaluated assuming $K^{4/3}$ in units of $[cm^{-1}]^{1/3}$, μ in units of g/mol, α in units of $Å^3$, and a singly charged M^+ ion.

Table 6-1 lists the corresponding limiting slopes ($-K^{4/3}$) with the reduced mass for each excited state of all six investigated molecular ions (MAr^+). The resulting polarizability of Argon from the LB limiting slopes is a function of the electron configuration of the metal cation (shown in Table 6-1 and Fig. 6-1). In general, the smaller the size of an atomic ion, then the smaller the derived polarizability value due the effect of higher multi-pole moments that are induced.

Table 6-1. Properties of the Observed Excited States of MAr$^+$ Systems.

MAr$^+$	**State label**	**M$^+$ Config. Excited State**	**D_0*(LB) [cm^{-1}]**	**m [amu]**	**$-K^{4/3}$ (Slope) [cm^{-1}]$^{1/3}$**
^{51}VAr$^+$	B	$3d^3\,4s$	16578	22.39	-0.427
^{58}NiAr$^+$	a	$3d^8\,4s$	13905	23.65	-0.415
^{58}NiAr$^+$	b	$3d^8\,4s$	13901	23.65	-0.414
^{58}NiAr$^+$	c	$3d^8\,4s$	14688	23.65	-0.413
^{59}CoAr$^+$	A	$3d^7\,4s$	13922	23.81	-0.415
^{59}CoAr$^+$	C	$3d^7\,4s$	15432	23.81	-0.416
^{59}CoAr$^+$	D	$3d^8$	17368	23.81	-0.443
^{59}CoAr$^+$	b	$3d^8$	15759	23.81	-0.443
^{90}ZrAr$^+$	d	$4d^2\,5s$	16762	27.67	-0.370
^{90}ZrAr$^+$	e	$4d\,5s^2$	16865	27.67	-0.366
^{93}NbAr$^+$	b	$4d^4$	14026	27.94	-0.374
^{93}NbAr$^+$	B	$4d^3\,5s$	13941	27.94	-0.374
^{181}TaAr$^+$	C	not assigned	16293	32.73	-0.320

In order to combine the results of all the molecules investigated the cube of Eqn (6-6) is examined:

$$-K^4\mu^2 = \frac{-1}{\alpha}\left[\frac{(128)(10^{24})N_A^2h^3}{\pi^2q^2c}\frac{\Gamma(5/4)^4}{\Gamma(3/4)^4}\right] \approx \frac{-59.217}{\alpha} \quad (6\text{-}7)$$

Eqn (6-7) gives the slope of a plot of $-K^4$ versus μ^{-2} as a function of α and fundamental constants only, where K^4 is in cm^{-1}, μ is in units of g/mol, α is in units of $Å^3$, q is in esu, h is in erg·s, c is in cm/s, and N_A is Avogadro's number (Further details on the unit analysis are provided in Appendix B). Figure 6-1 shows such a plot for the experimentally determined $-K^4$ values versus the inverse square of the reduced mass of the molecule from the determined limiting slopes in the six studied molecular ions. This plot, according to Eqn (6-7), should have a slope inversely proportional to the dipole polarizability of argon and an intercept of zero. The solid line shows a least squares fit to such a function and the dotted lines bound the estimated error to this fit. The slope determined from this graph (Eqn (6-7)) is -39.9 ± 3 which yields an effective value of $\alpha = 1.48 \pm 0.10$ $Å^3$ for the polarizability of Argon.

Discussion

The value obtained for the polarizability volume of argon in this study is 9% lower than the accepted literature value 1.662 ± 0.001 $Å^3$ for the static

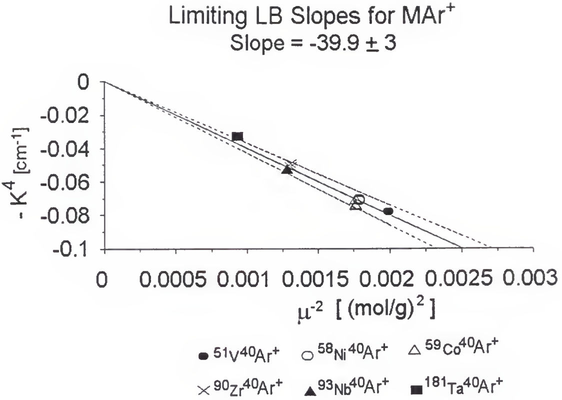

Figure 6-1. LeRoy-Bernstein Limiting Slopes for MAr$^+$ Complexes.

This is a plot for the experimentally determined $-K^4$ values versus the inverse square of the reduced mass of the molecular ion from the limiting slopes of the excited states. This plot, according to eqn (6-7), should have a slope inversely proportional to the polarizability of argon and an intercept of zero. The solid line shows a least squares fit to such a function and the dotted lines bound the estimated error to this fit. The slope determined from this graph is -39.9 ± 3 which yields a value of the dipole polarizability volume of Argon of $\alpha = 1.48 \pm 0.10$ Å^3.

polarizability volume [2, 64, 65] of this atom. This discrepancy is actually outside the estimated error limits of this study (±7%), but just barely. Is there any significance to this discrepancy?

Although the possibility of many-body effects as a cause of a deviation in the dielectric constant from a pressure-independent form (Eqn 6-1) exists, as alluded to in the introduction, the effects of pressure on the dielectric constant of the rare gases are well studied and presumably understood [66]. Careful extrapolation to low density, which is clearly possible in high sensitivity measurements, can eliminate the unwanted confusion introduced by such phenomena. The literature value of the static polarizability from ref [64] has been determined in this way and is thus taken as an intrinsic property of the isolated atom.

For atoms and molecules with absorptions, the index of refraction, dielectric constant, and polarizability are all functions of frequency. Measurements of the 'static' polarizability are not done with static electric fields, but with RF [64] or microwave [65] fields. These frequencies are much lower than any resonance frequencies in the argon atom and are thus considered to be varying so slowly in time as to be 'static'. The vibrational energy level structure near dissociation for a diatomic ion is determined by the charge induced dipole forces at the outer turning point of the potential and on a timescale of a vibrational period. Thus, our spectroscopic technique should determine the polarizability of argon at a frequency comparable to that corresponding to the diabatic dissociation energy of the ion complex, typically about 3000 cm^{-1} for the ions in this study.

The frequency dependence of the polarizability has several distinct origins. For polar species, the dielectric constant drops as the frequency of the applied electric field exceeds the reorientation time of the molecule. But, for argon, no permanent moments exist to be reoriented, so no such drop is expected to occur. The argon atom has resonant electronic absorptions in the deep UV. The Kramers relations [67] describe how the dielectric constant (and thus the molecular polarizability) is affected by this absorption. Since the characteristic frequency of the electric polarization in this experiment is well below the frequency of electronic absorption, the dielectric constant and thus the polarizability are expected to increase with increasing frequency. This is supported by the measured value [68] for the polarizability of Ar at an optical wavelength of 6328 Å (corresponding to a frequency of ~15 800 cm^{-1}) of 1.663 $Å^3$, an increase of 1.3% over the 'static' value. An effect of the characteristic frequency of the measurement then cannot be the cause for the observed 9% discrepancy.

It seems from the above discussion that neither many-body effects nor frequency dependence can explain the discrepancy between the effective polarizability of argon as measured from the spectroscopy of ion-argon complexes and bulk determinations. Yet, the spectroscopic data is consistent with the predicted trend with respect to reduced mass of the diatomic complex (Fig. 6-1) which supports the validity of the LeRoy-Bernstein analysis [14, 42].

The polarizability of argon determined in this study is found to be an 'effective' value, which will be of use in the modelling of other ion-argon complexes. But what makes it just an effective measure?

In both the optical and RF measurements of the polarizability, the applied electric field has parallel equipotential surfaces (plane wave) over the dimensions of the atom. i.e., there is no appreciable electric field gradient. In the case of the diatomic ion complex, the electric field lines of the ion radiate from its center of charge. Even at the highest investigated vibrational levels, the outer turning point of the nuclear motion of the ion complex only has an internuclear separation of about 8 Å. This means that the electric field the argon experiences within the molecule has a significant gradient over its dimensions. This asymmetry of the electric field induces higher moments in the charge distribution of the argon than would be induced by the field within an infinite parallel-plate capacitor or in either the optical or RF studies referred to above. It is possible that the induction of these higher moments will effectively reduce the polarizability in the dipole distortion, which is consistent with observation.

Summary

The vibrational structure of ion-Argon complexes has been studied by application of the formalism of LeRoy and Bernstein. The effective polarizability of argon obtained from these diatomic complex ions (1.48 ± 0.10 $Å^3$) is very similar to (1.49 ± 0.10 $Å^3$ [69]) a previosly determined value and comparable to, but smaller than, that measured by more conventional methods. This reduction in dipole polarizability within the complex may be due to the effect of the simultaneous distortion of the atom into higher multipole moments.

CHAPTER 7
PROBING THE IRON-LIGAND STRETCHING AND BENDING MODES IN $FeCO^+$ AND $FeCO_2^+$ COMPLEXES

Evidence of Spin-Allowed and Spin-Forbidden Transitions

Complexes of metal elements are found in numerous biological systems. This chapter focuses on the spectroscopy of iron-ligated complexes because of iron's importance to all living organisms. Proteins such as myoglobin, hemoglobin, cytochrome and enzymes such as peroxidase and catalase all have iron located at the center of a planar porphyrin system [70]. However, in both myoglobin and hemoglobin iron is in the +2 oxidation state; it forms four σ-bonds with nitrogen atoms in the porphyrin ring which leaves two ligands to account for the octahedral complex. The fifth ligand is provided for by the histidine group (part of protein chain) and in the absence of oxygen the sixth ligand is a water molecule. A number of ligands e.g. CO and NO are also known to bind to Fe^{2+} ion. CO binds more strongly than O_2 by $\approx$50 times in myoglobin and $\approx$ 200 times in hemoglobin [70]. The vibrational assignment of the FeCO unit of CO-bound heme proteins has been made possible by resonance Raman and infrared spectroscopies [71]. The binding energy and structural properties of these metal-ligand systems are crucial in understanding how the protein or enzyme functions, moreover, experiments and theories that provide this information are not trivial.

Thus, it is not surprising that there are a large number of experimental [15-31, 71-78] and theoretical [79-84] investigations on electronic and bonding properties of metal-ligated systems. In order to understand properties of macroscopic complexes containing transition metal it is important to break down the system to a small unit (for example, metal-ligand or binary molecule) where high-resolution spectroscopic techniques are available and experimental data can be used to test available theories. The first type of interaction discussed here will be bonding in (Fe^+-CO). The binding mechanism of Fe-CO (where iron is either neutral or charged) is not based purely on electrostatic interaction but a covalent σ-bond and π-back donation results in an appreciable double bond characteristic between the metal and carbon monoxide [78, 79, 80]. However, *ab initio* electronic structure theory finds that the binding mechanism is electrostatic in nature with no more than 10 % σ ligand-to-metal donations and practically no π-back donation in the binding of a CO ligand to early transition metal +1 ions, Sc^+, Ti^+, V^+ and Cr^+ [85].

For the second example, an electrostatic system ($Fe^+{\bullet}CO_2$) consisting primarily of a charge-quadrupole interaction is discussed. CO_2 plays a vital role in the carbon fixation cycle which forms organic molecules from reaction with H_2O. The activation of carbon dioxide may be done by photochemical (i.e. photosynthesis), electrochemical or catalytic process; fixation of CO_2 on the metal center is supposed to be a key step for the ultimate reduction of CO_2 as discussed in this review article [86].

Part A: Spin-Allowed Transition in $FeCO^+$

Figure 7-1 shows the photodissociation spectrum of $^{56}FeCO^+$ in the region 13 900 cm^{-1} to 18 100 cm^{-1}. The isotopomer of this molecular ion $^{54}FeCO^+$ was recorded simultaneously but it is not indicated in this figure. Only the $FeCO^+ \rightarrow Fe^+ + CO$ photofragmentation pathway is observed at this energy, which is the reverse process for complex formation in the molecular ion source. The labeling of transitions (tick marks above the spectrum) corresponds to the $^{56}Fe^+$-CO stretch and rock quantum numbers (ν_s, ν_r), respectively. Table 7-1 lists the assigned band origins in the $\tilde{A}-\tilde{X}$ system. They are analyzed with respect to a simple formula [87],

$$\begin{aligned} v[A(v_s,v_r)-X(0.0)] &= T_{00} + \omega_s v_s + \omega_r v_r + x_{SS} v_s^2 + x_{rr} v_r^2 \\ &\quad + x_{sr} v_s v_r + y_{ssr} v_s^2 v_r + y_{srr} v_s v_r^2 \end{aligned} \tag{7-1}$$

where T_{00} is the electronic origin, ν_s and ν_r are the stretch and rock upper state vibrational quantum numbers, respectively, ω_r and ω_s are the stretch and rock harmonic frequencies, x_{ss}, x_{rr}, x_{sr} are the first-order anharmonicity frequencies and y_{ssr} and y_{srr} are the second-order anharmonicity constants. The fit of

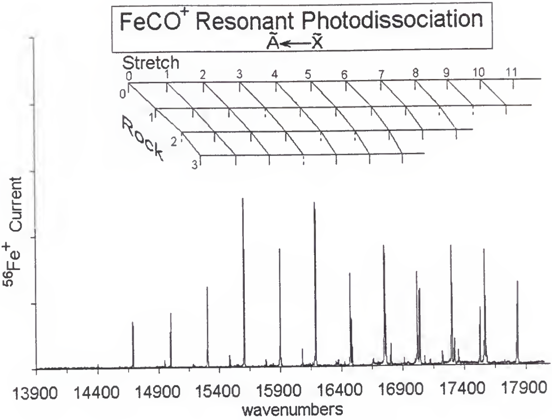

Figure 7-1. The Resonant Photodissociation Spectrum of $^{56}FeCO^+$.

The vertical axis is relative $^{56}Fe^+$ photocurrent resulting from the photofragmentation of the isolated isotopomer $^{56}FeCO^+$ and the horizontal axis is the dissociation laser frequency. The tick marks above the spectrum indicate assigned band origins and dashed lines mark grossly perturbed or missing transitions.

Table 7-1. Frequencies of Assigned Transitions in $FeCO^+$ and $FeCO_2^+$ Molecular Ions [cm^{-1}]

		$^{56}FeCO^+$		($^{56}FeCO^+$ - $^{54}FeCO^+$)		
ν'_s	ν'_r	**Observed**	**Obs.- Calc.**	**Observed**	**Calc.**	**Obs.- Calc.**
0	0	14687.6	-1.1	0	0.38	-0.38
1	0	14999.3	0.8	-1.76	-1.50	-0.26
2	0	15305.1	1.4	-3.63	-3.31	-0.31
3	0	15605.7	1.7	-4.9	-5.07	0.17
4	0	15900.5	1.0	-6.28	-6.77	0.49
5	0	16190.1	-0.2	-8.33	-8.41	0.08
6	0	16474.1	-2.2	-8.94	-9.99	1.05
7	0	16755.7	-1.8	-11.1	-11.5	0.40
8	0	17041.5	7.5	-	-13.0	-
9	0	17301.5	-4.1	-13.1	-14.4	1.30
10	0	17570.8	-1.8	-14.5	-15.7	1.20
11	0	17836.0	1.3	-16.4	-17.0	0.60
0	1	14888.9	-0.4			
1	1	15194.6	-0.3			
2	1	15493.4	-2.9			
4	1	16081.5	-5.3			
5	1	16373.8	-2.0			
6	1	16660.3	-0.4			
7	1	16945.7	4.3			
10	1	17757.9	-0.9			
1	2	15380.2	3.5			
2	2	15671.4	1.6			
3	2	15962.1	2.7			
6	2	16805.2	-1.9			

Table 7-1--continued.

		$^{56}FeCO^+$	
v'_s	v'_r	**Observed**	**Obs.- Calc.**
7	2	17082.8	0.0
8	2	17356.8	1.9
0	3	15257.2	-4.0
1	3	15547.1	3.0
2	3	15825.0	0.8
4	3	16373.8	-1.9
5	3	16647.2	0.0
6	3	16915.4	-0.5

	$^{56}FeCO_2^+$		
v'_s	v'_r	**Observed**	**Obs.- Calc.**
0	0	14538.4	2.8
1	0	14713.4	-0.5
2	0	14885.7	-1.2
3	0	15053.1	-1.3
4	0	15215.7	-1.0
5	0	15374.8	1.2
0	1	14639.3	-1.8
1	1	14817.8	-1.7
2	1	14993.7	1.3
3	1	15163.4	3.3
5	1	15478.0	-1.2

observed transitions only to the first-order anharmonicity resulted in larger residuals (observed - calculated), thus fitting of the experimental data to second-order anharmonicity became necessary. Table 7-2 shows these spectroscopic constants for ^{56}FeCO$^+$.

FeCO$^+$ molecular ion is assumed to have a linear geometry (based on theoretical prediction [79-84]) thus expected to have 3N-5 = 4 vibrational degrees of freedom. However, in the obtained spectrum only cold bands are observed with two vibrational modes active, that is the Fe$^+$ ↔CO stretch and Fe$^+$ $\triangle$CO rock or angular motion. No internal ligand stretching modes (CO stretch) are observed in this study, however, Villalta and Leopold [76] have measured the CO stretch (1950 cm^{-1}) in the ground state ($^3\Sigma^-$) of FeCO in the gas phase, even though their value is less than that of a "free" molecule, 2 150 cm^{-1} [88].

Figure 7-2 is a "close-up" of the (0,0) band origin of the $\tilde{A}$ state in the ^{56}FeCO$^+$ system. This band is red-degraded indicating a longer bond length in the excited state relative to the ground state. A simulated contour of this band is consistent with a linear geometry yielding a similar bond length to theory of 1.7 Å [76] between Fe$^+$ and center of mass of CO.

The sharp features in Fig. 7-1 represent vibronic bands in the Fe$^+$↔CO stretching mode (observed in the interval 14 500 cm^{-1} to 18 000 cm^{-1}) with up to three quanta of angular motion (relatively smaller intensities) built on each stretching mode. In Figure 7-3 the assigned bands are plotted as a function of the excited state vibrational stretching quantum number (v_s') on the horizontal axis. The tick marks above the spectrum indicate the excited state quantum numbers of the vibrational indeces of both the stretching (v_s') and rocking (v_r') modes.

Table 7-2. Molecular Constants of ^{56}FeCO$^+$ and ^{5}FeCO$_2^+$ [cm^{-1}].

Spectroscopic Constants	**^{56}FeCO$^+$ x-State**	**^{56}FeCO$^+$ Ã-State**	**^{56}FeCO$_2^+$ x-State**	**^{56}FeCO$_2^+$ ã-State**
ν_{00}	0	14688.6	0	14535.5
ω_s	-	312.3	-	181.0
ω_r	-	205.6	-	105.5
x_{ss}	-	-2.39	-	-2.68
x_{rr}	-	-4.91	-	-
x_{sr}	-	-2.32	-	-
y_{ssr}	-	0.32	-	-
y_{srr}	-	-2.33	-	-
k_s (N.m^{-1})[a]	-	107.0	-	47.6
Fe$^+$ Config.	3d^7 ($^4F_{9/2}$)	3d^7 ($^4P_{3/2}$)	3d^{6}4s ($^6D_{9/2}$)	3d^7 ($^4P_{3/2}$)
Atomic Energy[b]	1872.6	13 673.21	0	13 673.21
Diabatic limit	13 090 ± 500[d]	10 200± 500	3 920 ± 500[d]	3 050± 500
D_0* (BS)	13 090 ± 500	24 890± 500	3 910 ± 500	17 590±500

[a] Force constant of the Fe$^+$-L stretching mode.

[b] Ref. [10]

[c] Adiabatic limit Birge-Sponer approximation.

[d] Ground state binding energy, D_0", determined from [$D_0" = D_0*(BS) - \Delta E_{atomic}$]

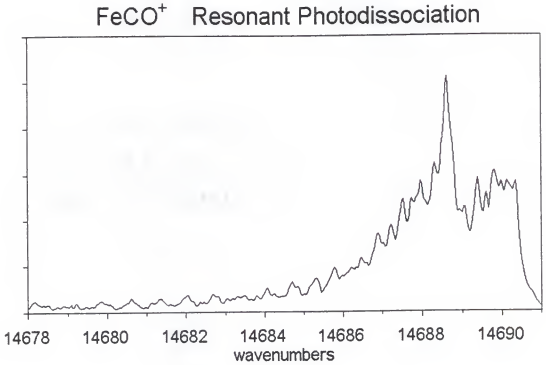

Figure 7-2. The Band Origin (0,0) of $^{56}FeCO^+$.

Higher resolution of the A←X origin (0,0) which corresponds to (ω_s,ω_r) in $^{56}FeCO^+$. The band is clearly red-degraded indicating that the excited state (A) is less bound than the ground state (X).

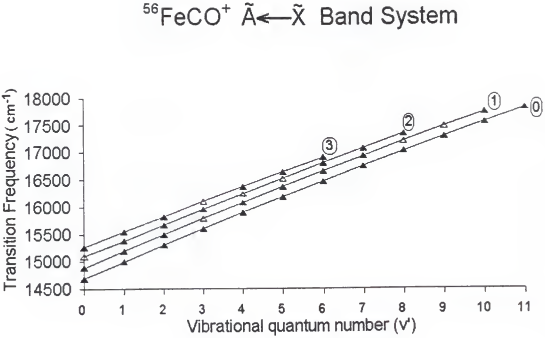

Figure 7-3. The Assigned Transitions of the A–X Progression in $^{56}FeCO^{+}$.

The symbols (triangles) are observed transitions and the curves are the least-squares fit of Eq.1 to assigned band origins. Numbers in circles indicate the rock quantum number built on the vibrations. The horizontal axis is absolute vibrational quantum number and the vertical axis is the transition frequency.

The intensity of these transitions suggests that the probed transition $\tilde{A}$ $3d^7$ (^4P) $\leftarrow 3d^7$ (^4F) $\tilde{X}$ in the $FeCO^+$ system is spin-allowed compared to the $FeCO_2^+$ photodissociation spectrum which results from a spin-forbidden transition $3d^7$ (^4P) $\tilde{a}$ $\leftarrow 3d^6$ 4s (^6D) $\tilde{X}$ [Part B]; since only a fifth of the $FeCO^+$ molecular ion (relative to $FeCO_2^+$ ion) was made in the molecular beam source. Fig. 7-3 shows the fit of observed transitions to the predicted line positions by Eq. 7-1 with $v_r = 3$ as the highest assigned rock quantum number. The residuals (observed-calculated), to this fit are listed in Table 7-1. Measured isotope shift between the molecular ions $^{56}FeCO^+$ and $^{54}FeCO^+$ are used to assign the true vibrational quantum number of the $\tilde{A}$ state.

Assuming that Fe^+-CO is a pseudo-diatomic molecular ion Eqn. 4-2 was used to predict the isotope shift ($^{56}FeCO^+$ - $^{54}FeCO^+$) which is in accord with experimental results. Assigning the first observed band of the $\tilde{A} \leftarrow \tilde{X}$ progression as the electron origin (0,0) shown in Figure 7-4 gives the best agreement.

Dissociation Energies

Very sharp transitions are observed, shown in Fig.7-1, and are believed to originate from a parity forbidden, spin-allowed transition centered on the iron cation: $3d^7$ (^4P) $\tilde{A}$ $\leftarrow 3d^7$ (^4F) $\tilde{X}$. The atomic states from which the $\tilde{A}$ and $\tilde{X}$ states originate are indicated with asterisks in Figure 7-5. However, this transition does not originate from an excited state as maybe suggested by Fig. 7-5. The promotion energy of 1872.6 cm^{-1} [9] from a ^6D ($3d^6$ 4s) to ^4F ($3d^7$) in the atomic ion is smaller than the gain in the stability of the molecular ion formed from a $3d^7$ configuration: however, it is possible for $FeCO^+$ to bond from ^6D ($3d^6$ 4s) ground state, shown in Figure 7-6. For this configuration, the occupied 4s orbital will yield a larger Fe^+-CO repulsion than in the state derived from a $3d^7$ configuration and the π-back bonding will be weaker for the state with an occupied s-orbital as there are only three $3d\pi$ electrons for donation to the CO π^* orbital. $FeAr^+$ and FeH_2O^+ have ground states derived from ^6D ($3d^6$ 4s) asymptote of Fe^+ since Ar and H_2O have smaller repulsion with Fe^+ ion compared with CO [89]. The ground state term symbol ($^4\Sigma^-$) for $FeCO^+$, predicted by theory [78,79], is derived from a $3d^7$ (^4F) atomic configuration.

The derived binding energy (D_0') of the $\tilde{A}$ state is 10 200 cm^{-1} from a Birge-Sponer approximation, ($D_0' \approx \omega_{ss}^2/4x_{ss}$) which normally yields a lower limit to the true binding energy of the studied molecular ions. The summation of D_0' to the electronic origin, ν_{00} , yields a Birge-Sponer dissociation limit [D_0^* (BS)] of the $\tilde{A}$ state shown in Table 7-2. The only possible spin allowed transition in the investigated region, 13 900 cm^{-1} to 18 100 cm^{-1}, is $3d^7$ (^4P) $\tilde{A} \leftarrow 3d^7$ (^4F) $\tilde{X}$ which has been assigned for the observed progression, see Figure 7-5. There are three possible choices of atomic lines for the ^4P manifold, however, experimental data obtained here does not provide adequate information for determining the exact ^4P manifold from which the $\tilde{A}$ state originates, thus the middle is picked as a reasonable guess which introduces an error in the determined binding energy

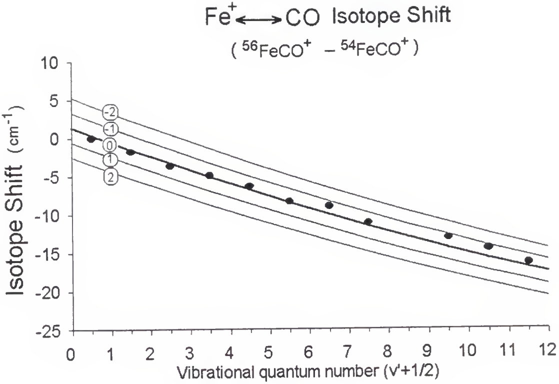

Figure 7-4. Observed and Calculated Isotope Shift of FeCO$^+$.

A fit of observed isotope shift (^{56}FeCO$^+$ - ^{54}FeCO$^+$) to Eq.4-2. Symbols represent experimental data points and curves are calculated. The vibrational quantum numbers (v') in circles are the predicted assignments for the lowest observed band. The agreement (thick solid curve) indicates that the first assigned band is the electronic origin, (0,0).

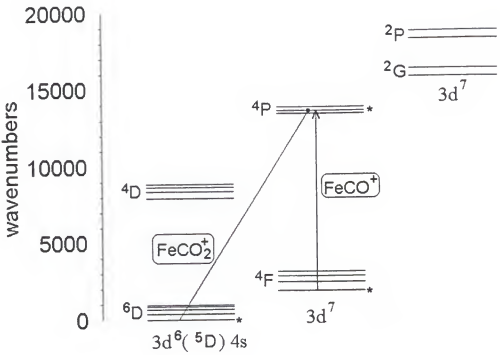

Figure 7-5. The Low-Lying Atomic States of Fe$^+$ [9].

Asterisks indicate atomic states from which the probed states originate. The observed transition for the Â−$\bar{X}$ system of FeCO$^+$ originate from a parity-forbidden spin-allowed excitation centered on iron cation: 3d^7 (^{4}P) Â ← 3d^7 (^{4}F) $\bar{X}$. For the FeCO$_2$$^+$ system the observed transition arises from a spin-forbidden excitation, 3d^7 (^{4}P) â ← 3d^6 4s (^{6}D) $\bar{X}$.

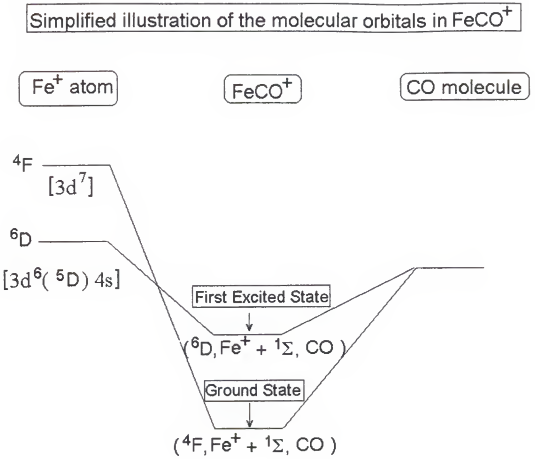

Figure 7-6. Simplified Molecular Orbital in $FeCO^+$.

The figure shows the 'stability' gained by the $FeCO^+$ molecular ion, corresponding to a $3d^7$ electron configuration in the Fe^+ ion to be better than that from a molecular ion ($FeCO^+$) originating from a $3d^6 4s$ configuration. Thus the , $\tilde{A} \leftarrow \tilde{X}$, transition probed in $FeCO^+$ is believed to originate from a ^4F manifold centered on the Fe^+ atomic ion.

of ± 250 cm^{-1}. This error combined with that arising from a Birge-Sponer approximation ≈250 cm^{-1} yields binding energy values with an uncertainty of ± 500 cm^{-1} as indicated in Table 7-2.

The binding energy of the ground state is then determined from the difference of the dissociation limit and the atomic promotion energy at the diabatic limit. This promotion energy is the difference between ^4P and ^4F atomic lines or 11 800.6 cm^{-1} [9]. Thus the ground state adiabatic binding energy of $FeCO^+$ is, $D_0'' = [(\nu_{00} + D_0') - \Delta E_{atomic}]$ or $[(14\,688.6\ cm^{-1} + 10\,200\ cm^{-1}) - 11\,800.6\ cm^{-1}] = 13\,088 \pm 500\ cm^{-1}$.

Trends in $FeCO^+$, $FeCO^-$ and FeCO Binding Energies

The dissociation energies, D_0'' and D_0', of $FeCO^+$, $FeCO^-$ and FeCO determined both from experiment and theory are presented in Table 7-3. Experiment and theory agree that, $FeCO^+ > FeCO^- > FeCO$, however, the error in the absolute value of the calculated binding energy compared to the measured one varies. In all three systems the σ-donation and π-back bonding charge transfer bonding mechanism is operative, illustrated in Fig. 7-7 for $FeCO^+$ [78].

$FeCO^+$ is the most bound because of additional electrostatic forces, charge (Fe^+)-dipole (CO) and charge-quadrupole interactions {calculated in Part B}. It is interesting to note that the calculation by Ricca et al. [82] yields lower binding energy values for FeCO and $FeCO^+$ relative to experimental results, Table 7-3. The calculated percentage error for $FeCO^+$ complex [(observed -

Table 7-3. Spectroscopic Properties of Iron-Carbonyl Systems [cm^{-1}]

Ground State [Ref #]	**$^{56}FeCO$ [72, 76]**	**$^{56}FeCO^-$ [73, 76]**	**$^{56}FeCO^+$ [this work]**
Iron Config.	$3d^7 4s$, $^3F_4$	$3d^7 4s^2$, $^4F_{9/2}$	$3d^7$, $^4F_{9/2}$
Atomic Energy	11 976.26	Fe^- ?	1872.60
Term Symbol	$\tilde{X}\ ^3\Sigma^-$	$\tilde{X}\ ^4\Sigma^-$	$\tilde{X}\ ^4\Sigma^-$
BDE (Expt)	8 290 ± 2 450	11 790 ± 1 250	13 090 ± 500
BDE (DFT)[a]	(4 652)	-	(10 840)
BDE (NL-Sph)[b]	(14 340)	(16 438)	(20 635)
Iron↔CO (Expt)	530 ± 10	465 ± 10	-
Iron↔CO (DFT)[a]	(455)	-	(423)
Iron↔CO (NL)[b]	(658)	(566)	-
Iron↔CO (LSDA)[b]	(672)	(555)	(547)
Iron△CO (Expt)	330 ± 50	230 ± 40	-
Iron△CO (DFT)[a]	(316)	-	(319)
Iron△CO (NL)[b]	(368)	(272)	-

Excited State [Ref.#]	**$^{56}FeCO$ [76]**	**$^{56}FeCO^-$ [no data]**	**$^{56}FeCO^+$ [this work]**
Iron Config.	$3d^7 4s$, $^5F_5$	-	$3d^7$, $^4P_{3/2}$
Atomic Energy	6928.28	-	13 623.21
Term Symbol	$\hat{a}\ ^5\Sigma^-$	-	-
BDE	(3 777)	-	10 200 + 500
ν_{00}	1 135 ± 25	-	14 688.6
Iron↔CO	(410) 460 ± 15	-	312.3
Iron△CO	(61) 180 ± 60	-	205

All values in parenthesis are theoretical predictions. [a]Ref. [80] [b]Ref. [78]

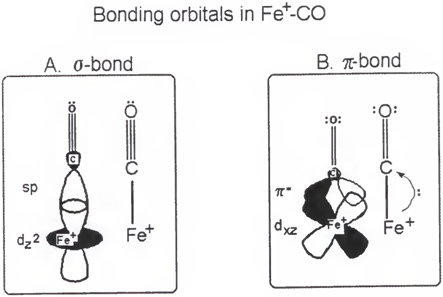

Figure 7-7. Schematic representation of the bonding orbitals in $FeCO^+$.

Panel A shows the formation of a σ-bond between CO and Fe^+. The carbon atom in CO is sp-hybridized. One of the hybrid orbitals containing the lone-pair electrons overlaps with the d_z^2 orbital of iron to form a σ-bond. Panel B indicates the formation of a π-bond. Back donation of electron density from the d_{xz} orbital of Fe^+ to an empty π* orbital on CO.

calculated) / observed] ≈ 17.2 % is in accord with previous observations of various metal cation-rare gas complexes [chapters 4 and 5]. However, for FeCO a much larger calculated error is found ≈ 44 % this could also be attributed to the much higher uncertainty (± 30%) in the measured experimental value [72] whereas ≈ 4 % experimental error is indicated for FeCO$^+$, Table 7-3. The adiabatic energy of FeCO$^+$ (13 090 ± 500 cm^{-1}) determined via high resolution photodissociation spectroscopy is in good agreement with that measured using collision-induced dissociation (12 820 ± 650 cm^{-1} [75]).

For FeCO complex, the ground state originating from a ^{5}D (3d^6 4s^2) on the atom is repulsive. Theory [78, 82] and experiment [76] agree that the ground state term symbol for FeCO is $^3\Sigma^-$ with $^5\Sigma^-$ being the first excited state. Despite the larger promotion energy of 11 976 cm^{-1} [10] for ^{3}F (3d^{7}4s) ← ^{5}D (3d^6 4s^2) excitation compared to only 6 928 cm^{-1}[10] ^{5}F (3d^7 4s) ← ^{5}D (3d^6 4s^2) the gain in the stabilization of the molecule derived from a (^{3}F) 3d^7 4s atomic asymptote compensates best for the cost of the excitation energy. The study of FeCO and FeCO$^-$ via negative ion spectroscopy yield $^3\Sigma^-$ for FeCO and for $^4\Sigma^-$ FeCO$^-$ ground states and $^5\Sigma^-$ as the first FeCO complex excited state, 1 135 ± 25 cm^{-1} higher in energy relative to the $^3\Sigma^-$ state [76]. From theoretical predictions different models favor the assignment of $^3\Sigma^-$ as the ground state [78, 80].

Since the lowest state of FeCO complex has an occupied 4s orbital (Fe, 3d^{7}4s) which increases the repulsions along the bonding axis it is less bound compared to that of FeCO$^+$ with no 4s-orbital occupation (Fe$^+$, 3d^7). The fully promoted (Fe $3d^8$) states are at least 4 eV [9] higher in energy than the ground state (Fe $3d^7$ 4s), thus for FeCO molecular ion promoting an s electron to a d-orbital will not be energetically favorable.

The binding energy of $FeCO^-$ (11 790 cm^{-1} [73])is intermediate to $FeCO^+$ and FeCO because: a) the $FeCO^+$ molecular ion is the most bound as a result of additional electrostatic forces; b) FeCO in the ground state pays a high cost for the promotion energy ≈1.5 eV [9] from (Fe $3d^6$ $4s^2$) to (Fe $3d^7$ 4s) electron configuration. All three molecular ions $FeCO^+$, $FeCO^-$ and FeCO have σ-bond and π-back bonding present, however, the trend for the M-CO π-back bonding character is $FeCO^- > FeCO > FeCO^+$. Despite the $3d^7 4s^2$ electron configuration in the ground state of $FeCO^-$ this molecular ion is strongly bound because of the ease with which the Fe^- can donate its 3d electron density to the empty antibonding $\pi*$ orbital in CO. This effect produces a stronger M-CO π- back bond in the anion which can offset its extra σ-repulsion [78]. Fe^+ ion in $FeCO^+$ has the least π-back bonding character because of the high energetic cost of donating electron density from Fe^+ due to its high second ionization potential 16.18 eV [1]. The 3d electron detachment of Fe^- (0.151 eV) [78] compared to that of ^3F and ^5F of Fe (7.40 eV and 7.04 eV) [9] favor a stronger p-back bond formation for $FeCO^-$ ion.

Part B: Spin-Forbidden Transition in $FeCO_2^+$

Figure 7-8 shows the photodissociation spectrum of $^{56}FeCO_2^+$ in the region 14 000 cm^{-1} to 16 200 cm^{-1}. Only the $FeCO_2^+ \rightarrow Fe^+ + CO_2$ photofragmentation pathway is observed at this energy, which is the reverse process for complex formation in the molecular ion source. The second possible pathway $FeCO_2^+ \rightarrow FeO^+ + CO$ was not observed in the probed region. Similar data analysis discussed in Part A were performed for the $FeCO_2^+$ system and line positions of assigned band origins are listed in Table 7-1. Molecular spectroscopic constants are provided for in Table 7-2.

Comparison of $FeCO_2^+$ to $FeCO^+$ Photodissociation Spectra

The observed peaks in the $FeCO_2^+$ system, Figure 7-7 are weak indicative of a spin-forbidden transition $\{3d^7\,(^4P)\ \tilde{a} \leftarrow 3d^6\,4s\,(^6D)\ \tilde{X}\}$ whereas the $FeCO^+$ bands, Figure 7-1 are much more intense characteristic of a spin-allowed transition $\{3d^7\,(^4P)\ \tilde{A} \leftarrow 3d^7\,(^4F)\ \tilde{X}\}$. The possibility of probing the same or analogous transition in both molecular ions is ruled out given that the synthesized $FeCO_2^+$ molecular ion in the plasma source was five times that of $FeCO^+$, yet the $FeCO_2^+$ photodissociation spectrum exhibited much less signal, Fe^+ photocurrent. Up to twelve excited vibrational stretching frequencies were observed in the $FeCO^+$ system whereas only six bands in $FeCO_2^+$. The assignment in the quantum number of rock (or angular motion of the ligand with respect to the metal cation) was only up to the first quantum built on a stretching mode for $FeCO_2^+$ compared to up to three quanta of rock in the $FeCO^+$ ion.

Binding Energies

The binding energy of $FeCO_2^+$ is determined in a very similar manner as that of $FeCO^+$. The excited state diabatic limit, D_0', is simply estimated from Birge-Sponer approximation ($D_0' \approx \omega_{ss}^2/4x_{ss}$) as 3 050 ± 500 cm^{-1} whereas the ground state binding energy, D_0'', is determined from the difference between the dissociation limit of the $\tilde{a}$ state derived from Birge-Sponer approximation, $D_0^*(BS)$ or $(\nu_{00} + D_0')$ and the atomic energy separation, ΔE_{Atomic} : $[(\nu_{00} + D_0') - \Delta E_{Atomic}] = [(14\ 535.5\ cm^{-1} - 13\ 673.21\ cm^{-1}) - 13\ 672.21\ cm^{-1}] = 3\ 920 \pm 500\ cm^{-1}$. These binding energy values are expected to yield a lower limit to the true binding energy [as discussed in Chapters 4 and 5 for $M^+\bullet(Rg)$ complexes] because of an improper asymptotic behavior of the Morse potential applied to a transition metal cation-ligand binary ion. Thus the reported adiabatic binding energy of 2 800 cm^{-1} [90] for $FeCO_2^+$ is unexpectedly much too small.

Trends in M^+-CO_2 Binding Energies

Molecular constants for six metal cation systems complexed with carbon dioxide are given in Table 7-4. For group II systems the expected trend in the ground state binding energies is observed with $Ca^+\bullet CO_2$ [91] being less bound than $Mg^+\bullet CO_2$ [92] because of increased radial size of the metal atomic ion, 4s versus 3s occupation. However, the binding energy of 669 cm^{-1} for $Ca^+\bullet CO_2$ is extremely low, Scurlock et al. [91] indicate that further investigations in this

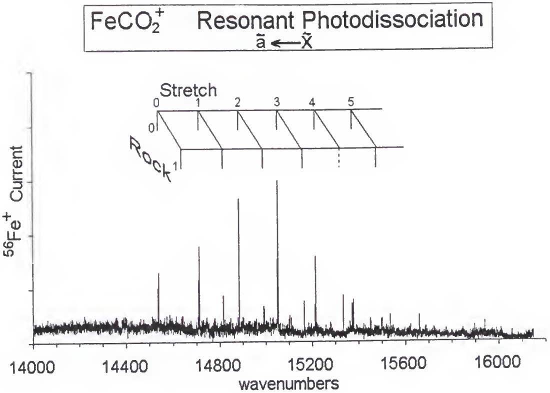

Figure 7-8. ^{56}FeCO$_2^+$ Photodissociation Spectrum.

Tick marks above the spectrum indicate assigned transitions with the dashed line showing a perturbed band. The horizontal axis is the dissociation laser frequency and the vertical axis is relative ^{56}Fe$^+$ photocurrent resulting from the photofragmentation of the mass-selected molecular ion, ^{56}FeCO$_2^+$.

surprising result are needed. However, the trends and absolute values of the stretching frequencies determined for these molecular ions are reasonable with ≈380 cm^{-1} for $Mg^{+}\text{--}CO_2$ and ≈250 cm^{-1} $Ca^{+}\text{--}CO_2$.

The observed trends in the ground state binding energy of transition metal containing systems are increasing in the series: $Fe^{+}\bullet CO_2$ [this work] < $V^{+}\bullet CO_2$ [93] < $Co^{+}\bullet CO_2$ [17] < $Ni^{+}\bullet CO_2$ [94]. The electron configuration of the metal ion in the complex determines its radial size which is inversely proportional to the binding energy. The $V^{+}\bullet CO_2$, $Co^{+}\bullet CO_2$ and $Ni^{+}\bullet CO_2$ complexes have no occupied s-orbital occupation in the M^{+} configuration thus higher binding energies than $Fe^{+}\bullet CO_2$ molecular ion with $3d^6$ 4s occupation are observed. The d-orbital contraction increases as a function of the atomic number of the metal ion and this correlates with the binding energy, that is, $Ni^{+}\bullet CO_2$ with d^9 occupation in its ground state is more bound than $Co^{+}\bullet CO_2$ with d^8 occupation and $V^{+}\bullet CO_2$ with a d^4 electron configuration on the metal cation is least bound. The observed trend can be explained by the fact that it is easier for the CO_2 ligand to get closer to a M^{+} ion with d^n occupation relative to $d^n s$ occupation because of favorable radial distance.

The stretching frequencies in $V^{+}\bullet CO_2$ [95], $Fe^{+}\bullet CO_2$ [this work] and $Co^{+}\bullet CO_2$ [17] are quite similar 196 cm^{-1}, 181 cm^{-1} and 188 cm^{-1} , respectively. The photodissociation spectrum of $Ni^{+}\bullet CO_2$ appeared too congested thus could not be analyzed for vibrational information. However, the rocking frequencies of

Table 7-4. Spectroscopic constants of M^+-CO_2 systems (cm^{-1})

System [Ref.#]	[X] M^+ Config.	D_o''	Excited State	D_o'	ν_{00}	$M^+ \leftrightarrow CO_2$	$M^+ \triangle CO_2$
$^{24}Mg^+$-CO_2 [93]	$3s^1$	5154	$^2\Pi_{1/2}$ $^2\Pi_{3/2}$	11 198	29 625 29 681	381.8 385.1	- -
$^{40}Ca^+$-CO_2 [92]	$4s^1$	(669)*	$^2\Pi_{1/2}$ $^2\Pi_{3/2}$	3 830 4 076	22 031 22 168	258.9 254.2	- -
$^{51}V^+$-CO_2 [91,95]	$3d^4$	-	B ($^5P_2$ V^+ limit)	-	15 800	196.0	105.0
$^{56}Fe^+$-CO_2 [this work]	$3d^6$ $4s^1$	3800 ± 500	a (^4P Fe^+ limit)	2 966 ± 500	14 535	181.0	105.5
$^{59}Co^+$-CO_2 [17]	$3d^8$	6960	A' ($^3F_4$ Co^+ limit)	4302	12 375	188.0	65.0
$^{58}Ni^+$-CO_2 [94]	$3d^9$	8700 ± 100	a ($^4F_{9/2}$ Ni^+ limit)	-	-	-	-

*Scurlock et al. questionable results (BS analysis of data) [92]

$V^+\bullet CO_2$ and $Fe^+\bullet CO_2$ are both 105 cm^{-1}, much greater than the 65 cm^{-1} found in $Co^+\bullet CO_2$. This difference may be explained by geometry arguments that both $V^+\bullet CO_2$ and $Fe^+\bullet CO_2$ molecular ions have a non-linear structures since experiment has indicated a linear geometry for the ground state of $Co^+\bullet CO_2$.

Electrostatic Bonding of CO_2 and CO to a Transition Metal Cation

The binding energy of various neutral ligands to a transition metal cation (TM^+) have been measured via high resolution photodissociation spectroscopy. It is important to determine how closely the models predict experimental observations. For transition metal cations complexed with rare gas the primary attractive force is charge-induced-dipole and has been shown to account for ≈60 % of the overall binding energy (Chapters 5 and 6). When dealing with a ligand with a dipole or quadrupole moment then the equations that represent the intermolecular interactions can be applied to the system to predict a binding energy value. All these electrostatic energy contribution calculations require knowledge of the bond distance between a point charge (TM^+) and the ligand which are not always available from experiment, however, theoretical predictions of the bond length can be used as best estimates.

Assuming a linear geometry (see Part A) for $FeCO^+$ then the significant interaction energy between Fe^+ and CO along the internuclear axis, is charge-dipole, given by [12]:

$$V = \frac{-\mu_1 q_2}{r^2} Cos\theta \qquad (7-2)$$

where μ_1 is the dipole moment of CO (0.112 D [96]), q_2 is +1 point charge on Fe^+ or 4.8024×10^{-10} esu and r is the internuclear distance between the center of mass of CO and Fe^+ ion (1.7 Å [79]). Using the given values the calculated charge dipole contribution for Fe^+-CO is only 940 cm^{-1}. In addition, charge-quadrupole contributions are also present and can be calculated using the following formula [12]:

$$V = \frac{\Theta_1 q_2}{4r^3}(3\cos^2\theta - 1) \qquad (7\text{-}3)$$

where Θ_1 is the quadrupole moment of CO (-2.5×10^{-26} esu.cm^2 [96]), q_2 is again the +1 charge on the metal and r the internuclear separation as in Equation 7-2. Evaluating Equation 7-3 yields 6 146 cm^{-1} for the charge-quadrupole contribution, which when combined with 940 cm^{-1} (charge-dipole contribution) accounts for approximately half the experimental value of 13 090 ± 500 cm^{-1} for $FeCO^+$. The balance is believed to be attributed to the formation of both the σ- and π-bonds. Theoretical predictions by Ricca et al. [82] underestimate the binding energy of $FeCO^+$ (10 840 cm^{-1}) by ≈17 %.

Since the data presented here seem to favor a non-linear geometry for the $FeCO_2^+$ molecular ion, similar calculations as done above for $FeCO^+$ would be more involved since the angle and bond length need to be known and has not yet been calculated or measured. However, the charge-dipole contribution is trivial (zero) since CO_2 has no dipole moment. If a linear geometry is assumed then the charge-quadrupole attraction force contributes 6 320 cm^{-1} when a bond length of 2.018 Å [97] and a quadrupole moment of -4.3×10^{-26} esu. cm^2 [96] for CO_2 are used. This value overestimates the true binding energy by almost a factor of two. This large error could be due to a number of uncertainties a) incorrect predicted bond length b) unknown geometry and c) error in the measured value since the presented value yields a lower limit.

Table 7-5 shows an improvement in theory. Comparisons between calculated and experiment values show good agreement to within 10 % with the exception of $FeCO_2^+$ since Fe^+ by its nature [9] is a harder transition metal to model.

Table 7-5. Ground State Binding Energies, D_0" (kcal/mol)

System (Term Symbol)[b]	Config.[a]	D_0" (Expt)	D_0" (Calc)[b]	% Error in Calc. #
VCO_2^+ ($^5\Sigma^+$)	$3d^4$	17.3[c]	18.2	-5.2
$FeCO_2^+$ ($^6\Delta$)	$3d^64s^1$	11.2	16.1	-44
$CoCO_2^+$ ($^3\Delta$)	$3d^8$	19.9	21.3	-7.0
$NiCO_2^+$ ($^2\Sigma$)	$3d^9$	24.9	24.2	2.8

Calculated % error = (observed - calculated) / (observed)*100

[a] Metal cation atomic configuration in separated atom limit.

[b] [97]

[c] [91]

Data presented in this chapter has provided information for distinguishing between a parity-forbidden spin-allowed transition ($FeCO^+$, Part A) and a spin-forbidden transition ($FeCO_2^+$, Part B). Comparisons between similar systems provided trends that were supported by both experiment and theory, even though, the absolute values are still not identical.

CHAPTER 8
TWO-COLOR EXPERIMENTS

One of the ways that transition metals have found economic importance is in their ability to act as catalysts. The nature of this important and varied catalytic activity is not fundamentally understood. However, it is not unreasonable to speculate that the transition metal chemistry is dependent on low-lying excited electronic states of irregular features of the catalytic surface. The complexity and inhomogeneity of real catalytic surfaces have made direct high resolution studies difficult. One possible solution to this problem has been to cut down the size of the system. We have chosen to study the bonding between pairs of transition metal atoms, isolated in the gas phase and possessing an overall positive charge. The purpose of this chapter is to disseminate recent results of ongoing high-resolution optical studies of the nickel dimer cation, whose structure and spectroscopy has been of interest to the Brucat laboratory for some time.

The bonding that takes place in a transition metal dimer is not trivial because of the high angular momentum and great number of low-lying atomic states of the open d-shell atoms from which they are composed. The spectroscopy of neutral dimer molecules [98] demonstrates this feature. Neutral dimer systems have been addressed both theoretically and experimentally, and the wealth of data for these species is much greater than that of ionic systems. The comparison of the electronic structure of different charge states of these molecules is one of the goals of this research.

The bond dissociation energy of transition metal diatomics is one of the first properties to become quantified experimentally to useful precision. Comparisons of neutral and cation bond strength show interesting behavior. For instance, the bond strength of Cu_2 (2.03 eV, [99]) is greater than that of Cu_2^+ (1.84 eV, [100]) which is indicative of the exclusively sσ type bonding in these species. Another late transition metal homonuclear diatomic shows the opposite behavior, however, the bond strength of Ni_2 (and 2.04 eV, [101]) is less than that of Ni_2^+ (2.32 eV, [102]).

Ligand field theory has been applied to the manifold of low-lying electronic states of Ni_2 and NiCu [103] and shows good agreement with both *ab initio* quantum theory [104-5] and experiment [101]. Hopefully, enough data pertaining to the low-lying electronic states of dimer cation systems will be generated so that a similar ligand field approach may be tested for these species.

In this chapter two examples of diatomic ions (i.e. Ni_2^+ and $CrFe^+$) will be discussed. In part A, the vibrational assignment of five excited electronic states of Ni_2^+ and their spectroscopic constants are presented. In addition, a refined estimation of the ground state vibrational frequency, ω_e'', as 270 $\pm$ 25 cm^{-1} is also presented. In Part B, an example of a heteronuclear diatomic ion, $CrFe^+$, is discussed. The binding energy determined via two-color experiment is presented. Two pathways for the photofragmentation of $CrFe^+$ are observed and discussed.

Two-Color Experiment Technique

Details of experimental procedures have been presented before [chapter 2, 106]. Briefly, a Ni rod is laser ablated inside a high pressure flow of helium gas. Collisional cooling in the resulting plasma during a supersonic expansion of this flow initiates the formation of various cluster ions and neutrals in the resulting molecular beam. The adiabatic expansion ensures significant vibrational and rotational cooling of the molecular ions. Spectroscopic results indicate a strict upper bound for the vibrational temperature of the nickel dimer cations at 60K and an upper limit for the rotational temperatures of around 5K [107]. The ion beam is studied inside a customized tandem TOF mass spectrometer. The positive ion ensemble entering the TOF tube is accelerated to a kinetic energy of 1450 eV. During the flight down the 2.45 m tube, the ions encounter focusing and deflecting optics, ensuring a maximum ion transmission through the apparatus. Electrostatic energy dispersion of the ions following photoexcitation allows for the determination of the fragmentation yield of any given parent ion, in this case the isotopes of Ni_2^+. The optical spectra of the mass selected isotopomers are obtained simultaneously (but separately). Photoexcitation is accomplished with the visible light of two Nd^{3+}:YAG pumped dye-lasers. The first laser pulse of lower power ≈5 mJ/cm^2 (excitation) serves to prepare an excited vibronic level of the molecule. The dissociation of the photoexcited ion is accomplished by a second laser pulse of higher energy and fixed frequency. For this study a frequency non-resonant with the parent ion of $\tilde{\nu} \approx 16290$ cm^{-1} was chosen with a pulse energy of 23 mJ/cm^2. A time delay between the excitation and dissociation pulse of 300 ns was employed. This delay time is shorter than the 5-10 μs lifetime of the excited state ions [107]. Similar experimental procedures where conducted for $CrFe^+$ molecular ion.

Part A: Homonuclear Diatomic Ion

Figure 8-1 shows a portion of the resonant two-color photodissociation spectrum for the $^{58}Ni_2^+$ molecule. The vertical axis is photocurrent resulting from dissociation of the molecular ion and the horizontal axis gives the resonant laser frequency. The tick marks above the spectrum show the transitions to vibrational levels within the excited electronic state. In the region between 11,000 cm^{-1} and 18200 cm^{-1}, 5 electronic band systems have been identified and over 80 vibrational assignments made. Sharp transitions bluer than the adiabatic binding limit of the molecule (18,900 cm^{-1} [102]) have also been observed, however, the density of states and the complexity of the one photon spectrum have rendered this portion difficult to analyze (and thus will not be

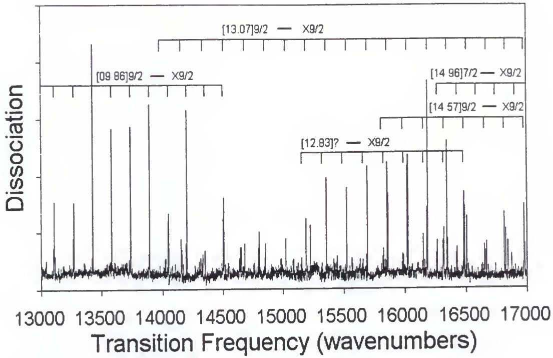

$^{58}Ni_2^+$ Resonant Two-Color Photodissociation Spectrum

Figure 8-1. Two-Color Resonant Photodissociation Spectrum of $^{58}Ni_2^+$.

A portion of the $^{58}Ni_2^+$ resonant two-color photodissociation (R2CD) spectrum in the region 13000 to 17000 cm^{-1}. The $^{58}Ni^+$ photocurrent resulting from the R2CD of $^{58}Ni_2^+$ -> $^{58}Ni^+$ + ^{58}Ni is shown as a function of resonant laser frequency. Labeled in the figure are the five electronic band systems; The vibrational numbering of the upper electronic state in the transition is indicated with vertical tick marks. All transitions originate from the vibronic ground state vibrationless ground state of the molecule thereby further facilitating the spectral analysis (there are no hot bands observed).

reported here). The ability to mass select and simultaneously monitor the isotopically varied constituents of Ni_2^+ has allowed the vibrational assignment of the spectrum shown in Fig.8-1. Due to the extensive cooling suffered by the ions prior to spectroscopic probing, each assigned transition originates from the vibrationless level of the ground state.

Table 8-1 lists line positions, vibrational quantum numbering and isotope shifts of the assigned $^{58}Ni_2^+$ photodissociation excitation transitions (grouped by electronic state). The excited state nomenclature is in accord with that used by other spectroscopists [101]. Specifically, the bracketed quantity gives the vibrational origin of the band system in thousands of wavenumbers and the number following is the total angular momentum of the molecule in that state, Ω. All the excited states with an omega assignment have been rotationally analyzed [107] and a question mark is used where rotational analysis was not achieved.

Our experimental procedure allows for the simultaneous acquisition of the photodissociation spectra of the $^{58}Ni_2^+$, $^{58}Ni\,^{60}Ni^+$, and ($^{58}Ni\,^{62}Ni^+$ + $^{60}Ni\,^{60}Ni^+$) isotopic variants of the nickel dimer cation. The spectral shifts among these isotopes is an unambiguous function of the vibrational constants and the absolute vibrational quantum numbering [41]. A subset of these data is provided in Table 8-1 (and Figure 8-2) as justification of the vibrational assignment of the observed vibronic transitions. Figure 8-2 shows the isotope shift between $^{58}Ni_2^+$ and $^{58}Ni^{60}Ni^+$ transitions in the [13.07]9/2 state as a function of vibrational quantum number ($v' + \frac{1}{2}$). The symbols and solid curves are the observed and

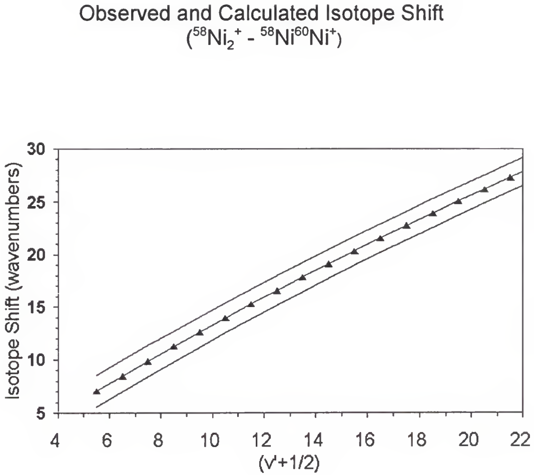

Figure 8-2. Excited State, [13.07]9/2, Vibrational Quantum Number Assignment.

The observed (symbols) and calculated (solid curves) isotope shifts for the band positions of $^{58}Ni_2^+$ minus $^{58}Ni_2{}^{60}Ni_2^+$ as a function of vibrational quantum numbering for corresponding transitions. Excellent agreement can be seen between the central calculated solid curve and the observed shifts (triangles). The remaining solid curves are calculated assuming the upper state vibrational quantum numbering is different by ± 1 quantum.

Table 8-1. Frequencies of Assigned Transitions in $^{58}Ni_2^+$ and Observed Isotope Shifts [cm^{-1}]

Transition	$^{58}Ni_2^+$ Line Positions			$^{58\text{-}58}Ni_2^+$ - $^{58\text{-}60}Ni_2^+$	
	v'-v"	Frequency	Obs-	Iso-Shift	Obs-
[09.86] 9/2 - X 9/2	7-0	11106.7	0.32	9.87	0.10
	8-0	11279.8	0.25	11.15	0.01
	9-0	11451.6	-0.02	12.46	-0.04
	10-0	11622.2	-0.36	13.74	-0.09
	11-0	11792.3	-0.02	15.16	0.02
	12-0	11960.8	-0.10	16.39	-0.05
	13-0	12128.5	0.19	17.8	0.09
	14-0	12294.5	-0.11	18.89	-0.08
	15-0	12459.2	-0.46	20.03	-0.17
	16-0	12623.2	-0.48	21.76	0.34
	17-0 *	12785.8	-0.63	21.62	-1.00
	18-0 *	12947.7	-0.40	22.98	-0.82
	19-0 *	13109.3	0.73	26.27	1.31
	20-0 *	13268.2	0.22	26.66	0.56
	21-0	13426.3	0.16	27.73	0.51
	22-0	13583.2	0.06	28.12	-0.20
	23-0	13739.6	0.51	29.69	0.29
	24-0	13894.1	0.32	30.73	0.26
	25-0	14047.7	0.39	31.12	-0.39
	26-0	14200.1	0.41	32.54	0.00
	27-0	14350.8	-0.21	33.39	-0.15
	28-0	14500.2	-0.88	34.65	0.12
[12.83] ? - X 9/2	13-0	15153.5	0.34	17.95	-0.18
	14-0	15322.8	-0.30	18.96	-0.45
	15-0	15491.4	-0.46		
	16-0	15659.6	0.28	21.84	-0.05
	17-0	15825.6	0.14	23.09	-0.01
	18-0	15990.3	-0.13	24.74	0.45

Table 8-1--continued.

Transition	$^{58}Ni_2^+$ Line Positions			$^{58-58}Ni_2^+$ - $^{58-60}Ni_2^+$	
	v'-v"	Frequency	Obs-	Iso-Shift	Obs-
[12.83] ? - X 9/2	19-0	16154.4	0.26		
	20-0	16314.9	-1.76		
	21-0	16477.7	-0.14		
[13.07] 9/2 - X 9/2	5-0	13977.4	-0.32	6.8	-0.26
	6-0	14155.1	-0.02	8.42	-0.06
	7-0	14331.5	0.23		
	8-0	14506.3	0.20	11.31	0.05
	9-0	14680.0	0.19	12.69	0.07
	10-0	14852.2	-0.01	14.18	0.22
	11-0	15023.1	-0.20	15.24	-0.03
	12-0	15193.3	0.05	16.56	-0.01
	13-0	15361.9	0.03	18.28	0.44
	14-0	15529.3	0.06	19.07	-0.03
	15-0	15695.3	-0.06	20.24	-0.09
	16-0	15860.1	-0.17	21.41	-0.13
	17-0	16023.9	-0.02	22.97	0.23
	18-0	16186.5	0.09	23.91	0.00
	19-0	16347.3	-0.23	25.08	0.02
	20-0	16507.4	-0.02	25.9	-0.29
	21-0	16666.1	0.05		
	22-0	16823.6	0.15		
	23-0 *	16976.7	-3.00		
	24-0 *	17136.4	1.84		
	25-0 *	17293.8	5.60		
	26-0 *	17441.8	1.18		
	27-0 *	17598.3	6.46		
	28-0 *	17750.8	9.04		

Table 8-1--continued.

Transition	$^{58}Ni_2^+$ Line Positions			$^{58\text{-}58}Ni_2^+$ - $^{58\text{-}60}Ni_2^+$	
	v'-v"	Frequency	Obs-	Iso-Shift	Obs-
[12.83] ? - X 9/2	29-0 *	17897.3	6.89		
	30-0 *	18044.8	7.00		
[14.57] 9/2 - X 9/2	7-0	15809.9	-0.20		
	8-0	15981.4	0.25		
	9-0	16150.9	0.17	12.23	-0.07
	10-0	16318.8	-0.09	13.76	0.18
	11-0	16485.3	-0.33	15.05	0.21
	12-0	16651.1	0.16	16	-0.05
	13-0	16814.9	0.03	16.84	-0.41
	14-0 *	16976.7	-0.73	17.63	-0.80
	15-0 *	17136.5	-1.93	18.35	-1.23
	16-0 *	17293.8	-4.26		
	17-0 *	17449.0	-7.31		
	18-0 *	17603.5	-9.62		
	19-0 *	17752.0	-16.5		
	20-0 *	17902.5	-20.0		
	21-0 *	18051.9	- 23.1		
[14.96] 7/2 - X 9/2	8-0	16265.7	-0.09	9.88	-0.37
	9-0	16426.1	0.65	10.3	-1.23
	10-0	16583.7	-0.68		
	11-0	16741.7	-0.95	13.86	0.20
	12-0	16902.1	1.80	15.48	0.17
	13-0	17056.5	-0.73	16.88	-0.33

* Not included in regression

Table 8-2. Molecular Constants for $^{58}Ni_2^+$ [cm^{-1}]

Transition	**[09.86]9/2-X9/2**	**[12.83]?-X9/2**	**[13.07]9/2-X9/2**	**[14.57]9/2-X9/2**	**[14.96]7/2-X9/2**
T_{eo}	9770.4	12736.4	12979.8	14482.1	14880.9
ω_e'	182.5	187.4	184.9	182.4	165.8
$\omega_e x_e'$	0.58	0.62	0.62	0.71	(0.34)

calculated shifts, respectively. The solid curve through the center of data points (triangles) gives the correct quantum number assignment while the other remaining curves are calculated assuming the vibrational index is different by ±1 quantum number. Table 8-1 also lists the residuals to a least squares fit of the vibronic band origins to the standard formula, Equation 3-1, from which the constants T_{eo} , ω_e' and $\omega_e x_e'$ were derived (Table 8-2). Perturbations were identified as transition frequencies with a discrepancy of significantly greater than one standard deviation from the fit to Eqn. 3-1 and/or an inconsistent set of isotope shifts. Perturbed upper state vibronic levels were not included in the final regression analysis and determination of vibrational constants. Typically these perturbations were found in the bluer, more congested region of the spectrum. Note that the value of the anharmonicity constant of the [14.96]7/2 state (in parenthesis, Table 8-2) is poorly determined due to the small sample of data; only six transitions were observed in the [14.96]7/2 - X9/2 system. The approximate vibronic band origins were consistently chosen as most intense feature of each band, i.e. the Q-branch head. Full rotational analysis [107] shows that the difference between the true vibronic band origin and the Q-branch head is typically less than a wavenumber.

Figure 8-3 shows the vibrational structure of Ni_2^+ in a plot of transition energy versus excited state quantum number (v' + ½). The solid curves represent the fit to equation (3-1) and the symbols are the experimentally observed vibronic band origins. Despite the perturbations which are evident in this spectrum the overall fit to eq. (3-1) is quite good. This figure clearly shows that all five electronic states have nearly identical vibrational structure.

Selected isotope shifts of corresponding unperturbed transitions in $^{58}Ni^{60}Ni^+$ and $^{58}Ni_2^+$ in two electronic band systems, [09.86]9/2-**X**9/2 and [13.07]9/2-**X**9/2 were scrutinized to obtain an estimate of the ground state vibrational frequency. The effect of the anharmonicity of the ground state was ignored in this determination. This analysis provides a value of $\omega_e'' = 270 \pm 25$ cm^{-1}, significantly greater than all of the excited states thus observed for this molecule.

Discussion

Resonant two-photon, one-color transitions as red as 16,300 cm^{-1} have been reported before [106]. This work provides an improvement of the former study and a refinement of the molecular constants. Moreover, inclusion of the rotational analysis of selected vibronic bands [107] has provided Ω assignments

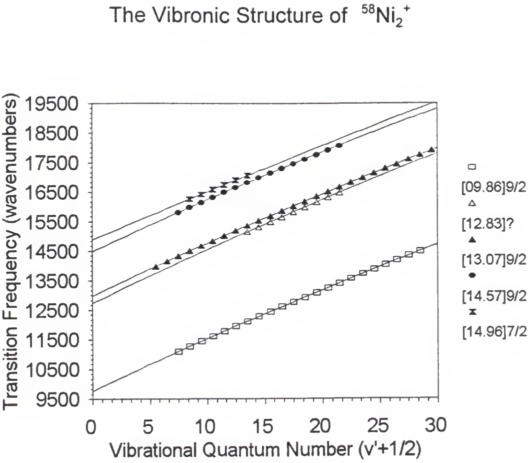

Figure 8-3. Assigned Excited States in $^{58}Ni_2^+$.

The observed vibronic band origins (symbols) of five systems in $^{58}Ni_2^+$ and the least squares fit of this data to equation 3-1 (solid curves). The legend at the right identifies the upper state of each band system (the lower state in each system is the vibronic ground state). The assigned line positions and residuals to the fit are listed in Table 8-1. The vibrational constants derived from the fit are found in Table 8-2.

of the electronic states involved in four band systems. Two new excited states have been identified and spectroscopically characterized for the first time in this study.

A striking consistency exists in the vibrational structure of the low-lying excited states of Ni_2^+. All but one of these states have about the same vibrational frequency (184 cm^{-1}) and anharmonicity (0.6 cm^{-1}). This consistency is graphically represented in Fig. 8-3. Only one excited state observed has a significantly different (lower) vibrational frequency than this manifold of states and it is the only state confirmed to have a different total electronic angular momentum ($\Omega' = 7/2$ as opposed to $\Omega' = 9/2$ for all other confirmed states including the ground state). In addition, all the excited states have a significantly lower vibrational frequency (and a significantly longer bond length [107]) than that of the ground state ($\omega_e'' = 270 \pm 25$ cm^{-1}).

A somewhat similar situation exists in the neutral dimer Ni_2. All the observed vibrational frequencies of the excited states of the nickel dimer neutral (209 $cm^{-1} <= \omega_e' <= 234$ cm^{-1}, [101]) are smaller than that of the ground state ($\omega_e'' = 280 \pm 20$ cm^{-1} [12], 259.2 ± 3.0 cm^{-1} [108]). This has been attributed [101] to a change in the bond order from 1 to ½ upon excitation in the neutral molecule ($3d^8 3d^9 \sigma^2 \sigma^* \leftarrow 3d^9 3d^9 \sigma^2$).

Note that the excited states of bond order ½ in the neutral Ni_2 molecule have a similar but slightly higher vibrational frequency than the excited states observed in the Ni_2^+ ion. Perhaps, then, the excited states of Ni_2^+ are also of bond order ½, with an electronic configuration of $3d^8 3d^8 \sigma^2 \sigma^*$ or more likely

$3d^9 3d^9 \sigma$. But the ground state of Ni_2^+ has a vibrational frequency similar to that of Ni_2 and a binding energy that is slightly higher (2.32 eV for the ion [102,109] 2.042 eV [101] for the neutral). This implies a ground state with a bond order of 1 and perhaps an electronic configuration of $3d^9 3d^8 \sigma^2$. An interesting interpretation of this configuration is that of a ground state neutral Ni atom ($3d^8 4s^2$) forming a coordinate covalent (dative) bond with a ground state Ni^+ ($3d^9$).

The picture which arises for the ground and low-lying states of Ni_2 and Ni_2^+ consistently implies the lack of significant d-orbital contribution to the bonding in these molecules. This is consistent with d-orbital contraction in the late transition period metals. In fact, this leads to a molecular orbital description of three charge states of the nickel dimer: Ni_2^+ $3d^9 3d^8 \sigma^2$, Ni_2 $3d^9 3d^9 \sigma^2$ [101], Ni_2^- $3d^9 3d^9 \sigma^2 \sigma^*$ [108], that is somewhat consistent with the observed bond energies: 2.32 eV, 2.04 eV [101], and 1.84 eV [110] for Ni_2^+, Ni_2, and Ni_2^- respectively. Presumably the increase in bond energy between Ni_2 and Ni_2^+ is due to the presence of charge induced-dipole forces in the dissociation of the ion. What remains most puzzling are the major differences between Ni_2 and Ni_2^+:

1) Ni_2^+ has high electron orbital angular momentum in its ground state ($\Omega'' = 9/2$) but Ni_2 has low angular momentum ($\Omega'' = 0$)
2) Ni_2^+ has a larger adiabatic binding energy than Ni_2, but actually has a longer bond length (cation 2.242 Å [10]; neutral 2.1545 Å). Perhaps this is the effect of the charge induced-dipole forces absent in the neutral dimer.

3) High level *ab initio* theory [105] predicts the correct ground state angular momentum for Ni_2 but not Ni_2^+
4) Theory [105, 111] accurately predicts the bond length of Ni_2^+ but not Ni_2

The more the details of such complex diatomic molecules are understood, the better will it be to predict the behavior of larger molecules or even real catalytic surfaces. But with a more immediate perspective, hopefully, the data presented here will be helpful for new or revised theoretical studies of isolated transition metal molecular systems.

Part B: Heteronuclear Diatomic Ion

In the past decade, both neutral [112-3] and charged [114-5] heteronuclear diatomic ions have been a subject of various research groups and theory has predicted some of the spectroscopic constants for various metal dimers [116-8]. Despite tremendous effort undertaken by several groups clear understanding of the bonding and electronic structure in these cluster systems is not yet forthcoming.

What makes the study of these clusters fascinating is the complexity or mystery that both experiments and calculations have to unravel regarding the electronic configuration and binding nature of the partners. Most neutral

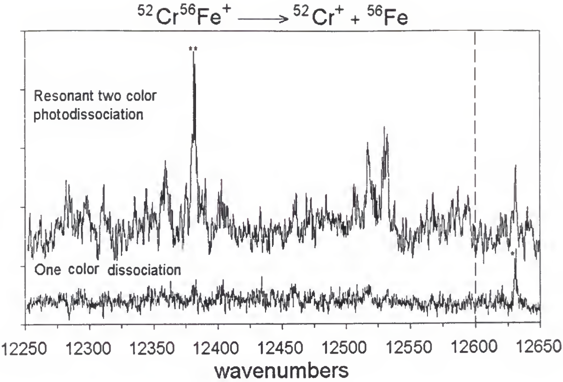

Figure 8-4. Photodissociation Spectrum of $^{52}Cr\,^{56}Fe^+$.

A portion of the photofragmentation excitation spectra of $^{52}Cr^{56}Fe^+$ observed in the region of 12 250 to 12 650 cm^{-1} is shown. The bottom panel, shows one-color dissociation (*also one-photon transition, see Fig. 8-5) and is labeled as such; while the top panel obtained under conditions that favor two-color photodissociation (**see Figure 8-6) reveals new peaks to the red of 12 600 cm^{-1}. The dashed line, at 12 600 cm^{-1} marks the upper limit to the adiabatic binding energy of $CrFe^+$ (D_0'' =12 600 ± 100 cm^{-1}). The onset of one photon dissociation, in the blue, near the dashed line occurs in all isotopic variants of $CrFe^+$.

transition metals are in the $d^n s^2$ ground state electron configuration and generally are promoted to the excited state $d^{n+1} s^1$ atomic limit in order for the strongest bond to form, for example Ni_2 [101]. Of course, the cost of the promotion energy has to be lower than the gain that results from forming a σ - bond. Extensive literature on neutral dimer exists both from experiment [98] and theory [116], however, little is known about dimer cations. Spectroscopic parameters of Ni_2^+ have been discussed in Part A ; data obtained from photodissociation studies of $CrFe^+$ are discussed here and this information contributes to the growing data base of metal-metal ions.

The Binding Energy of $(CrFe)^+$

Figure 8-4 shows the photodissociation action spectrum of $^{52}Cr^{56}Fe^+ \rightarrow$ $^{52}Cr^+ + {}^{56}Fe$ in the visible region (12 250 to 12 650 cm^{-1}). The bottom trace shows a one color dissociation (which is also one photon, see Figure 8-5) spectrum. The lowest energy transitions that lead to a single photon dissociation are found just above 12 600 cm^{-1} (marked with a dashed line) for all isotopic variants of $CrFe^+$ and increase in occurrence to the blue. The onset of one photon dissociation transition at 12 629 cm^{-1} indicates a threshold for a dissociation mechanism which ultimately sets the upper limit of $D_0'' = 12\,600 \pm 100$ cm^{-1} for the adiabatic dissociation energy , of Cr^+-Fe. The observed transition via one color technique is clearly due to a one-photon dissociation mechanism as confirmed by a linear laser power dependence of the dissociation yield, shown in Figure 8-5.

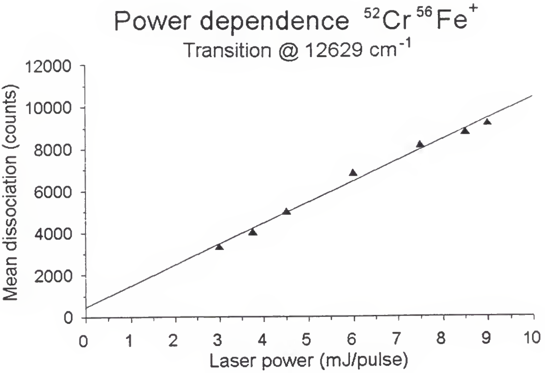

Figure 8-5. Evidence of One-Photon Dissociation in CrFe$^+$.

The figure shows a linear relationship between the average photofragmentation yield (vertical axis) and the laser power (horizontal axis). This behavior confirms that the transition observed for $^{52}Cr^{56}Fe^+ \rightarrow {}^{52}Cr^+ + {}^{56}Fe$, at 12 629 cm^{-1} is a single-photon transition.

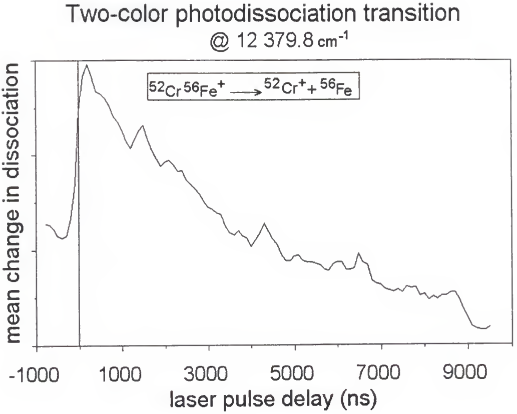

Figure 8-6. Evidence of Two-Color Photodisociation in $CrFe^+$.

The figure is obtained by setting the excitation laser on a resonance transition at 12 379.8 cm^{-1} (with ≈ 5 mJ/cm^2 pulse) and its pulses are scanned in time relative to a fixed non-resonant dissociation laser pulse (@ 641.6497 nm with ≈ 25 mJ/cm^2 pulse). When the two lasers cross (~1200 ns) , referenced as 0 ns laser pulse delay in this figure, a sharp change in the dissociation yield is indicative of two-color enhancement. This transition is marked with two asterisks in Figure 8-4 and together with the peaks around 12 525 cm^{-1} serve as a lower limit to the adiabatic binding energy of $CrFe^+$.

In order to obtain the two-color photodissociation (R2CD) spectrum, the first excitation laser pulse (≈ 5mJ/cm^2 pulse) is used to resonantly prepare some vibronic level of the molecular ion but does not alone induce significant dissociation. The second dissociation laser pulse delayed by ~1200 ns from the first laser, dissociates the prepared excited molecular ions. The dissociation laser was fixed at 641.6497 nm which is non-resonant with the nascent parent ions. This technique when successful (R2CD) is a powerful tool of probing excited states that with one color-dissociation alone would otherwise be undetectable. The two color spectrum in Figure 8-4, upper trace, has several peaks to the red of 12 600 cm^{-1} that do not occur in the one color spectrum. The peak at 12 379.8 cm^{-1} is highlighted in Figure 8-6 where the timing scan between the resonant excitation laser pulse and the non-resonant dissociation laser pulse indicates that this transition is indeed due to a resonant two color photodissociation, R2CD, (two photon) mechanism, shown in Figure 2-8. The decay of the curve in Figure 8-6 is directly related to the lifetime of CrFe$^+$ in the probed excited state. Unfortunately, due to variety of decays that this molecular ion undergoes, the exact determination of the lifetime has become obstructed.

Evidence of Two Pathways in the Photofragmentation of CrFe$^+$

For homonuclear diatomic ions, localization of the charge (positive or negative) is trivial. However, in heteronuclear diatomic ions, the electron density is polarized such that the positive charge is placed on the metal with a lower ionization potential. However, in this study CrFe$^+$ photodissociates to produce

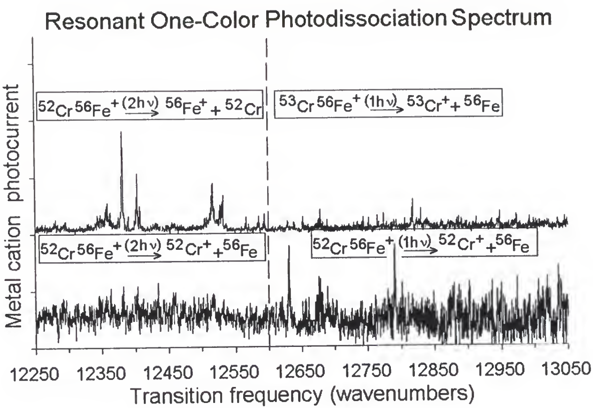

Figure 8-7. Two Pathways in the Photodissociation of $CrFe^+$.

Above the adiabatic threshold, 12 600 cm^{-1}, of Cr^+-Fe (indicated by a dashed line) 'normal' or expected behavior is observed with Cr^+ as a photofragment in the resonant photodissociation of $CrFe^+$. However, at lower laser frequency (< 12 600 cm^{-1}) both pathways are turned on with evidence of Fe^+ as an additional photofragment.

both Cr^+ and Fe^+ as photoproducts, in spite of the difference in the first ionization potentials: (IP of 6.766 eV for Cr [1] and IP of 7.870 eV for Fe [1])

Figure 8-7 shows a portion of the one color resonant photodissociation spectrum in the region 12 250 to 13 050 cm^{-1} with evidence of the two dissociation pathways: (a) $CrFe^+ \rightarrow Cr^+ + Fe$ or (b) $CrFe^+ \rightarrow Fe^+ + Cr$. The bottom panel shows the lighter molecular ion $^{52}Cr^{56}Fe^+$ dissociating via path (a); while the top panel shows both the heavier isotopic variant $^{53}Cr^{56}Fe^+$ also separating by following the first path (a) and a different dissociating channel for $^{52}Cr^{56}Fe^+$, that is path (b). The dashed line at 12 600 cm^{-1} serves the same purpose as already explained in Figure 8-4, that is, it sets an upper limit to the adiabatic energy of $CrFe^+$. To the blue of this threshold all observed transitions are due to path (a) with preference of Cr^+ ion as a photofragment with measured resonant features up to 17 250 cm^{-1}. However, the overly congested spectrum has made it difficult to assign vibrational progressions.

Interesting and yet unclear dynamics take place to the red of 12 600 cm^{-1}, that is, in addition to detecting Cr^+ photofragment, Fe^+ is produced as a product. Why? In an attempt to provide 'hints' for the occurrence indicated in Figure 8-7, a laboratory kinetic energy spectrum (shown in Figure 8-8) of photoexcited $CrFe^+$ was measured. That is, the field strength of the 180° kinetic energy filter is scanned to transmit produced fragment ions from the mass-selected $CrFe^+$ complex. The spectrum shown in Fig.8-8 maybe considered as a secondary mass spectrum since for the experimental design in the Brucat laboratory the ratio of

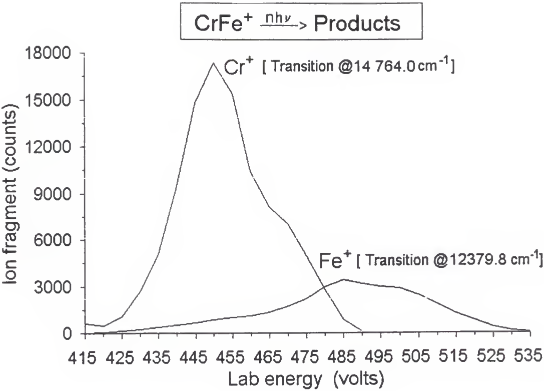

Figure 8-8. Products Produced in the Photodissociation of $CrFe^+$.

This figure shows two photofragments of $CrFe^+$ from dissociating the parent ion with two different laser frequencies: 1) at a higher frequency 14 764.0 cm^{-1} the Cr^+ photofragment is detected as a primary product and 2) in the red, 12 379.8 cm^{-1} Fe^+ is favored. In this spectrum, the field strength of the 180° electrostatic sector is scanned to transmit produced fragment ions from the isolated $CrFe^+$ molecular ion.

Table 8-3. Experimental and Theoretical Ground State Binding Energies, D_0'' in eV, of Transition Metal Dimer Cations.

Molecular Ion	Experiment (PD)	Experiment *(CID)	**Estimated % Error	Theory	***Calc. % Error
Ti_2^+	2.43[a]	2.37[g]	2.5	-	-
V_2^+	3.14[a]	3.13[g]	0.39	-	-
Cr_2^+	2.13[b]	2.74[g]	-29	1.86[k]	13
Mn_2^+	1.39[c]	0.85[h]	39	1.08[l]	28
Fe_2^+	2.92[d]	2.72[i]	6.8	-	-
Co_2^+	2.76[a]	1.92[g]	30	-	-
Ni_2^+	2.32[e]	2.08[j]	10	1.86[m]	20
$CrFe^+$	**1.55[f]**	-	-	-	-

*Collisional induced dissociation (CID) measurements are good to within 50% error.
**Estimated % error : (PD-CID)/(PD)*100
***Calc. % error : (PD-Theory)/(PD)*100
[a]Ref. [119], [b]Ref. [120], [c]Ref. [121], [d]Ref. [122], [e]Ref. [102], [f]This work, [g]Ref. [123], [h]Ref. [124], [i]Ref. [125], [j]Ref. [110], [k]Ref. [126], [l]Ref. [127], [m]Ref. [105]

parent to daughter mass is equivalent to that of parent to daughter kinetic energy. That is, for an isolated parent $^{52}Cr^{56}Fe^+$ ion, the voltage difference of 940 V (referred to as Lab. energy in Fig. 8-8) was applied to the hemispherical electrostatic sector for optimum transmission of parent ions having ca. 1450 V kinetic energy. The photoexcited $CrFe^+$ ion (prior to entrance to the electrostatic sector) produced $^{52}Cr^+$ ion fragment determined at laboratory energy of 452 V whereas $^{56}Fe^+$ ion fragment action occurred at 487 V. The transition at 12 379.8 cm^{-1} favored the second pathway with Fe^+ detected as a photoproduct while the transition at 14 764.0 cm^{-1} favored the first pathway resulting mainly in Cr^+ photofragment.

Overview

In this chapter, binding energies of both Ni_2^+ and $CrFe^+$ have been presented. High-resolution photodissociation spectroscopy (specifically R2CD) has provided both excited and ground states spectroscopic constants for Ni_2^+. Two pathways in the photofragmentation action spectrum of $CrFe^+$ have been measured. Comparisons of observed bond energies of diatomic metal cations via photodissociation spectroscopy to estimations from collisional induced dissociation (CID) methods and theoretical predictions are made in Table 8-3. These values provide critical test for CID methods for determining accurate thermochemistry for transition metal cluster and also test for theoretical models. Both theory and CID methods indicate an approximately 30 % deviation from photodissociation experimental observations.

CHAPTER 9
CONCLUSIONS

Earlier work [4,5] in the Brucat research group involved the characterization of a variety of novel cluster ions studied via photodissociation spectroscopy in the visible region. Experimental data indicate that the bonding in metal cation-ligand systems is diverse and depends greatly on the electron configuration of the metal cation. This is illustrated in numerous tables of data completed in the past decade. The first tabulation of molecular constants (completed in 1992) for the following diatomic ions VAr^+, $CoAr^+$, $NiAr^+$, $ZrAr^+$, $CaKr^+$, VKr^+, $CoKr^+$, $CrAr^+$, Cr_2^+, Ni_2^+ and Ca_2^+ appeared elsewhere [4], in addition, the following polyatomic ions $V(H_2O)^+$, $V(CO_2)^+$, $V(NH_3)^+$ and $V(N_2)^+$ were also spectroscopically probed.

Since 1992 the above molecular ions have been re-visited and constants of new excited states occurring redder (lower energy region) than the above study for $CoAr^+$, $NiAr^+$ and $ZrAr^+$ have been measured and are tabulated in this reference [5]. New spectroscopic constants for the following molecular ions, $Co(H_2O)^+$, $Ni(H_2O)^+$, $Ni(CO_2)^+$, $Co(CO_2)^+$ and $Co(N_2)^+$ are also tabulated [5]. Tables 9-1 and 9-2 summarize both revised and new molecular constants for the research work completed here.

An increase in binding energy as a function of the size of the rare gas in all investigated molecular ions is observed [see Chapter 4]. This behavior is due to increasing polarizability in the series, Ar < Kr < Xe. $CoAr^+$ is a very interesting and yet rich system and it is not surprising that it is still currently been investigated in the Brucat research group. The first excited states to be studied (A, B, C [4]) have been re-labeled as b, C, D respectively and A' [5] as A. The purpose of re-examining this molecular ion here was not to determine new excited states since that has been done [5], however, there was a gap of about 500 cm^{-1} between data acquired in 1989 and that competed in 1994 and perturbations in the spectrum made it necessary to do further investigations for completeness of this study.

However, trends in the binding energy as a function of the size of the metal cation are not trivial to speculate; from both experimental observations [Chapter 5] and theoretical predictions [91, 116]. Nonetheless, as a general trend, the d-orbital contraction plays a vital role, meaning that, for a transition metal atom with a higher atomic number the contraction is larger, thus the rare gas or ligand is capable to bind 'stronger' to a smaller size atomic ion. As a result metal cations with an occupied s-orbital have relatively smaller binding energies due to increase radial distance. Photodissociation of $TaAr^+$ provides, for the first time, spectroscopic details (of both ground and excited states) for a third-row containing transition metal cation, complex to be studied.

Table 9-1. Spectroscopic Parameters of Studied Diatomic Ions [cm^{-1}].

System	State Label	M^+ Term Symbol	Molecular Term Symbol	T_{00}	D^* (LB)	D_0	ω_e	$\omega_e x_e$
$CaAr^+$	X	^2S ($4s^1$)	$^2\Sigma^+$	-	-	890	-	-
	C	^2D ($3d^1$)	$^2\Sigma^+$	14072	-	429	42	0.96
$CaKr^+$	X	^2S ($4s^1$)	$^2\Sigma^+$	-	-	840^a	74	-
	C	^2D ($3d^1$)	$^2\Sigma^+$	14217	-	301	60	2.8
$CoAr^+$	X	$^3F_4$ ($3d^8$)	$^3\Delta_3$	-	4111	4111	-	-
	a	$^1D_2$ ($3d^8$)	$^3\Delta_2$	12552	-	3210	120	-
	b	$^1D_2$ ($3d^8$)	-	13193	15759	2569	155	2.41
	A	$^3F_4$ ($3d^74s$)	$^3\Phi_4$	12505	13922	1420	100	2.15
	C	$^3F_2$ ($3d^74s$)	-	13451	15432	1983	119	2.04
	D	$^3P_2$ ($3d^8$)	-	14549	17369	2825	175	3.26
$CoKr^+$	X	$^3F_4$ ($3d^8$)	$^3\Delta_3$	-	5405	5405	-	-
	a	$^1D_2$ ($3d^8$)	$^3\Delta_2$	12553	-	4503	-	-
	b	$^1D_2$ ($3d^8$)	-	13413	17010	3644	148	1.47
	C	$^3F_2$ ($3d^74s$)	-	13935	16730	2792	118	1.35
	D	$^3P_2$ ($3d^8$)	-	14753	18658	3913	158	1.76
$CoXe^+$	X	$^3F_4$ ($3d^8$)	$^3\Delta_3$	-	7700	7700	257	-

Table 9-1--continued.

System	State Label	M$^+$ Term Symbol	Molecular Term Symbol	T_{00}	D* (LB)	D_0	ω_e	$\omega_e x_e$
CoXe$^+$	a	$^1D_2$ (3d^8)	$^3\Delta_2$	12575	-	6776	237	-
	b	$^1D_2$ (3d^8)	-	13711	-	5640	158	1.29
	A	$^3F_4$ (3d^{7}4s)	$^3\Phi_4$	13028	17629	4485	124	0.888
	B	-	-	13748	18404	4656	124	0.786
	C	$^3F_2$ (3d^{7}4s)	-	14142	-	4880	129	0.837
	D	$^3P_2$ (3d^8)	-	15033	20890	5929	161	1.13
VAr$^+$	X	^5D (3d^4)	$^5\Sigma$	-	2974	2974	-	-
	A	-	-	15116	-	1196	95.4	1.83
	B	$^5P_2$ (3d^{3}4s)	-	15217	16577	1360	90.4	1.56
	B'	-	-	15207	-	1283	87.1	1.43
NbAr$^+$	X	^5D (3d^4)	$^5\Sigma$	-	3106	3106	-	-
	a	-	-	11747			84.6	0.809
	b	$^3G_5$ (4d^4)	-	-	14026	-	-	-
	A	-	-	12456	-	1022	81.2	1.5
	B	$^5P_2$ (4d^{3}5s)	-	12739	13941	1202	82.3	1.46
TaAr$^+$	X	^5F (5d^{3}6s)	-	-	2000	2000	-	-
	A	-	-	13701	-	1416	79.3	1.08

Table 9-1--continued.

System	State Label	M^+ Term Symbol	Molecular Term Symbol	T_{00}	D^* (LB)	D_0	ω_e	$\omega_e x_e$
$TaAr^+$	B	-	-	15201	-	728	64.8	1.38
	C	-	-	15547	16293	746	48.1	0.806
	D	-	-	15693	-	906	42.2	0.48
$TaAr^+$	E	-	-	17471	-	834	147	5.96
Ni_2^+	X	-	-	-	18710[b]	18710	270	
	[9.86]9/2	-	-	9860	-	-	183	0.58
	[12.83]?	-	-	12380	-	-	187	0.62
	[13.07]9/2	-	-	13070	-	-	185	0.62
	[14.57]9/2	-	-	14570	-	-	182	0.71
	[14.96]7/2	-	-	14960	-	-	166	0.34
$CrFe^+$	X	-	-	-	12600[b]	12600	-	-

[a] Accepted binding energy for $CaKr^+$ is 1400 cm^{-1} [15].

[b] Upper limit determined via R2CD [102] and this work.

(LB) Dissociation limit determined from Leroy-Bernstein analysis of data. Note that where there is no data entry for LB D_0^*, the binding energies, D_0, are estimated via a Birge-Sponer approximation or derived from $D_0' = [(D_0'' + \Delta E_{Atomic}) - T_{00}]$.

Table 9-2. Spectroscopic Parameters of Studied Polyatomic Ions [cm^{-1}].

System	State	M^+ Term Symbol[a]	Molecular Term Symbol[b]	T_{00}	D*(BS)	D_0	ω_s	x_{ss}
$FeCO^+$	X	^4F ($3d^7$)	$^4\Sigma^-$	-	13090	13090	-	-
	A	^4P ($3d^7$)	-	14689	24890	10200	312	2.39
$FeCO_2^+$	X	^6D ($3d^64s$)	$^6\Delta$	-	3920	3920	-	-
	a	^4P ($3d^7$)	-	14535	17590	3050	181	2.68

(BS) Dissociation limit determined from Birge-Sponer approximation
Predicted by theory: [a]Ref. [9] [b]Ref. [80 and 96] for $FeCO^+$ and $FeCO_2^+$ respectively.

In addition, high-resolution photodissociation of $FeCO^+$ [Chapter 7] pioneers the series of transition metal cation-carbonyl complexes that are spectroscopically probed. The photodissociation study of $Fe(CO_2)^+$ adds a forth system to the already investigated $V(CO_2)^+$ [97], $Co(CO_2)^+$ [17] and $Ni(CO_2)^+$ [86] molecular ions, which aid in learning more about the trends in binding energies as a function of the size of the transition metal ion. The bond strength increases in the series $Fe(CO_2)^+ < V(CO_2)^+ < Co(CO_2)^+ < Ni(CO_2)^+$.

The binding energy of a heteronuclear diatomic ion, $CrFe^+$, has been determined as 1.55 eV [Chapter 8]. In addition, new information about the excited states of Ni_2^+ are presented.

In the future, related systems of other transition metals can be investigated in addition to second ligands added to the simplified binary ion (M^+-L) complexes. Hopefully, examples of systems containing other transition metals (essentially all transition metals) when completed will provide solid benchmarks for theoretical models.

APPENDIX A
GENERATION OF IONS OR MOLECULES IN THE PLASMA AND DETERMINATION OF THE CONCENTRATION OF CARRIER GAS MIXTURE

Generation of Ions or Molecules

In order to successfully study mass-selected molecular ions using photodissociation spectroscopy a sufficient number of ions have to be generated in the plasma. The studied molecular ions, in this dissertation, are produced in a pulsed-laser-driven supersonic expansion source. The formation of ions is initiated by the interaction of Nd^{3+} :YAG pulsed laser (532 nm light with 7 ns duration and 10 - 40 mJ/pulse) with a solid target. Ionization and heating rates are determined by the intensity and duration of the laser pulse. The laser light is focused to a point smaller than 1 mm in diameter which corresponds to a photon fluence of 10^8 to 10^9 W/cm^2 at the rod surface. An estimation of vaporized material is given by [128];

$$\frac{No.\ of\ molecules}{pulse} = \frac{U(J/pulse)}{\Delta H_{vap}} * N_A \qquad \text{(A-1)}$$

where U is the internal energy per laser pulse, ΔH_{vap} is the heat of vaporization of the metal and N_A is Avagadro's number. However, the fractional ionization of vaporized material is a function of the initial temperature of the plasma which is estimated as 7000 K here.

Upon interrogation with green light (532 nm) the spatial profiles of the ion and the electron density at the surface of a target rod changes, that is, the ion density decreases from solid state value down to zero where as the electrons spread out to some extent. The Saha equation [128] relates the electron number density n_e to the number densities n_i and n_{i-1} of two ions that differ by only one stage of ionization, and the relationship is given by:

$$\frac{n_e n_i}{n_{i-1}} = \frac{2u_i}{u_0} * \frac{2\pi m_e kT}{h^2} e^{\frac{-IP}{kT}} \tag{A-2}$$

where u_i and u_0 are electronic partition functions. Thus the fraction of ions can be estimated as;

$$\frac{No.\ of\ ions}{pulse} \approx \frac{No.\ of\ molecules}{pulse} * e^{\frac{-IP}{kT}} \tag{A-3}$$

For an example, we assume the target metal is iron: substituting the ionization potential (IP) of iron (7.87 eV [1]) and the heat of vaporization (351 kJ/mol [1]), with a laser pulse of 20 mJ/pulse into Eqn. 3, will give roughly 10^{10} ions and about a factor of 100 to 1000 will be lost in the collimating process following the adiabatic expansion. Which leaves approximately 10^7 to 10^8 ions made.

Determination of the Concentration of Carrier Gas Mixture

For all investigated molecular ions, [Chapters 3 to 8], approximately a 1 % seeded carrier gas of He with the ligating species was used. The concentration of the prepared gas mixture can be measured by using the time of arrival at the "A" chamber (obtained from using the Brucat group experimental apparatus) using the following expression,

$$t_u = t_{He}\sqrt{\frac{M_u}{M_{He}}} \tag{A-4}$$

The arrival time of the molecular beam depends on the speed of sound of the carrier gas. On average the time of arrival (TOA) of the generated molecular beam using pure He as a carrier gas is 620 μs. However, for a seeded gas the TOA is expected to increase as a function of the ligating gas average molecular weight. Typical recorded TOA from the experiment with a 1 % Ar tank is 647 μs.

APPENDIX B
DETERMINATION OF LEROY-BERNSTEIN CONSTANT, -$K^{4/3}$, FOR DERIVING THE POLARIZABILITY OF A RARE GAS ATOM IN THE PRESENCE OF A POSITIVE CHARGE

The LeRoy-Bernstein (LB) constant (- $K^{4/3}$) is unique for each studied diatomic ion and can be directly derived from the slopes of LB plots [chapters 4 and 5]. K which is a combination of fundamental constants is defined as [14, 42],

$$K = \frac{hC^{-1/n} n\Gamma(1+1/n)}{(2\pi\mu)^{1/2}\Gamma(1/2+1/n)} \tag{B-1}$$

where n is the order of 1/r in the long-range attractive part of the diatomic potential. For diatomic ions whose principal force is the charge-(induced dipole), n = 4. Γ is the standard gamma function [129], μ is the reduced mass of the diatomic and h is the Planck constant. The gamma function is evaluated below as,

$$\frac{n\Gamma(1+1/n)}{\Gamma(1/2+1/n)} = \frac{4*\Gamma(1.250)}{\Gamma(0.750)} = \frac{4*0.90640247}{1.2254167} = 2.95866 \tag{B-2}$$

and C is defined as,

$$C = \frac{q^2\alpha}{2} = \frac{(4.8024*10^{-10}esu)^2\alpha}{2} \tag{B-3}$$

where α is the polarizability in cm^3 and q is a full electron charge on the metal (1 esu = $cm^{3/2}\, g^{1/2}\, s^{-1}$). Then $C^{-1/4}$ yields,

$$C^{-1/4} = (54279.6302\ \alpha^{-1/4})\ g^{-1/4}\ cm^{-3/2}\ s^{1/2}$$

Substituting the standard constants, results of steps (B-2) and (B-3) into equation (B-1) simplifies K into,

$$= \frac{(6.626 * 10^{-27} g\ cm^2\ s^{-1})(2.95866)(54279.6302\alpha^{-1/4} g^{-1/4} cm^{-3/2} s^{1/}}{(2.5066\mu^{1/2} g^{1/2})} \qquad \text{(B-4)}$$

evaluating all the numbers K can be expressed as,

$$K = (4.2452*10^{-22}\ \alpha^{-1/4}\ \mu^{-1/2})\ g^{1/4}\ cm^{1/2}\ s^{-1/2}$$

converting to SI units yields,

$$K = (7.5479656*10^{-24}\ \alpha^{-1/4}\ \mu^{-1/2})\ Kg^{1/4}\ m^{1/2}\ s^{-1/2}$$

Converting joules into wavenumbers (since 1 J = kg $m^2\, s^{-2}$)

$$K = 7.5479656 * 10^{-24} \alpha^{-1/4} J^{1/4} * \frac{(50341.1 cm^{-1})^{1/4}}{(1 * 10^{-18} J)^{1/4}} \qquad \text{(B-5)}$$

then collecting all the values yields K of,

$$K = (3.57528*10^{-18}\ \alpha^{-1/4}\ \mu^{-1/2})\ cm^{-1/4}$$

By converting the polarizability (α) cm^3 into $Å^3$ and representing the reduced mass (μ) in amu the above value of K can be re-written as,

$$K = (3.57528*10^{-18}\ \alpha^{-1/4}\ \mu^{-1/2})\ cm^{-1/4}\ (10^{-24})^{-1/4}\ (6.022*10^{23})^{1/2}$$

which yields,

$$K = 2.774\ \alpha^{-1/4}\ \mu^{-1/2}$$

then,

$$-K^{4/3} = \frac{-3.898}{\mu^{2/3}\alpha^{1/3}} \qquad \text{(B-6)}$$

Finally we examine the cube of equation (B-6),

$$-K^{4}\mu^{2} = \frac{-59.228}{\alpha} \qquad \text{(B-7)}$$

LIST OF REFERENCES

[1] D. R. Lide (editor) *CRC Handbook of Chemistry and Physics*, 71st ed. 1990-91,CRC Press, Boston (1990)

[2] A. A. Radzig and B. M. Smirnov, *Reference Data on atoms, molecules and ions*, Springer-Verlag, Berlin Heidelberg (1985)

[3] D. E. Lessen, R. L. Asher and P. J. Brucat, J. Chem. Phys., **93** (1990) 6102

[4] D. E. Lessen, *Spectroscopic characterization of novel cluster ions*, Ph.D. Dissertation, University of Florida, Gainesville (1992)

[5] R. L. Asher, *Experimental and theoretical investigation and characterization of small molecular ions*, Ph. D. Dissertation, University of Florida, Gainesville (1995)

[6] M. Rosi, C. W. Bauschlicher Jr., J. Chem. Phys., **90** (1989) 7264

[7] M. Rosi, C. W. Bauschlicher Jr., J. Chem. Phys., **92** (1990) 1876

[8] P. Baunstein, D. Matt and D. Nobel, Chem. Rev., **88** (1988) 747

[9] C. E. Moore, *Atomic Energy Levels*, NSRDS-NBS Circular # 467, US GPO, Washington DC (1949)

[10] R. E. Smalley, L. Wharton and D. Levy, Acct. Chem. Res., **10** (1977) 139

[11] D. Bellert, T. Buthelezi, V. Lewis, K. Dezfulian and P. J. Brucat, Chem. Phys. Lett., **240** (1995) 495

[12] J. O. Hirschfelder, C. F. Curtiss and R. B. Bird, *Molecular theory of gases and liquids*, John Wiley & Sons, New York, (1964)

[13] D. H. Levy, Ann. Rev. Phys. Chem., **31** (1980) 197

[14] R. J. LeRoy and R. B. Bernstein, J. Chem. Phys., **52** (1970) 3869

[15] S. H. Pullins, C.T. Scurlock, J. E. Reddic and M. A. Duncan, J. Chem. Phys., **104** (1996) 7518

[16] C. S. Yeh, J. S. Pilgrim, K. F. Willey, D. L. Robbins, and M. A. Duncan, Int. Rev. Phys. Chem., **13** (1994) 231

[17] R. L. Asher, D Bellert, T. Buthelezi, and P. J. Brucat, Chem. Phys. Lett., **227** (1994) 623

[18] R. L. Asher, D. Bellert, T. Buthelezi, and P. J. Brucat, Chem. Phys. Lett., **228** (1994) 599

[19] P. J. Brucat, D. E. Lessen, and R. L. Asher in *Advances in Metal and Semiconductor Clusters*, **Volume I**, M.A. Duncan (editor) JAI Press, New York, (1991) 267-302

[20] J. S. Pilgrim, C. S. Yeh, K. R. Berry, and M. A. Duncan, J. Chem. Phys., **100** (1994) 7945

[21] J. S. Pilgrim, C. S. Yeh, and M. A. Duncan, Chem. Phys. Lett., **210** (1993) 322

[22] S. I. Panov, J. M. Williamson, and T. A. Miller, J. Chem. Phys., **102** (1995) 7359

[23] C. Luder and M. Velegrakis, J. Chem. Phys., **105** (1996) 2167

[24] K. V. Subbaram, J. A. Coxon and W. E. Jones, Can. J. Phys., **54** (1976) 1535

[25] D. Lessen and P. J. Brucat, J. Chem. Phys., **90** (1989) 6296

[26] D. Bellert, T. Buthelezi, K. Dezfulian, T. Hayes and P. J. Brucat, Chem.Phys. Lett., **256** (1996) 555

[27] T. Buthelezi, D. Bellert, T. Hayes and P. J. Brucat, Chem. Phys. Lett., **262** (1996) 303

[28] R. L. Asher, D. Bellert, T. Buthelezi and P. J. Brucat, Chem. Phys. Lett., **227** (1994) 277

[29] T. Buthelezi, D. Bellert, V. Lewis and P. J. Brucat, Chem. Phys. Lett., **242** (1995) 627

[30] T. Buthelezi, D. Bellert, V. Lewis and P. J. Brucat, Chem. Phys. Lett., **246** (1995) 145

[31] D. Lessen and P. J. Brucat, J. Chem. Phys., **91** (1989) 4522

[32] H. Partridge and C. Bauschlicher Jr., J. Chem. Phys., **98** (1994) 2301

[33] P. R. Kemper, M. Hsu and M. T. Bowers, J. Phys. Chem., **95** (1991) 10600

[34] N. Aristov and P.B. Amentrout, J. Phys. Chem., **90** (1986) 5135

[35] C. W. Bauschlicher Jr., H. Partridge and S. R. Langhoff, J. Chem. Phys., **91** (1989) 4733

[36] H. Partridge, C. W. Bauschlicher Jr. and S. R. Langhoff, J. Phys. Chem., **96** (1992) 5350

[37] C. W. Bauschlicher, Jr. and H. Partridge, Chem. Phys. Lett, **239** (1995) 241

[38] T. Bustug, W. Sepp, B. Fricke, E. Johnson and C. M. Barshick, Phys. Rev. A, **52** (1995) 2734

[39] C. W. Bauschlicher Jr., H. Partridge and S. R. Langhoff, Chem. Phys. Lett., **165** (1990) 272

[40] C. Heinemann, J. Schwarz, W. Koch and H. Schwarz, J. Chem. Phys. **103** (1995) 4551

[41] G. Herzberg, *Molecular Spectra and Molecular Structure, Spectra of Diatomic Molecules*, D. Van Nostrand Company, INC, (1950)

[42] R. J. LeRoy and R. B. Beinstein, J. Mol. Spectrosc., **37** (1971) 109

[43] J. Sugar and C. Corliss, J. Phys. Chem. Ref. Data, **10** No.4 (1981) 1097

[44] R. M. Badger, J. Chem. Phys., **2** (1934) 128

[45] R. L. Asher, D. Bellert, T. Buthelezi, D. Lessen and P. J. Brucat, Chem.Phys. Lett., **234** (1995) 119

[46] R. L. Asher, D Bellert, T Buthelezi, and P. J. Brucat, Chem. Phys. Lett., **228** (1994) 599

[47] D. E. Lessen, R. L. Asher and P. J. Brucat, Chem. Phys.Lett., **177** (1991) 380

[48] R. H. Schultz, K. C. Crellin and P. B. Armentrout, J. Am. Chem. Soc.,**113** (1991) 8590

[49] A. Freitag, C. van Wullen and V. Staemmler, Chem. Phys. **192** (1995) 267

[50] C. L. Laio and C. Y. Ng, J. Chem. Phys., **84** (1986) 1142

[51] S. H. Sheen, G. Dimoplon, E. K. Parks and S. Wexler, J. Chem. Phys. **68** (1978) 4950

[52] D. Bellert, T. Buthelezi, T. Hayes and P. J. Brucat, Chem.Phys. Lett., submitted

[53] D. Lessen and P. J. Brucat, J. Chem. Phys. **91** (1989) 4522

[54] T. Hayes, T. Buthelezi, D. Bellert, and P. J. Brucat, manuscript in preparation

[55] J. F. Wyart, Optica Pura y Appl. **10** (1977) 177

[56] K. V. Subbaram, J. A. Coxon and W. E. Jones, Can. J. Phys., **54** (1976) 1535

[57] D. E. Lessen, R. L. Asher and P. J. Brucat, Chem. Phys. Letters, **177** (1991) 380

[58] A. Dalgrano and A. E. Kingston, Proc. Roy. Soc. A **259** (1960) 424

[59] C.T. Scurlock, J. S. Pilgrim and M.A. Duncan, J. Chem. Phys. **103** (1995) 3293

[60] P. Pyykko, J. Am. Chem. Soc. **117** (1995) 2067

[61] P. W. Atkins, *Physical Chemistry*, 5th ed., W. H. Freeman and Co., New York (1994)

[62] D. Bellert, T. Buthelezi, T. Hayes and P. J. Brucat, J. Chem. Phys., submitted (1997)

[63] D. E. Lessen, R. L. Asher, and P. J. Brucat, Int. J. Mass. Spec. Ion. Process., **102** (1990) 331

[64] R. H. Orcutt and R. H. Cole, J. Chem. Phys., **46** (1967) 697

[65] A. C. Newell and R. C. Baird, J Appl Phys., **36** (1965) 3751

[66] N. E. Hill, W. E. Vaughan, A. H. Price, and M. Davies, *Dielectric Properties and Molecular Behavior*, Van Nostrand Reinhold, London (1969)

[67] H. A. Kramers, Atti del Congr. Intern. Dei. Fisici, Como, **2**, (1927) 545

[68] A. Dalgrano and A. E. Kingston, Proc. Roy. Soc. A, **259**, (1960) 424

[69] R. L. Asher, D. Bellert, T. Buthelezi, V. Lewis and P. J. Brucat, Chem. Phys. Lett., **234** (1995) 113

[70] R. Chang, *Physical Chemistry with Applications to Biological Systems*, 2nd ed., Collier MacMillan Publishers, New York (1981)

[71] T. Hirota, K. Ogura, S. Shinzawa-Itoh, M. Yoshikiwa, M. Nagai and T. Kitagawa, J. Phys. Chem., **98** (1994) 6652

[72] P. C. Engelking and W. C. Lineberger, J. Am. Chem. Soc., **101** (1979) 5569

[73] L. S. Sunderlin, D. Wang and R. Squires, J. Am. Chem. Soc., **114** (1992) 2788

[74] Y. Kasai and K. Obi, J. Chem. Phys., **103** (1995) 90

[75] R. H. Shultz, K. C. Crellin and P. B. Armentrout, J. Am. Chem. Soc., **113** (1991) 8590

[76] P. W. Villalta and D. G. Leopold, J. Chem. Phys., **98** (1993) 7730

[77] G. Jeung, Chem. Phys. Lett., **232** (1995) 319

[78] D. G. Leopold and W. C. Lineberger, J. Chem. Phys., **85** (1986) 51

[79] A. Ricca, C. W. Bauschlicher Jr. and M. Rosi, J. Phys. Chem., **98** (1994) 9498

[80] M. Castro, D. R. Salahub and R. Fournier, J. Chem. Phys., **100** (1994) 8233

[81] G. Berthier, R. Cimiraglia, A. Daoudi, H. Mestdagh, C. Rolando and M. Suard, J. Mol. Struct. (Theochem) **254** (1992) 43

[82] A. Ricca and C. W. Bauschlicher Jr.,Theor Chim Acta, **92** (1995) 123

[83] V. Barone, Chem. Phys. Lett., **233** (1995) 129

[84] L. A. Barnes, M. Rosi and C. W. Bauschlicher Jr., J. Chem. Phys., **93**, (1990) 609

[85] A. Mavridis, J. F. Harrison and J. Allison, J. Am. Chem. Soc., **111** (1989) 2482

[86] P. Braustein, D. Matt and D. Nobel, Chem. Rev., **88** (1988) 747

[87] G. Herzberg, *Electronic spectra of Polyatomic Molecules*, Van Nostrand Reinhold, New York (1950)

[88] G. Herzberg, *Molecular Constants of Diatomic Molecules*, Van Nostrand Company, Inc., New York (1950)

[89] C. W. Bauschlicher Jr., H. Partridge and S. R. Langhoff in *Advances in Metal and Semiconductor Clusters*, **Volume II**, M. A. Duncan (editor) JAI Press, New York, (1994) 165-175

[90] J. Schwarz and H. Schwarz, Organometallics, **13** (1994) 1518

[91] B. S. Freiser (editor), *Organometallic Ion Chemistry*, Kluwer Academic Publishers (1996)

[92] C. T. Scurlock, S. H. Pullins and M. A. Duncan, J. Chem. Phys., **105** (1996) 3579

[93] C. S. Yeh, K. F. Willey, D.L. Robbins, J. S. Pilgrim and M.A. Duncan, J. Chem. Phys., **98** (1993) 1867

[94] R. L. Asher, D. Bellert, T. Buthelezi, G. Weeraseka and P. J. Brucat, Chem Phys. Lett., **228** (1994) 390

[95] D. E. Lessen, R. L. Asher and P. J. Brucat, J. Chem. Phys., **95** (1991) 1414

[96] D. Stogryn and A. P. Stogryn, Molecular Physics, **11** (1966) 319

[97] M. Sodupe, V. Branchadel , M. Rosi and C. W. Bauschlicher , Jr. , not yet published paper (1997)

[98] M. D. Morse, Chem. Rev. **86** (1986) 1049

[99] M. D. Morse, Adv. Metal Semicond. Clusters. **1** (1993) 83

[100] A. D. Sappey, J. E. Harrington and J. C. Weisshaar, J. Chem. Phys., **91** (1989) 3854

[101] J. C. Pinegar, J. D. Langenberg, C. A. Arrington, E. M. Spain and M. D. Morse, J. Chem. Phys., **102** (1995) 666

[102] R. L. Asher, D. Bellert, T. Buthelezi and P. J. Brucat, Chem. Phys. Lett., **224** (1994) 529

[103] E. M. Spain and M. D. Morse, J. Chem. Phys., **97** (1992) 4641

[104] T. H. Upton and W. A. Goddard III, J. Am. Chem. Soc., **100** (1978) 5659

[105] C. W. Bauschlicher Jr., H. Patridge and S. R. Langhoff, Chem. Phys. Lett., **195** (1992) 360

[106] D. Lessen and P. J. Brucat, Chem. Phys. Lett., **160** (1989) 609

[107] D. Bellert, T. Buthelezi, V. Lewis, K. Dezfulian, D. Reed, T. Hayes and P. J. Brucat, Chem. Phys. Lett., **256** (1996) 555

[108] H. Wang, H. Haouari, R. Craig, J. R. Lombardi, and D. M. Lindsay, J. Chem. Phys., **104** (1996) 3420

[109] L. Lian, C. X. Su, and P. B. Armentrout, Chem. Phys. Lett., **180** (1991) 168

[110] J. Ho, M.L. Polak, K. M. Ervin and W. C. Lineberger, J. Chem. Phys., **99** (1993) 8542

[111] M. Merchan, R. Pou-Amerigo and B. O. Roos, Chem. Phys. Letters, **252** (1996) 405

[112] C. A. Arrington, T. Blume and M. D. Morse, J. Phys. Chem, **98** (1994) 1398

[113] A. M. James, P. Kowalczyk, E. Langlois, M. Campbell, A. Ogawa and B. Simard, J. Chem. Phys., **101** (1994) 4485

[114] M. Cheeseman, R. J. Van Zee and W. Weltner, Jr., J. Chem. Phys., **92** (1990) 1553

[115] R. L. Hettich and B.S. Freiser, J. Am. Chem. Soc., **109** (1987) 3537

[116] S. P. Walch and C. W. Bauschlicher, Jr. in *Comparison of Ab Initio Quantum Chemistry with Experiment for Small Molecules*,R. J. Bartlett (editor) Reidel, Dordrecht (1985) 312-355

[117] T. L. Haslett, M. Moskovits and A. L. Weitzman, J. Mol. Spec., **135** (1989) 259

[118] B. Simard, A. M. James, P. Kowalczyck, R. Fournier and P. A. Hackett, SPIE, **2124** (1994) 376

[119] L. A. Russon, S. A. Heidecke, M. K. Birke, J. Conceica, M. D. Morse and P.B. Armentrout,, J. Phys. Chem, **100** (1994) 4747

[120] D. E. Lessen, R. L. Asher and P. J. Brucat, Chem. Phys. Lett., **182** (1991) 412

[121] M. F. Jarrold, A. J. Illies and M. T. Bowers, J. Am. Chem. Soc., **107** (1985) 7339

[122] P. J. Brucat, L. S. Zheng, C. L Pettiette, S. Yang and R. E. Smalley, J. Chem. Phys., **84** (1986) 3078

[123] P. B. Armentrout in *Metal-Ligand Interactions*, N. Russo and D. R. Salahub (editors) Kluwer Academic Publishers, Netherlands (1996) 200-223

[124] K. Ervin, S. Loh and P. B. Armentrout, J. Phys. Chem., **87** (1983) 3593

[125] S. Loh, L. Lian, D. A. Hales and P. B. Armentrout, J. Phys. Chem., **92** (1988) 4009

[126] M. M. Goodgame and W. A. Goddard III, Phys. Rev. Lett., **54** (1985) 661

[127] C. W. Bauschlicher, Chem. Phys. Lett., **156** (1989) 95

[128] R. G. Root in *Laser-Induced Plasmas and Applications*, L. J. Radziemski and D. A. Cremers (editors) Marcel Dekker, Inc., New York (1989) 69-104

[129] H. J. Fischbeck and K. H. Fischbeck, *Formulas Facts and Constants*, 2nd ed., Springer-Verlag, New York (1987)

BIOGRAPHICAL SKETCH

The author was born December 25, 1967, to Joseph Faniza and Theresa Liapeng Buthelezi in Soweto, South Africa. She first attended school at St. Martin's Primary school, high school at both St. Barnabas (Bosmont, South Africa) and Miss Porter's School (Farmington, CT, USA). In the fall of 1987 she enrolled at Williams College and received a Bachelor of Arts Degree (with honors in Chemistry) in 1991. She then taught at Jabulani high school (Soweto, SA), January to June 1992. The author registered at the University of Florida from the Fall of 1992 to the present where she studied physical chemistry and worked with the Brucat research group on high-resolution photodissociation spectroscopy of transition metal containing molecular ions.

I certify that I have read this study and that in my opinion it conforms to acceptable standards of scholarly presentation and is fully adequate, in scope and quality, as a dissertation for the degree of Doctor of Philosophy.

Philip Brucat, Chair
Associate Professor of Chemistry

I certify that I have read this study and that in my opinion it conforms to acceptable standards of scholarly presentation and is fully adequate, in scope and quality, as a dissertation for the degree of Doctor of Philosophy.

William Weltner Jr.
William Weltner, Jr.
Professor of Chemistry

I certify that I have read this study and that in my opinion it conforms to acceptable standards of scholarly presentation and is fully adequate, in scope and quality, as a dissertation for the degree of Doctor of Philosophy.

Martin Vala
Martin Vala
Professor of Chemistry

I certify that I have read this study and that in my opinion it conforms to acceptable standards of scholarly presentation and is fully adequate, in scope and quality, as a dissertation for the degree of Doctor of Philosophy.

Michael Zerner
Michel Zerner
Professor of Chemistry

I certify that I have read this study and that in my opinion it conforms to acceptable standards of scholarly presentation and is fully adequate, in scope and quality, as a dissertation for the degree of Doctor of Philosophy.

Timothy J. Anderson
Timothy Anderson
Professor of Chemical Engineering

This dissertation was submitted to the Graduate Faculty of the Department of Chemistry in the College of Liberal Arts and Sciences and to the Graduate School and was accepted as partial fulfillment of the requirements for the degree of Doctor of Philosophy.

August, 1997

Dean, Graduate School